UNIVERSITÀ DEGLI STUDI DI CATANIA
DIPARTIMENTO DI SCIENZE BIOLOGICHE, GEOLOGICHE E AMBIENTALI

Dottorato di Ricerca in
Scienze Geologiche, Biologiche e Ambientali
- XXIX CICLO -

Marisa Giuffrida

MAGMA STORAGE, ASCENT AND DEGASSING HISTORIES TRACED BY TEXTURES AND CHEMICAL ZONING IN CRYSTALS: APPLICATION TO THE CO_2-RICH BASALTIC SYSTEM OF MT. ETNA VOLCANO

Tutor
Prof. Marco VICCARO

Coordinatore del Dottorato di Ricerca
Prof. Agata DI STEFANO

Catania 2017

MAGMA STORAGE, ASCENT AND DEGASSING HISTORIES TRACED BY TEXTURES AND CHEMICAL ZONING IN CRYSTALS: APPLICATION TO THE CO_2-RICH BASALTIC SYSTEM OF MT. ETNA VOLCANO

Marisa Giuffrida

INDEX

1. INTRODUCTION **5**

2. MT. ETNA: A CASE STUDY FOR UNDERSTANDING MAGMA DYNAMICS IN CO_2-RICH BASALTIC SYSTEMS **10**

2.1. Brief history of Mt. Etna 10
2.2. The eruptive activity between January 2011 and April 2013 14

3. CONSTRAINING THE NATURE AND TIMESCALES OF MAGMATIC PROCESSES **19**

3.1. Strategy of investigation 19
3.2. Sampling and selection of the volcanic products 20
3.3. Analytical procedures 22
3.3.1 Whole rock analyses 22
3.3.2 In-situ microanalytical data 22
3.4. Geochemical and petrological characterization of volcanic rocks 26
3.4.1 Bulk rock geochemistry 26
3.4.2 Petrography and chemistry of minerals 32
3.5. Textural and compositional features of plagioclase and olivine crystals 37
3.5.1 Plagioclase textures 37

3.5.2 Minor and trace element zoning in plagioclase and their relation with major element variations 42
3.5.3 Lithium compositional gradients in plagioclase 53
3.5.4 Olivine chemical zoning patterns 55
3.6. Discussion 62
3.6.1 Evidence of magma evolution throughout the 2011-13 activity of Mt. Etna 62
3.6.2 The importance of investigating mineral textures and zoning 65
3.6.3 Processes controlling major, minor and trace element zoning in plagioclase 67
3.6.4 Crystallization conditions and magma dynamics inferred from chemical zoning and textures of plagioclase 70
3.6.5 Magma storage zones and recharging processes inferred from olivine compositional zoning 77
3.6.6 Time constraints of magma residence and transfer by modeling the chemical zoning of plagioclase and olivine crystals 92
3.6.6.1 Plagioclase residence time in the plumbing system of Mt. Etna 93
3.6.6.2 Fe-Mg diffusion modeling in olivine crystals and timescale of magma storage and recharge beneath Mt. Etna 101
3.6.7 The origin of lithium chemical gradients in plagioclase crystals 110
3.6.7.1 Lithium *diffusion and timescales of magma degassing* 115
3.6.8 General picture of Mt. Etna dynamics beneath the New South East Crater 118
4. UNDERSTANDING THE INFLUENCE OF CARBON DIOXIDE ON MINERAL STABILITY DURING MAGMA STORAGE AT INTERMEDIATE AND SHALLOW CRUSTAL LEVELS 121
4.1. Introduction 121
4.2. Experimental methods 122
4.2.1 Anhydrous glass synthesis 122
4.2.2 Sample hydration and preparation of capsules for experiments 124

4.2.3 Crystallization and flushing experiments in Internally Heathed Pressure Vessels [IHPV] 125

4.3. Analytical methods 129

4.3.1. KFT measurements of H_2O content in initial hydrous glasses 129

4.3.2. Determination of sample fluid compositions after experiments 130

4.3.3. Electron Microprobe Analysis (EMPA) 132

4.4. Experimental Results 132

4.4.1 Mineral assemblage and composition of the post-run hydrated products 132

4.4.2 Mineral assemblage and composition of the products after CO_2 flushing 133

4.4.3 Composition of the experimental glasses 138

4.5. Discussion 140

4.6. Implications on natural samples 144

5. CONCLUDING REMARKS 149

REFERENCES 150

MAGMA STORAGE, ASCENT AND DEGASSING HISTORIES TRACED BY TEXTURES AND CHEMICAL ZONING IN CRYSTALS: APPLICATION TO THE CO_2-RICH BASALTIC SYSTEM OF MT. ETNA VOLCANO

1. INTRODUCTION

Continuous advancement in the quality of geophysical methods and accessibility of *in-situ* analytical techniques during the last twenty years has led to an exponential increase in the knowledge of the geometry of volcanic feeding systems and of the processes of magma emplacement, transfer and degassing that catalyze an eruption. Among the multiple techniques of investigation of plumbing system dynamics, analysis of textures and chemical zoning in minerals has been established as one of the most efficient tools (e.g. Davidson et al., 2001; 2007; Ginibre et al., 2007; Humphreys et al., 2006; Morgan and Blake, 2006; Streck, 2008; Viccaro et al., 2010; 2012; 2016a; Kahl et al., 2011; 2013; 2015). Minerals can be highly sensitive to gradual or sudden changes in the volcanic system, and for this reason, decades ago, they started to be employed as archives of magmatic processes (i.e. Larsen et al., 1938). With development of high-precision *in-situ* analytical techniques, such as electron microprobe (Castaing, 1951), ion microprobe (Slodzian, 1964), laser ablation mass spectrometry (Ginibre et al., 2007), and microdrilling (Davidson et al., 2007), it became evident that crystals preserve a huge source of information in their textural and compositional zoning, providing evidence for changes in chemical (i.e. melt and fluid composition) and/or physical (i.e. temperature,

pressure and oxygen fugacity) conditions of the magmatic system during their growth history (Singer et al., 1995; Wallace and Bergantz, 2002, 2004; Ginibre et al., 2007; Streck, 2008; Viccaro et al., 2010; Kahl et al., 2011, 2013).

Additionally, diffusion chronometry applied to compositionally zoned crystals has proved to be valuable for determining the timescales that lead to such changes (e.g., Zellmer et al., 1999; 2003; Costa et al., 2003, 2008; Costa and Chakraborty, 2004; Costa and Morgan, 2010; Morgan et al., 2004; Morgan and Blake, 2006; Kahl et al., 2011, 2013, 2015; Druitt et al., 2012; Viccaro et al., 2016a, 2016b). Measurements of compositional gradients in minerals and glasses have been used to quantify the timing of residence and ascent of magma bodies, as well as of magma chamber processes (e.g. addition of new melts and mixing), over periods $>10^5$ years (e.g., Zellmer et al., 1999, 2003; Costa and Chakraborty, 2004; Morgan et al., 2004; Morgan and Blake, 2006). More recent innovations in geochemical analyses, such as secondary ion mass spectrometry (SIMS), permit measurement of a variety of trace elements (e.g. Li and B) that are inaccessible by other analytical techniques, but are crucial for the study of late-stage degassing processes that occur just prior to or during the eruption (e.g. Genareau et al., 2007; Genareau and Clarke, 2010; Charlier et al., 2012; Cabato et al., 2013).

However, studies of volcanic processes rarely attempt to decipher the time-space relationships among multiple pre-eruptive processes by integrating different types of data (i.e., in-situ major and trace elements, chemical diffusion, textural heterogeneities) on more than one single mineral phase. Indeed, many different events are generally involved at the same time in the petrogenesis of volcanic rocks. This makes complex the quantification of the rates at which many important processes operate, from the early

stages of magma ascent to eruption, and therefore limits a full understanding of how a volcano works.

To properly interpret the textural and compositional records preserved in magmatic crystals, awareness of the role of volatile species is also needed because of the profound influence volatiles have on melt properties and phase equilibria (Sparks and Pinkerton, 1978; Sparks, 2003), and consequently on magma ascent dynamics and styles of eruption (Papale and Dobran, 1994; Papale et al., 1998; Blundy and Cashman, 2001; Sparks et al., 2003; Cashman, 2004). Typically, the composition of magmatic volatiles is dominated by H_2O and CO_2. These two components behave quite differently in the melt during ascent, as a result of their strong pressure-dependent and contrasting solubilities (e.g., Holloway and Burnham, 1972; Holloway, 1976; Burnham, 1979; Webster et al., 1999; Lowenstern, 2001; Newman and Lowenstern, 2002; Shishkina et al., 2014b; Witham et al., 2012). In the last decade, understanding the behavior of mixed volatile components, especially H_2O and CO_2, during magma ascent has become an important aspect of experimental studies aimed at unraveling the effects of ascent rates on kinetics of magma vesiculation, crystallization and eruption (e.g. Mourtada-Bonnefoi and Laporte, 2002; Cichy et al., 2011; Pichavant et al., 2013; Riker et al., 2015; Fiege et al., 2015). In spite of the increasing interest in reproducing crystallization paths of multicomponent volatile-bearing systems, previous studies did not address changes in crystal stability in response to variations in the CO_2 proportion of the magmatic system. The interpretation of textural and compositional features of crystals has been so far conducted through experimental reproduction of processes of crystal dissolution/resorption or growth in presence of a pure-H_2O magmatic fluid phase (e.g. Logfren, 1974, 1980; Kirkpatrick, 1981;

Tsuchiyama and Takahashi, 1983; Tsuchiyama, 1985; Housh and Lurh (1991); Kawamoto, 1992; Hummer and Rutherford, 2002), whilst the influence of CO_2 on mineral textural and compositional changes has been generally neglected and, at present, it is still not understood.

Such general lack of information precludes a proper interpretation of natural samples. In particular, it makes problematic the study of CO_2-rich magmatic systems, where the deep exsolution of CO_2 and its flushing at shallow levels may play a dominant role in triggering eruptions. In this regard, several authors have provided evidence that sudden onset of explosive activity at CO_2-rich basaltic volcanoes is directly associated with fast ascent of CO_2 from the deep plumbing system (Aiuppa et al., 2007, 2010b; Cannata et al., 2008; Ferlito et al., 2014; Shinohara et al., 2008; Allard, 2010; Pichavant et al., 2013). Among basaltic systems largely enriched in CO_2, Mt. Etna volcano has been particularly distinguished in the last decade for its recurrent, high-energy eruptions. The paroxysmal activity between 2011 and 2013 at the volcano summit represents one of the most impressive chapters in the history of Mt Etna, which produced in this period more than 40 paroxysmal episodes with sustained lava fountains and eruptive columns of several kilometres.

This study offers an innovative petrological approach that combines the textural, chemical and temporal records of magmatic crystals with experimental simulations to produce a realistic spatial-temporal reconstruction of magmatic dynamics that precede and accompany the beginning of paroxysmal eruptions at Mt. Etna between 2011 and 2013. Selection of Mt. Etna as case-study provides the opportunity to evaluate modes and timescales of magma transfer across a very dynamic and complex plumbing system. The

investigation of this recent paroxysmal activity also allows focus on factors controlling explosivity at basaltic volcanoes through investigation of less commonly explored evolutionary dynamics of magmas (e.g. processes of CO_2 flushing) during storage in deep and shallow reservoirs.

Topics of this study have been handled following two main tasks of investigation. The first task aims to constrain the nature of the plumbing system dynamics (e.g. storage conditions, intrusion and mixing, degassing) and their space-time relationships during the 2011-2013 eruptive sequence. This required a detailed investigation of the textural and compositional characteristics of crystals in terms of major, minor and trace element zoning, along with a thermodynamic analysis of the system and the definition of time constraints through diffusive chemical equilibration of crystal zoning. The second task of investigation includes crystallization experiments on H_2O+CO_2-bearing K-trachybasalts of the post-2011 activity of Mt. Etna, with the aim to test the influence of CO_2-flushing on mineral stability and melt chemistry during storage in the intermediate and shallow plumbing system.

Topics and tools introduced in this study allow development of a comprehensive model of the plumbing system dynamics at Mt. Etna and offer the basis for a better comprehension of the chemical and physical processes driving the eruption onset at basaltic volcanoes enriched in CO_2. Relevance of this study mainly relies on the quantification of volcanic processes at depth that may have considerable consequences in development of unusual, high-energy eruptions at basaltic volcanoes that are, otherwise, acknowledged to be characterized by weak to mild explosive activity.

2. *MT. ETNA:* A CASE STUDY FOR UNDERSTANDING MAGMA DYNAMICS IN CO_2-RICH BASALTIC SYSTEMS

2.1. ***Brief history of Mt. Etna***

Mt. Etna is a persistently active open-conduit volcano that rises up 3329 m a.s.l. on the eastern coast of Sicily (Southern Italy). The volcano lies at the intersection of three structural domains: the Apennine - Maghrebian overthrust belt system, the Hyblean Plateau and the oceanic Ionian domain (e.g., Cristofolini et al., 1985; Ciliberto et al., 2009; Fig.1). In this area, processes of extensional tectonics are active, as evidenced by the presence of several eruptive fissures and deep normal faults, cutting a ~22 Km thick continental crust, that accommodate extensional processes at a regional scale (Monaco et al., 1997).

Over centuries, Mt. Etna has produced both effusive and explosive eruptions with predominant emissions of tholeiites and OIB-type alkali basalts. The volcanic activity began ~600 ka ago with effusion of submarine tholeiitic pillow lavas, followed ~300 ka ago by the eruption of subaerial tholeiites, which still outcrop on the southern flanks of the volcano (Branca et al., 2008). Composition of erupted magmas changed to transitional, and then become Na-alkaline ~220 ka (e.g., Cristofolini and Romano, 1982; Tanguy et al., 1997; Viccaro and Cristofolini, 2008; Viccaro et al., 2011). The first evidence of explosive eruptions dates back to 122-130 ka to the building of central-conduit edifices that occurred with cycles of Strombolian and Plinian eruptions (cf. Branca et al., 2008). At present, traces of the volcanic centers related to this phase of activity are visible in the Valle del Bove depression. Activity in the last 15 ka has

displayed very variegate eruptive styles, including central and fissure flank effusions, moderately explosive summit eruption ranging in style from Strombolian to lava fountaining and, more rarely, exceptionally violent explosive episodes (sub-Plinian to Plinian eruption) that produced several pyroclastic deposits (Coltelli et al., 1998).

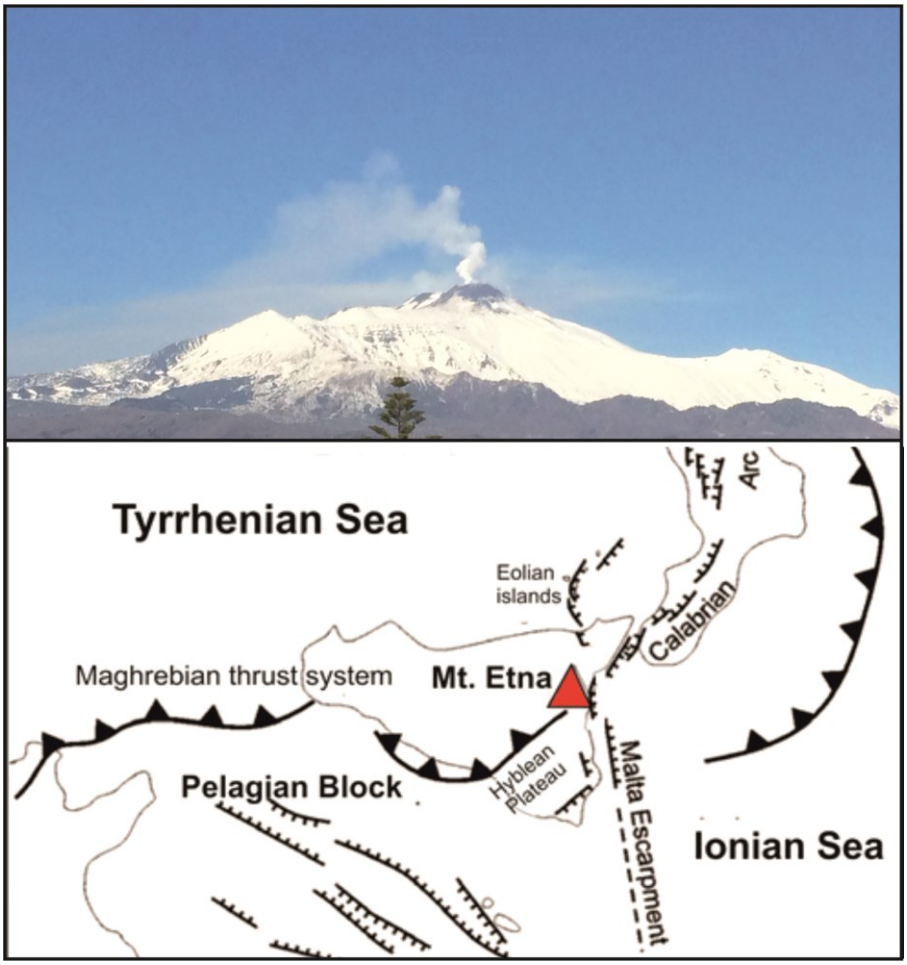

Figure 1. *View of the southeastern flank of Mt. Etna volcano (top) and its geodynamic framework (bottom) with the main structural domains of southern Italy involved in active tectonics.*

Compositions of these products span from picritic and alkali basalt to trachytes, with hawaiites being the dominant rocks (D'Orazio et al., 1994). Historic eruptions in the last few centuries were dominantly effusive, producing primarily subaphyric to mildly porphyritic hawaiites; however, the magma chemistry and eruptive behavior have changed significantly over the last four decades. Indeed, Etna has been increasingly more active since 1971, showing higher eruption frequency and output rate (Hughes et al., 1990; Branca and Del Carlo, 2005; Bonaccorso and Calvari, 2013). Erupted lavas have also evolved compositionally, becoming more basic and richer in alkali elements and Sr and B isotopes. In contrast, Th and Nd-Pb-Hf isotope ratios are more depleted than the former lavas (e.g., Tanguy et al. 1997; Clocchiatti et al. 2004; Metrich et al., 2004; Viccaro and Cristofolini, 2008; Viccaro et al. 2011; Correale et al., 2014). Changes of the product chemistry toward K-trachybasaltic compositions were observed particularly after the 2001 A.D. and have been attributed to progressive replenishment of the plumbing system by more alkaline, volatile-rich magma with a new geochemical signature (cf. Clocchiatti et al. 2004; Métrich et al. 2004; Rizzo et al. 2006; Viccaro et al. 2006; Corsaro et al. 2009; Ferlito et al., 2012; Nicotra and Viccaro 2012a).

The volcanic activity during the last 20 years has displayed more explosive behavior, with spectacular explosive flank eruptions, such as in 2001 and 2002-2003 (Andronico et al., 2005) and an increasing number of paroxysms at the summit craters (Allard et al., 2006; Bonaccorso and Calvari, 2013; Viccaro et al., 2014, 2015). Main paroxysmal episodes occurred at the South East Crater (SEC) between September 1998 and February 1999 (23 events) and between January and June 2000 (64 events; La Delfa et al. 2001; Andronico and Corsaro 2011). Later, another short sequence of paroxysms

took place during the period March - September 2007, with a limited series of 7 eruptions at the SEC (Andronico et al. 2008). Since 2011, the main site of activity has moved to a newly formed summit crater, i.e. the New South East Crater (NSEC; Behncke et al.; 2014) that was the locus of a long sequence of paroxysmal episodes between 2011 and 2013 (Fig. 2). The episodes that took place at the NSEC have shown similarity with the series of paroxysms that occurred at the South East Crater (SEC) during 1998-1999, 2000 and 2007 A.D. for what concern the general evolution of the eruptive phenomena that always started with increasing Strombolian explosions evolving to sustained lava fountains. The fountaining phase typically extinguished in few hours, but often occurred together with lava flow emissions.

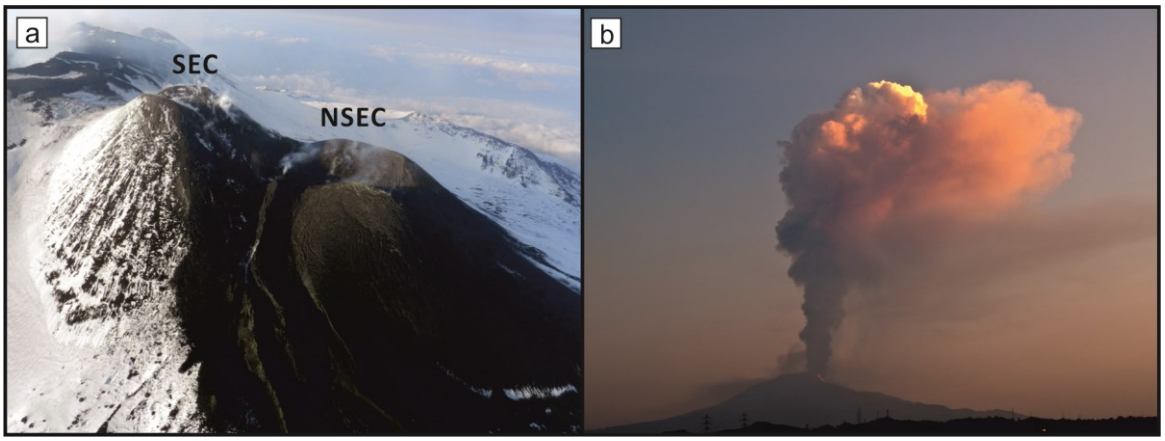

Figure 2 . a) *Aerial view of the Etna' New South East Crater (NSEC) and the nearby South East Crater (SEC) at the date of March 4, 2013. The South East cone, on the left side, last erupted on May 2007, whereas the New South East Crater cone, on the right, has entirely grown between 2011 and 2013; photo provided by INGV-Osservatorio Etneo (www.ct.ingv.it); b) Eruptive column produced during the culminating phase of the August 12, 2011 paroxysmal episode, seen from Catania. Photo by Marco Viccaro, University of Catania..*

After a brief period of dominantly effusive behavior that followed the 2011-2013 paroxysmal sequence, Mt Etna has had new exceptionally violent paroxysmal episodes during the months of December 2015 and May 2016. Eruptions took place at the summit crater Voragine that was the site of some of the most explosive episodes recorded during the last two decades, producing several kilometers-high eruptive columns and lava fountains more than 1 km in height. Episodes of severe ash and tephra fall-out affected the volcano flanks and, in the case of the most energetic eruptions (i.e. the paroxysm of December 3, 2015), the dispersion of a huge amount of ash also forced the shutdown of the nearby airport of Catania for hours.

2.2. The eruptive activity between January 2011 and April 2013

The spectacular sequence of lava fountaining that occurred in the period 2011-2013 led to the formation of a large cone, called the New South East Crater (NSEC; Fig.2; Behncke et al.; 2014), in a relatively short time span. With a 44 paroxysmal events between January 2011 and December 2013 (38 at the date of April 27, 2013, which are the focus of the present work; Table 1), this young summit crater could be likely considered the most important expression of high explosivity at Mt. Etna of the last decade.

The NSEC began to grow on November 6, 2009, after a ~5 m-wide pit crater opened at the southeastern base of the SEC. During the months of April and May 2010, the bottom of the pit-crater underwent progressive widening and deepening, rapidly evolving into a new summit crater. After eight months of rest, the NSEC erupted again on January 2–3, 2011 with low-intensity Strombolian explosions that were accompanied by pulsating

emission of gasses. An increase in activity was observed on January 11, with cycles of explosions becoming progressively more powerful and close in time until the evening of January 12. At 22.00 (Local Time UTC+1), Strombolian explosions abruptly increased in intensity and frequency, finally culminating in sustained lava fountains. The paroxysmal phase lasted about 2 hours and was accompanied by lava flow emission from the crater and conspicuous ash-lapilli fallout on the eastern flank of the volcano. At around 23.30 (Local Time UTC+1), the activity rapidly declined and ended after a series of weak Strombolian explosions.

All the 38 episodes between January 2011 and April 2013 that follow this first paroxysmal eruption had similar main characteristics, although they differed in intensity and duration (see Table 1): in all the cases, paroxysmal activity started with increasing Strombolian explosions, evolving in short times to lava fountaining and sustained eruptive columns, having average height of 5-6 km. Most of the events lasted less than 24 hours, considering the time span from the beginning of intensification of the Strombolian activity to the end of eruption (Behncke et al. 2014; Viccaro et al., 2014, 2015). Average duration of the paroxysmal phases during the entire 2011–2013 period vary between 20 minutes and a couple of hours, with some exceptions of paroxysmal phases lasting more than 5 h (e.g., the episodes of February 18, April 10 and July 24, 2011, and the February 9, 2012 eruptions; Behncke et al., 2014; Table 1). Some of the main differences among the paroxysmal eruptions also concern the duration of the Strombolian activity preceding the lava fountaining (cf. Viccaro et al., 2015). In this regard, some events showed slow intensification of the Strombolian activity, which often lasting for a long time (up to some days); other episodes exhibited very fast evolution of the eruptive phenomena, reaching

N° of the event	Date of the event	Start of the paroxysmal phase (GMT)	End of the paroxysmal phase (GMT)
1	January 12, 2011	21:50	22:55
2	February 18, 2011	3:30	14:30
3	April 10, 2011	8:00	14:00
4	May 12, 2011	2:00	6:10
5	July 9, 2011	13:45	15:30
6	July 19, 2011	0:00	2:30
7	July 24, 2011	2:30	6:30
8	July 30, 2011	19:30	21:30
9	August 5, 2011	21:30	0:15
10	August 12, 2011	8:30	10:25
11	August 20, 2011	6:55	7:50
12	August 29, 2011	4:05	4:50
13	September 8, 2011	6:30	8:45
14	September 19, 2011	12:20	13:00
15	September 28, 2011	19:31	20:10
16	October 8, 2011	14:30	17:45
17	October 23, 2011	18:30	21:15
18	November 15, 2011	11:19	12:42
19	January 5, 2012	5:25	7:00
20	February 9, 2012	0:30	5:30
21	March 4, 2012	7:30	9:32
22	March 18, 2012	7:15	9:59
23	April 1, 2012	2:00	3:30
24	April 12, 2012	14:10	15:20
25	April 24, 2012	1:30	2:15
26	February 19, 2013	3:42	5:02
27	February 20, 2013	0:45	2:34
28	February 20, 2013	13:20	14:30
29	February 21, 2013	n.d.	n.d.
30	February 23, 2013	18:20	19:20
31	February 28, 2013	10:10	11:00
32	March 5, 2013	23:20	0:10
33	March 16, 2013	17:50	18:10
34	April 3, 2013	14:00	15:35
35	April 12, 2013	04:00	12:00
36	April 18, 2013	11:00	13:15
37	April 20, 2013	15:13	16:40
38	April 27, 2013	16:30	20:00

Table 1 - *List of the 38 paroxysmal eruptions occurred during the 2011-2013 period (at the date of April 27). Timing for the start and end of the paroxysmal phase of each event has been derived from the multidisciplinary reports of the INGV - Osservatorio Etneo available at www.ct.ingv.it.*

the paroxysmal phase after just few hours of Strombolian activity. Lava fountaining phases were also generally coupled with emplacement of rheomorphic lava flows descending the Valle del Bove flanks for several kilometers (Calvari et al., 2011; Bonaccorso and Calvari, 2013). On 27 April 2013, the continuous superimposition of lava flows generated during paroxysmal eruptions produced a huge lava flow field on the northwestern side of the Valle del Bove depression (Fig.3), yielding important morphological modifications of the landscape on and around the summit area of Mt. Etna.

It is also interesting to note that the frequency of the paroxysmal eruptions was not constant over the 2011-2013 eruptive period; 25 episodes took place from January 2011 to April 2012 and, after ~10 months of rest, a further 13 events were recorded between February and April 2013 (cf. Viccaro et al., 2015). Moreover, the time gap between eruptions strongly changes over time; during the first half of 2011 and from November 2011 to the first episode of 2012 (on January 5), paroxysms occur with low frequency of 4-8 weeks. In this period, only two eruptions in July 2011 occur within a limited time span of 6 days (e.g. the events of July 24 and 30, 2011). In this circumstance, also the intensity of volcanic activity was strongly amplified. The short paroxysmal sequence of 2012 has average recurrence time of about two weeks. Eruptive phenomena from February 2013 displayed an unusually high frequency of occurrence; the first five episode of 2013 were separated by only 36 hours, whereas the subsequent eight episodes (until April 27, 2013) had inter-eruptive period between 2 and 10 days.

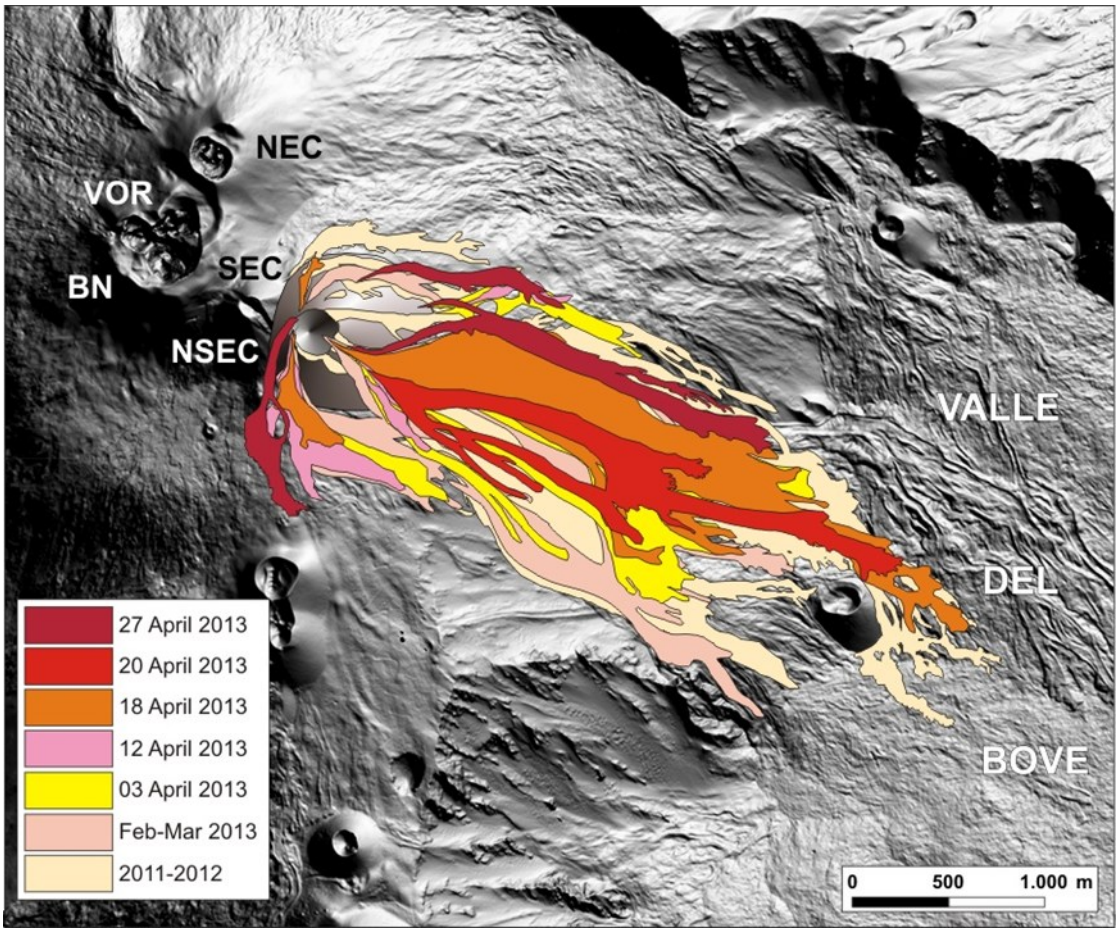

Figure 3. *Lava field formed by single flow units emitted between January 2011 and April 2013, as resulted from the GPS survey performed by Behncke et al. (2014). The map also reproduce the location of the summit craters. NSEC: New South East Crater; SEC: South East Crater; BN: Bocca Nuova; VOR: Voragine; NEC: North East Crater.*

3. CONSTRAINING MODES AND TIMESCALES OF MAGMATIC PROCESSES

3.1 Strategy of investigation

One of the primary targets of the present work is a detailed definition and quantification of the physical and geochemical magmatic processes driving the eruption onset for the recent 2011-2013 paroxysmal episodes at Mt. Etna. To accomplish these goals, the present study first focused on relevant petrographic and mineral chemical characteristics of a total of 88 lava samples, which represent the paroxysmal sequence that occurred between January 2011 and April 2013 (eruptive episodes listed in Table 1). On selected samples, attention has been mainly focused on textural and *in-situ* compositional analysis of minerals sensitive to chemical and physical variations of the magmatic system, mainly plagioclase and olivine. Crystals from representative paroxysms within the period under investigation have been analysed using multiple *in-situ* analytical approaches (i.e. SEM-EDS/WD, LA-ICP-MS, SIMS) with the aim to characterize major, minor and trace element concentrations. Timescales of magma residence and open-system magmatic processes have been constrained through the application of different diffusion modelling approach on the chemical zoning of plagioclase and olivine crystals. A selection of plagioclase crystals has been also analysed in order to quantify dynamics and processes occurring at exceptionally fast timescales, such as gas-rich magma ascent and degassing, through the determination of the ^{7}Li concentration gradients. Lithium measurements along crystal rims have been finally coupled with diffusion models to determine rates of magma ascent during volatile exsolution upon eruption, and to show

how the latest-stage syn-eruptive processes associated with paroxysmal activity can be quantified over unusually short timescales.

3.2 Sampling and selection of the volcanic products

Ten relevant eruptive episodes at Mt. Etna have been selected among the 38 paroxysms between January 2011 and April 2013 AD to test various methodological approaches on mineral phases, including some of the most avant-garde techniques in petrology and geochemistry. Lava rocks used in this study are part of the extensive dataset (88 rock samples) already published by Viccaro et al. (2015). These lavas were sampled during or just after the end of the volcanic activity in order to definitively constrain their date of emission. The main criteria for selection of the samples include petrological differences between lava rocks (i.e. porphyritic index, proportions of any single mineral phase within thin sections, groundmass texture), as well as the duration of the Strombolian activity preceding the fountaining phase, as derived from the reports of INGV-Osservatorio Etneo (www.ct.ingv.it). For volcanic products erupted during the 2011-2012 period of activity, the temporal evolution (high/low rate of increase) of the volcanic tremor amplitude (VTA) during the Strombolian phase preceding the lava fountaining activity has been also considered. Distinction of the paroxysmal episodes based on these seismic signals utilizes geophysical data reported in Viccaro et al. (2014), which showed that amplitude and source location of volcanic tremor drastically change during the evolution of each lava fountain and they are also related to the dynamics of pre-eruptive magmatic processes at depth. Based on these evidences, within the period under investigation, I selected a) five short-lasting eruptions characterized by a rapid

intensification of the seismic signal preceding the fountaining and/or preceded by a short (< 4h) Strombolian phase, and b) five long-lasting eruptions, showing low-rates of VTA increase prior to the paroxysm and/or a long Strombolian phase (5-18 h) preceding the fountaining (cf. Viccaro et al., 2014). Selected episodes and their evolutionary features are listed in Table 2.

Table 2. *Chronology and evolutionary features of the 2011-2013 paroxysmal eruptions that have been selected for a detailed in-situ microanalisys of mineral phases and quantification of volcanic processes. Classification of the events as LL=Long-lasting and SL=Short- is based on the time gap between the intensification of the strombolian phase and the fountaining phase (>5h for LL events and <5h for SL events) and on the rate of volcanic tremor amplitude increase for those episodes for which is available.*

Date of eruption	Intensification Strombolian activity (GMT)*	Duration of the Strombolian phase preceding the paroxysm*	Rate of VTA increase	Eruption type
January 12, 2011	21:06	24h 44’	0.8	LL
February 18, 2011	01:41	1h 49’	6.3	SL
April 10, 2011	03:15	28h 50’	1.2	LL
July 30, 2011	03:41	16h	2.1	LL
March 04, 2012	04:20	3h 10’	12.6	SL
April 24, 2012	17:33	8h	2.6	LL
February 23, 2013 **	18:00	0h 30’	n.a.	SL
March 05-06, 2013 **	21:32	1h 16’	n.a.	SL
April 12, 2013 **	06:47	28h 3’	n.a.	LL
April 18, 2013 **	11:00	2h	n.a.	SL

* *Information taken from reports of INGV- Osservatorio Etneo and by Behncke et al. (2014)*

** *Seismic data not available*

3.3 Analytical procedures

3.3.1 Whole rock analyses

Major element compositions for all the collected volcanic rocks (88 samples) of the 2011-2013 activity were analyzed at the Dipartimento di Biologia, Ecologia e Scienze della Terra of Università della Calabria (Italy) by means of a Philips PW2404 WD-XRF on powder pellets, correcting for the matrix effects. Loss on ignition was determined by gravimetric methods. Trace element abundances were measured at the SGS Laboratories of Toronto (Ontario, Canada) on 40 selected samples representative of the January 2011-April 2013 eruptive sequence. Powdered rock samples were fused by Na-peroxide in graphite crucibles and dissolved using dilute HNO_3. Trace element analyses were then obtained by means of a Perkin Elmer ELAN 6100 inductively coupled plasma mass spectrometer. Four calibration runs were performed on international certified reference materials at the beginning and end of each batch of 20 samples. Precision is better than 5% for all the trace elements analyzed. Whole rock major and trace element measurements for volcanic rocks analyzed in this study are available at the following link: http://www.volcanology-unict.it/online_material/giuffrida_phd_thesis.

3.3.2 In-situ microanalytical data

In-situ major element compositions were obtained on plagioclase, olivine, clinopyroxene and opaque oxides representative of the main textural and size variability within volcanic rocks. A selection of plagioclase (70 crystals; 4692 spot analyses) and olivine phenocrysts (49 crystals; 2515 spot analyses) were also analyzed for major elements along core-to-rim or rim-to rim transects crosscutting the centers of crystals.

Analytical steps in plagioclase vary from 5 to 30 μm depending on the crystal size, whereas spot analyses within olivine are at steps of 7-15 μm. Data were acquired at the Dipartimento di Scienze Biologiche, Geologiche e Ambientali of Catania (Italy) using a Tescan Vega-LMU scanning electron microscope equipped with an EDAX Neptune XM4-60 micro-analyzer using an energy dispersive system characterized by an ultra-thin Be window, and coupled with an EDAX WDS LEXS (wavelength dispersive low energy X-ray spectrometer) calibrated for light elements. Operating conditions for the analysis of major element abundances in mineral phases were 20 kV accelerating voltage and 0.2 nA beam current. Repeated analyses on internationally certified minerals and glass standards during the analytical runs ensure precision for the collected elements between 3 and 5%.

On ~35 plagioclase crystals, the same core-to-rim traverses analyzed for major elements were followed to obtain trace element data by Laser Ablation Inductively Coupled Plasma Mass Spectrometry (LA-ICP-MS). Analyses were conducted at the Istituto Nazionale di Geofisica e Vulcanologia – section of Palermo (INGV-PA, Italy), by using a GeoLasPro 193 nm Excimer Laser system, equipped with an Agilent 7500ce quadrupole ICP-MS. Analyses were performed at 10 Hz and fluency of 14-18 J/cm2. Ablation spots are on the order of 25 μm in diameter, and steps between spots vary from 30 to 50 μm. To determine trace element concentrations in the ablated material, data acquisition was accomplished in peak-jumping mode with one point per peak and 10 ms dwell. Total analysis time was 2 minutes per spot, including 1 minute of background acquisition. Plasma conditions were adjusted to oxide formation rates below 0.6% (monitored using the 248/232 mass ratio), so that no further oxide corrections were necessary. 43Ca and 29Si were used as internal standards for both the geochemical

reference materials (NIST SRM 612) and natural samples. NIST SRM 612 served as the external standard and was measured at the beginning and at the end of each group of unknowns (20-30 sample measurements). Data were collected in time-resolved graphics mode to monitor compositional heterogeneities that might be present in the sample at the scale of the laser sampling and to monitor the inter-element fractionation. Data were transmitted to a PC and processed by the GLITTER program (Van Achterbergh et al. 2001). Instrument performance and stability were monitored by repeated measurements of USGS basaltic reference glass BCR-2G during the analytical sessions. At spot size 24 μm, the precision of the analyses is better than 10% for all trace elements, except for Li, Cs, Rb, Zn and Pb for which is between 20-30%. According to Pearce et al. (2011), analyses were corrected for the fractionation index obtained on BCR-2 by dividing the measured value (averaged on repeated analyses) by the accepted one.

The rims of plagioclase crystals from various eruptive events have been also characterized for ^{7}Li concentrations by Secondary Ion Mass Spectrometry (SIMS). Analyses were performed on selected crystals already characterized for major and trace elements, but along opposite transects with respect to the LA-ICP-MS traverses within the crystal. SIMS analyses were carried out using the IMS 4f Cameca ion microprobe installed at CNR-IGG (Pavia). The plagioclase crystals were selected on rock thin sections that were polished, washed in ultrasonic tank, dried and Pt-coated. The samples were first investigated with an optical microscope under transmitted and reflected light, and suitable micrographs were produced on the selected areas prior to SIMS investigation. A primary beam of 5 nA $^{16}O^{-}$, yielding a spot diameter of 6-8 μm at the sample surface, was used to sputter secondary ions from a series of points along transects

within the crystals. Experimental set up was the following: -12.5 kV accelerating voltage, 25-µm secondary-ion imaged field, 400-µm contrast aperture and 1800-µm field aperture. The energy filtering technique (range: 75-125 eV) was used to reduce matrix effects and improve analytical precision (Ottolini et al., 1993; Ottolini et al., 2002 and reference therein). A 900 (M/ΔM) mass resolution was used. Experimental data were collected in four, one-day analytical sessions. For the purposes of this paper, the basic run table included ^{7}Li and ^{30}Si. Lithium compositional profiles were obtained by determining average counts per second for the ^{7}Li isotope and then calculating a ratio with respect to ^{30}Si. This is because the raw Li data provided by SIMS are given in secondary ion intensity as a function of time. To use the raw data, the ion intensity of the ^{7}Li isotope need to be first normalized to the intensity of ^{30}Si. $^{7}Li^{+}$ and $^{30}Si^{+}$ were monitored over 5 analytical cycles with 8 and 4 second acquisition time for each, for a total time of 40 and 20 seconds respectively, after a 450-second waiting time to get steady-state sputtering conditions. NIST-SRM-610, NIST-SRM-612 and NIST-SRM-614 international standards (Gao et al., 2002; Pearce et al., 1997) were used as calibration samples in order to convert the ion signal for Li into Li concentrations (ppm). The resulting analytical reproducibility of the $^{7}Li/^{30}Si$ count ratios are ±1% (1σ) for NIST-SRM-610 over a one-day session. After SIMS analysis, thin sections were re-polished smoothly, and the analysed crystals were imaged again using light microscopy to determine the precise analysis pit locations along the crystal margins. SIMS craters were then re-analysed at the Dipartimento di Scienze Biologiche, Geologiche e Ambientali of Catania by scanning electron microscope in order to determine the exact major element composition and anorthite content within the SIMS pit locations. Specifically, the SEM-EDS SiO_2 (wt.%) values at each spot were

adopted in the SIMS quantification of Li at those micro-areas. Moreover, in order to further reduce the residual matrix effects (see Ottolini et al. (1993) for details), and consider the different SiO_2 (wt.%) values among the plagioclase crystals and the NIST glasses (~ 50 wt.% SiO_2 vs. 72.2 wt.% SiO_2 in the NIST-series glasses), we applied a correction to the relative-to-Si ion yields for Li, i.e., I(Li)/I(Si) / Li(at)/Si(at) [where I(Li) and I(Si) represent the ionic signals for Li and Si, and Li(at) and Si(at), their respective atomic concentrations]. The accuracy of the final SIMS data for Li concentration is quoted ≤ 10% rel. The anorthite composition determined at each SIMS analysis spot was finally used to correct the measured $^{7}Li/^{30}Si$ ratios for the variation in silica. Specifically, the ^{30}Si count rate was converted in $^{30}Si_i$, which is proportional to the amount of plagioclase sputtered during the analysis. This conversion follows the equation $^{30}Si_i = {}^{30}Si\ \{(4/3) + 2X_{An}/3\}$ (cf. Charlier et al., 2012), where the $^{30}Si_i$ value accounts for the number of tetrahedral sites ablated during analyses, assuming constant ionization efficiency for Si. Therefore, the $^{7}Li/^{30}Si_i$ signal represents a value proportional to the molar Li content within the plagioclase, i.e. proportional to the number of Li atoms for tetrahedral site.

3.4 Geochemical and petrological characterization of volcanic rocks

3.4.1 Bulk rock geochemistry

To characterise the volcanic products within the period under investigation, whole rock geochemistry and petrography are provided for a total of 88 lava samples, which represent the sequence of paroxysms that occurred between January 2011 and April 2013 (data available at http://www.volcanology-unict.it/online_material/giuffrida_phd_thesis).

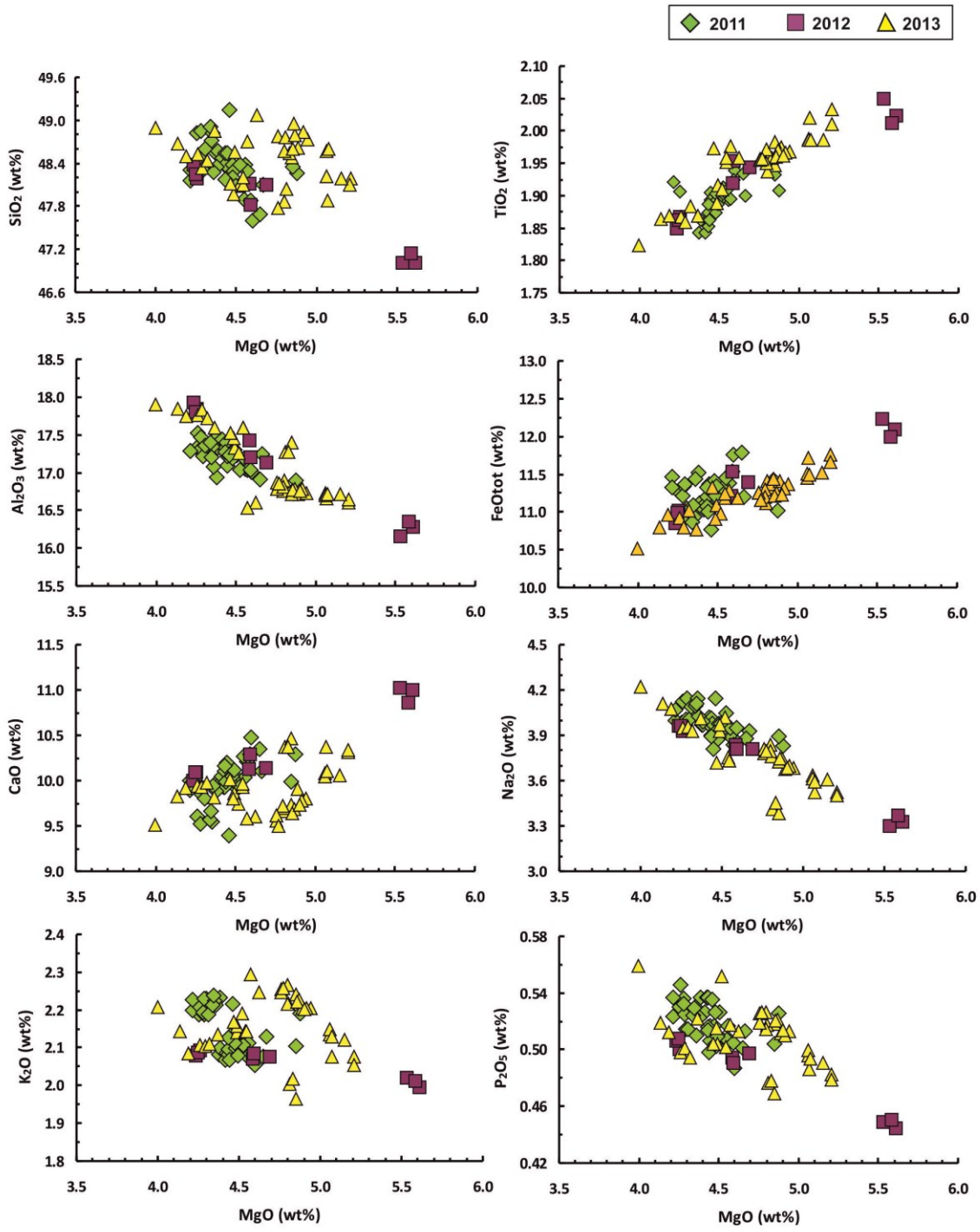

Figure 4. *Plots of major oxides vs. MgO (wt.%) for volcanic rocks erupted between January 2011 and April 2013 at Mt. Etna volcano.*

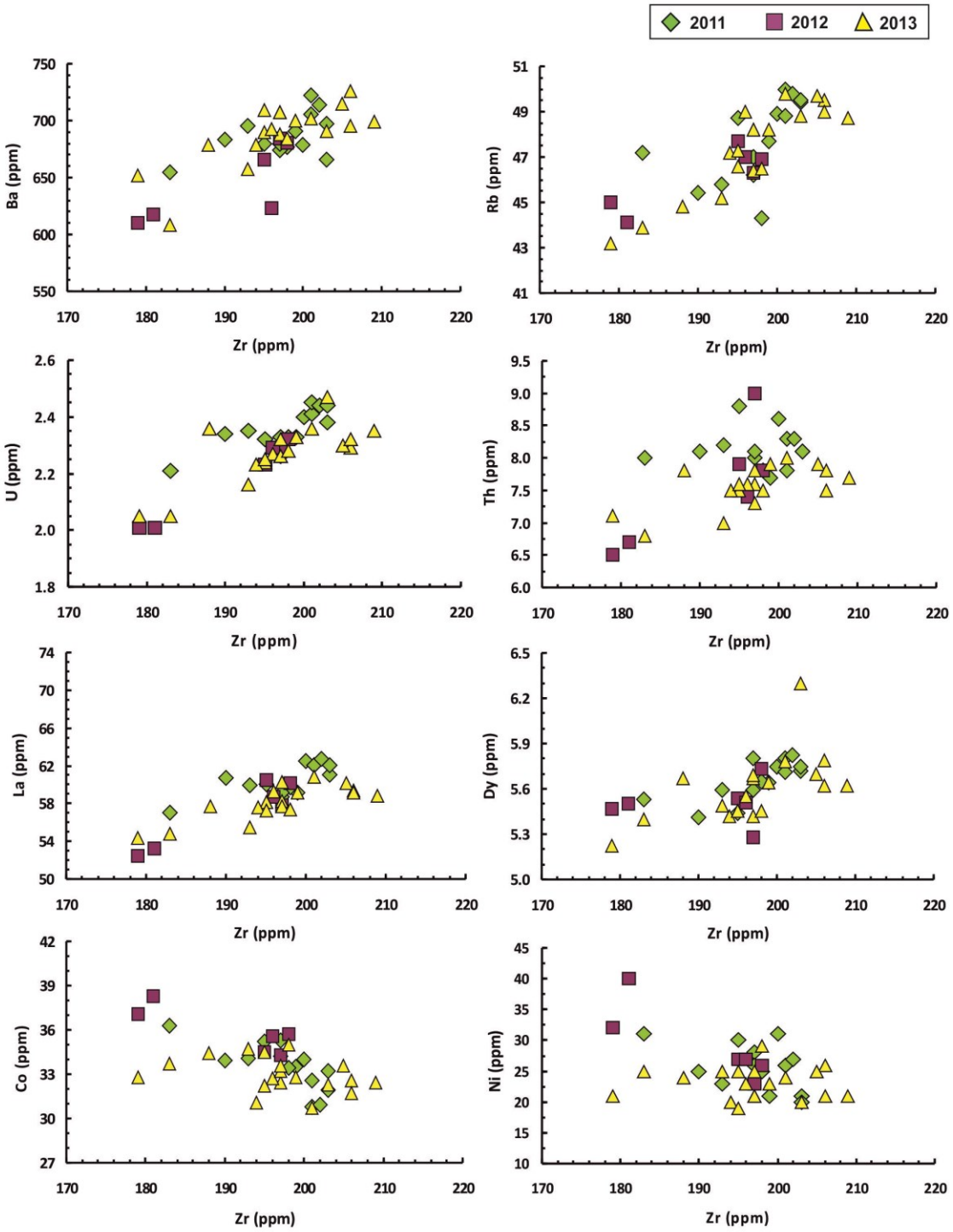

Figure 5. *Plots of trace elements vs Zr (ppm) for volcanic rocks erupted between January 2011 and April 2013 at Mt. Etna volcano.*

All samples fall within the K-trachybasalt field of the TAS diagram. To address the evolution of magmas throughout the period under investigation, the compositions of major oxides were plotted versus Mg (Fig. 4). TiO_2, FeO_{tot}, CaO display positive correlations with respect to MgO, whereas Al_2O_3, alkalis and P_2O_5 exhibit negative trends (Fig. 4). Trace elements were plotted versus Zr, which was used as differentiation index for its marked incompatibility in basaltic liquids. Large Ion Lithophyle Elements (LILE; Ba, Rb and, to a minor extent Sr), the High Field Strength Elements (HFSE; U, Nb and subordinately Th) and the group of Rare Earth Elements (REE) display positive correlations with Zr (Fig. 5). Only the transition metals (Co, Ni, V) show decreasing values at increasing Zr (Fig. 5). In spite of rather similar geochemical signatures, a more detailed analysis of major and trace element abundances reveals, however, the existence of some chemical differences over the considered period. For most of major oxides and trace elements, products related to the 2011 activity display chemical compositions with variations narrower than those of the 2012 and 2013 volcanic rocks (Figs. 4-5). Volcanic products of the 2011 episodes show also slight bimodality for K_2O contents, whereas the other elements are more clustered. Lavas and tephra of the 2012 activity present the widest compositional range compared to the products of the 2011 and 2013 paroxysms, and display the most basic compositions of 2011-2013 sequence, i.e. the samples from the March 04, 2012 eruption. Products of 2013 cover the most extensive range of compositions, but they do not reach compositions that are as basic as those observed in the 2012 paroxysmal samples (Figs. 4-5).

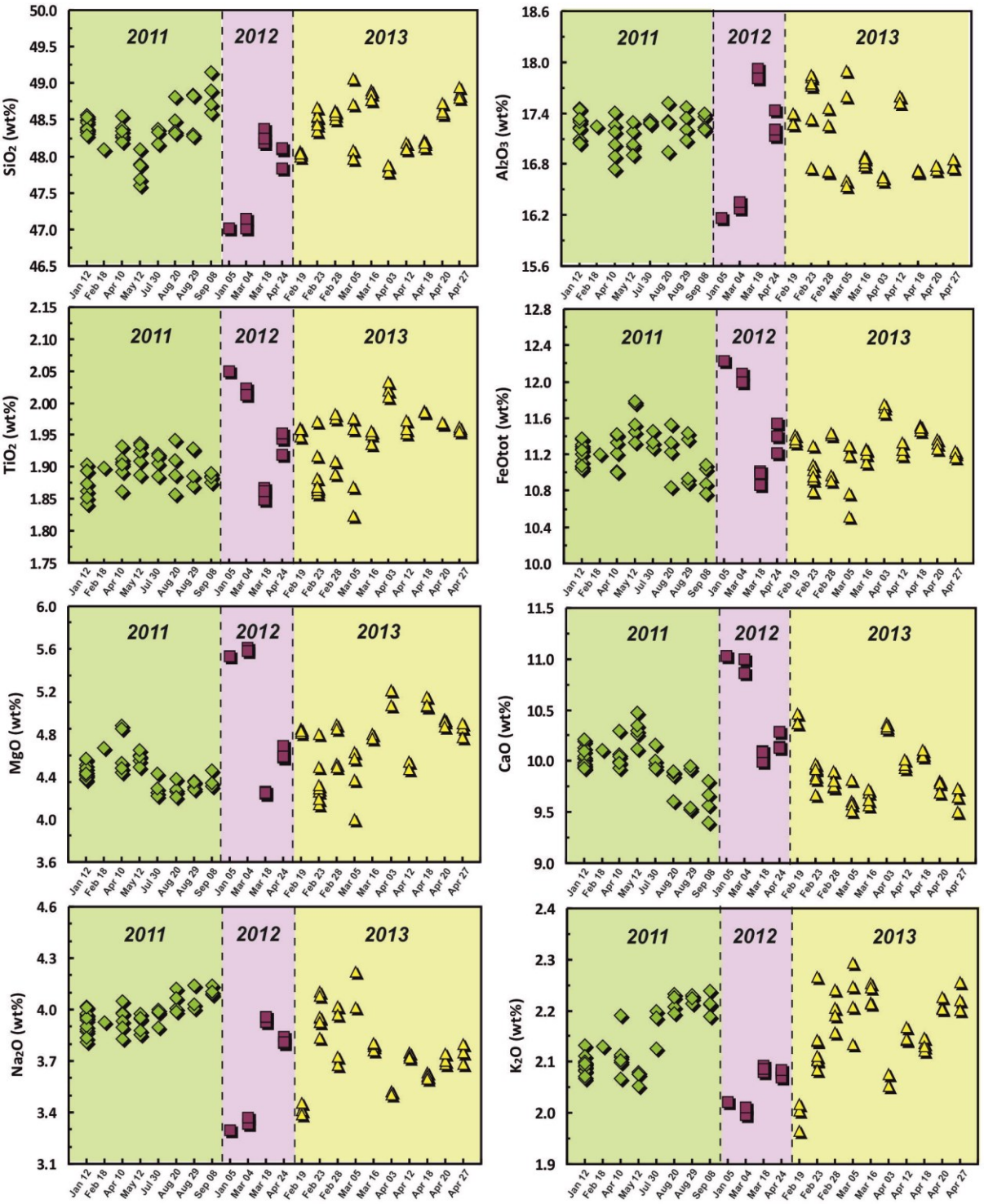

Figure 6. *Evolution of the major oxide compositions (wt. %) for the volcanic rocks erupted at Mt. Etna volcano throughout the period January 2011 and April 2013.*

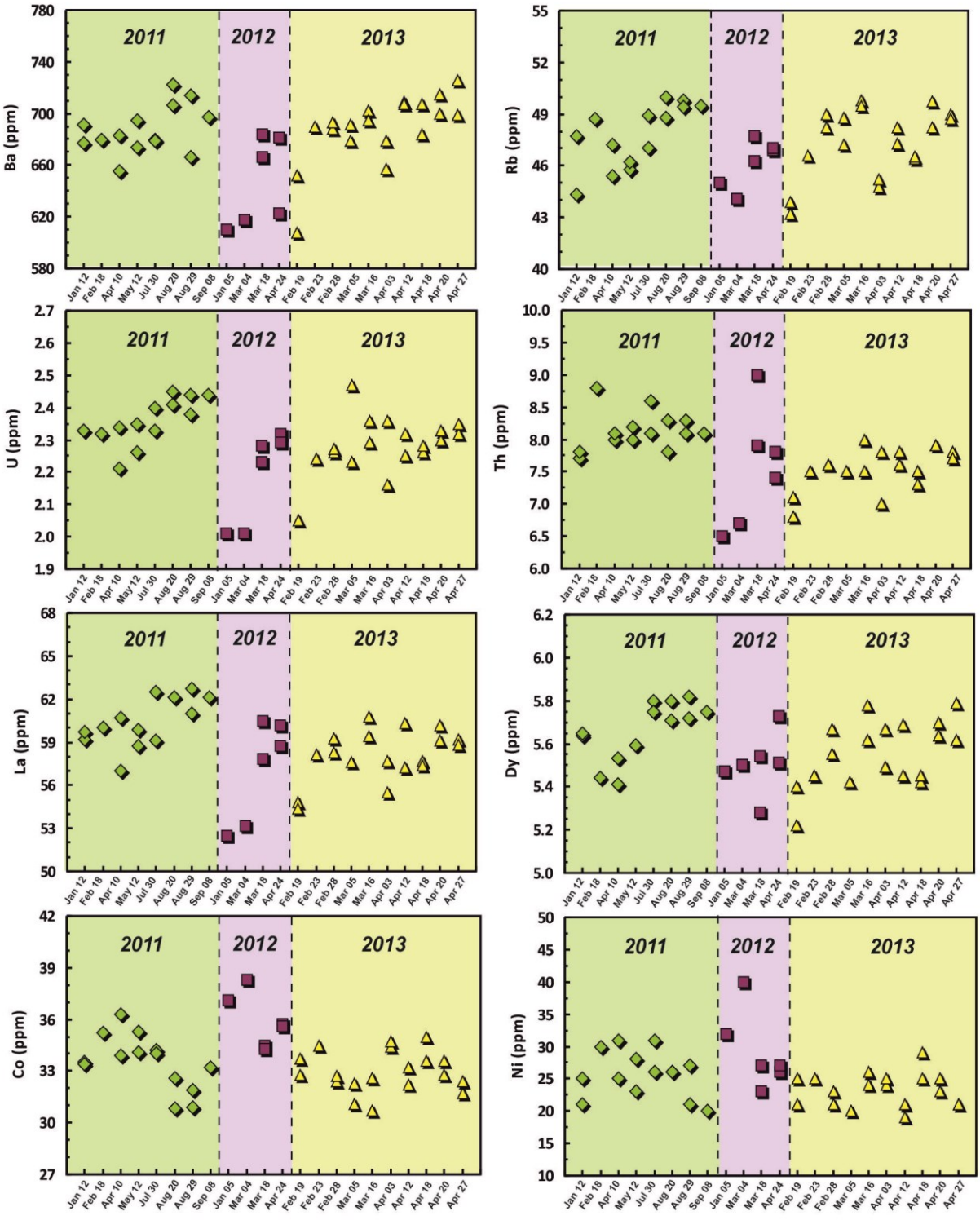

Figure 7. *Evolution of some selected trace element concentrations (ppm) for the volcanic rocks erupted at Mt. Etna volcano throughout the period January 2011 and April 2013.*

Figures 6 and 7 show the time evolution of some major oxides and trace elements for volcanic rocks at Mt. Etna throughout the period under investigation. Products of the 2011 activity become more MgO-rich from January to April, followed by shifting to more evolved compositions starting from May 2011. Volcanic rocks erupted during the period between July and September 2011 have more limited fluctuations maintaining, on the whole, rather constant compositions. Products erupted during the early episodes of 2012 are the most basic of the entire 2011-2013 sequence, but suddenly drop to compositions similar to those of the 2011 activity during the middle-late stage of the 2012 paroxysmal sequence. Reinitiation of volcanic activity on February 2013 yielded emissions of lavas and tephra fairly similar in their chemistry to those erupted during the final episodes of April 2012. For samples from February-March 2013 compositions are rather constant or slightly more evolved, whereas on April 3, the magma is the most basic of 2013. From that moment on, compositions tend to become progressively more evolved with only minor chemical changes (e.g., April 18, 2013; Figs. 6-7).

3.4.2 *Petrography and chemistry of minerals*

Volcanic rocks emitted at Mt. Etna during the 2011-2013 period display seriate porphyritic texture with the crystal fraction (Porphyritic Index in volume %) ranging between 15 and 30. The Porphyritic Index progressively decreases through time. Phenocrysts are included in a vitrophyric groundmass with transition to hyalopilitic texture. When microlites are present, they are generally acicular plagioclase, augitic clinopyroxene, subordinate olivine and opaque oxides. Mineral phases found as phenocrysts and their abundances related to the phenocryst fraction are: plagioclase (40-

60 vol.%), augitic clinopyroxene (30-50 vol.%), olivine (5-10 vol.%) and opaque oxides (<5 vol.%). Plots of compositions of the main mineral phases are shown in Figure 8.

Plagioclase is usually euhedral to subhedral, variable in size from micro-phenocryst (100-200 μm) up to 2-3 mm. Phenocrysts are characterized by a wide compositional and textural variability. Specifically, compositional oscillatory zoning typically occurs together with complex disequilibrium textures that characterize either the plagioclase core or rim. The anorthite content covers a wide range from andesine (An_{47}) to anorthite (An_{91}) during the considered eruptive period (Fig.8a). Crystals larger than 1 mm generally have more calcic core compositions (An up to 91 mol%) than small plagioclases, most of which have An between 55 and 65 mol%. Variations of the average core compositions throughout the entire period under investigation highlight major increases of An contents from February 18 to August 29, 2011 (An increases of ~25 mol%), and from February 23 to April 3, 2013 (An increases of ~10 mol%; Fig. 9a; cf. Viccaro et al., 2015). Conversely, cores of the crystals from the 2012 activity have, in average, less calcic compositions and record limited An fluctuations on the order of ~5 mol%. Plagioclase rims generally display the same trend as cores, although with lower An content (Fig. 9a). Details of textural features and An zoning patterns in plagioclase from selected episodes, together with variations of minor (Mg, Fe) and trace element (Sr, Ba) are described in the following section.

Clinopyroxene has euhedral to subhedral habitus and size between micro-phenocrysts (~100 μm) up to ~3 mm. Larger crystals with size >1 mm have been found either as single individuals or complex aggregates with the other mafic phases (olivine and oxides). The composition falls in the fields of diopside-salite and augite (Fig. 8b).

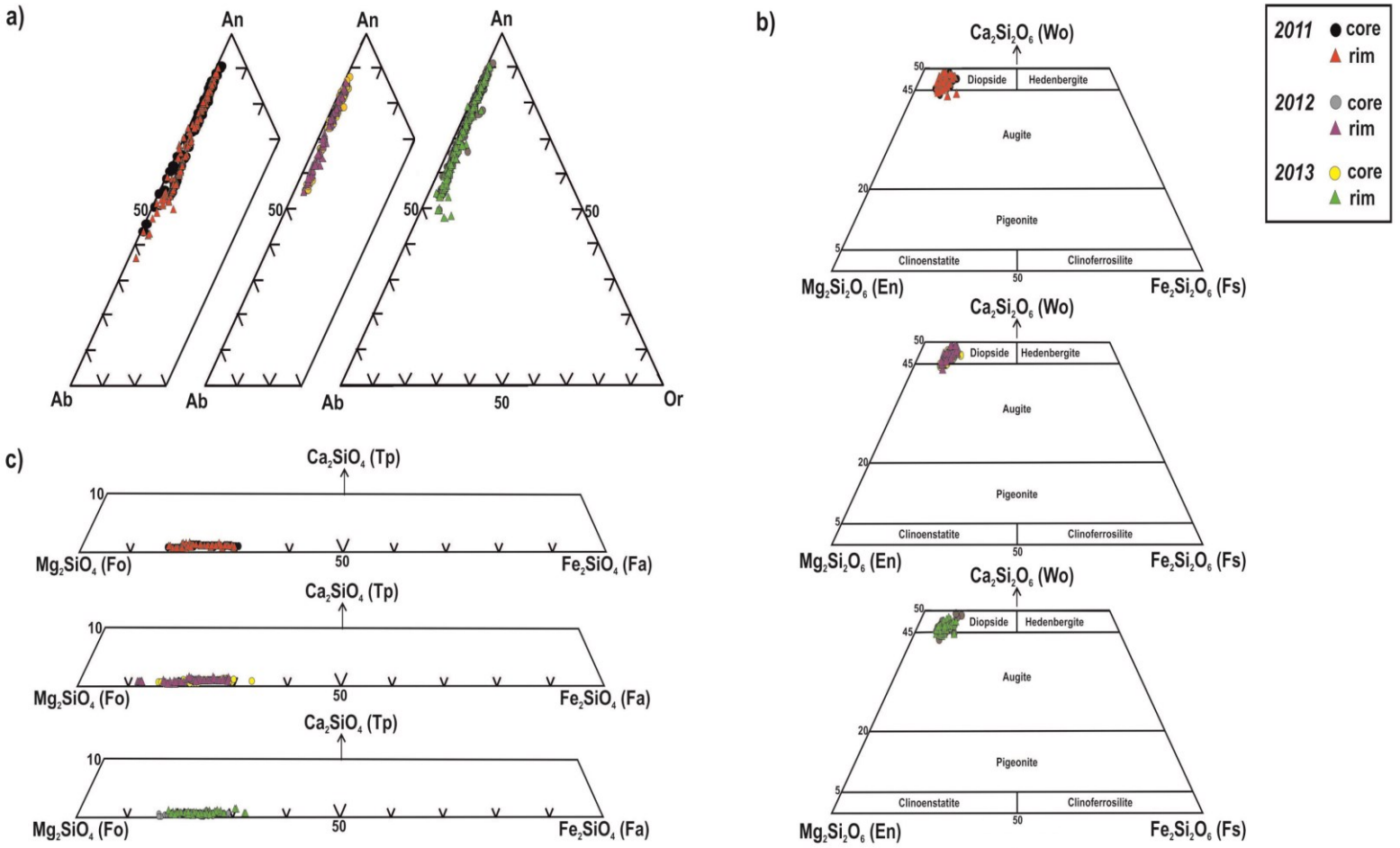

Figure 8. *Compositional variation of plagioclase, olivine and clinopyroxene in volcanic rocks of the 2011–2013 paroxysmal eruptions at Mt. Etna: a) plagioclase compositions within the Ab-An-Or diagram; b) clinopyroxene compositions in the QUAD diagram; c) forsterite – fayalite variation for olivine.*

Most of augitic crystals that were found in lava rocks from short-lasting paroxysmal eruptions (i.e. samples of March 4, 2012 and April 18, 2013) display resorption textures at the rim, similar to sieve textures. The average Mg# measured at the crystal core and rim has limited fluctuations throughout the entire 2011-2013 period (ΔMg# ~0.2; Fig. 9b). The main trends of increasing Mg# in the core (up to Mg# ~81) have been observed from May 12 to August 29, 2011, from March 4 to April 24, 2012, and finally from March 5 to the end of April 2013. Rims typically reveal Mg# higher than core (Fig. 9b).

Olivine is euhedral to subhedral. Sizes vary from micro-phenocrysts up to 1.4 mm. Some of the largest (>1.0 mm) olivine crystals are affected by strong disequilibrium, which manifests as embayments at their edge. It is worth noting that these olivine crystals generally coexist with destabilized clinopyroxene. The complete spectrum of olivine compositions covers the range between Fo_{70} and Fo_{84} (Fig. 8c). The core composition of olivine crystals shows great fluctuations during the 2011 and the 2013 eruptive periods (ΔFo 4-8), whilst crystals from the 2012 activity display more homogeneous compositions, which fall mainly in the range Fo_{75-80} (Fig. 9c). Based on compositions measured in the core, olivine crystals have been grouped into 5 populations, hereafter indicated as OP*i*, each one characterized by multiple zoning patterns. Section *3.5* provides a detailed description of the identified populations and their chemical zoning.

Opaque oxides have subhedral to anhedral habitus and are between 50 and 200 μm. Measured compositions allow their classification as titaniferous magnetite (cf. Viccaro et al., 2015). They are typically enclosed in olivine and clinopyroxene, testifying their early nucleation and growth. Textural relationships among phenocrysts suggest that,

after the early crystallization of titaniferous-magnetite, crystallization proceeded from olivine and clinopyroxene to plagioclase.

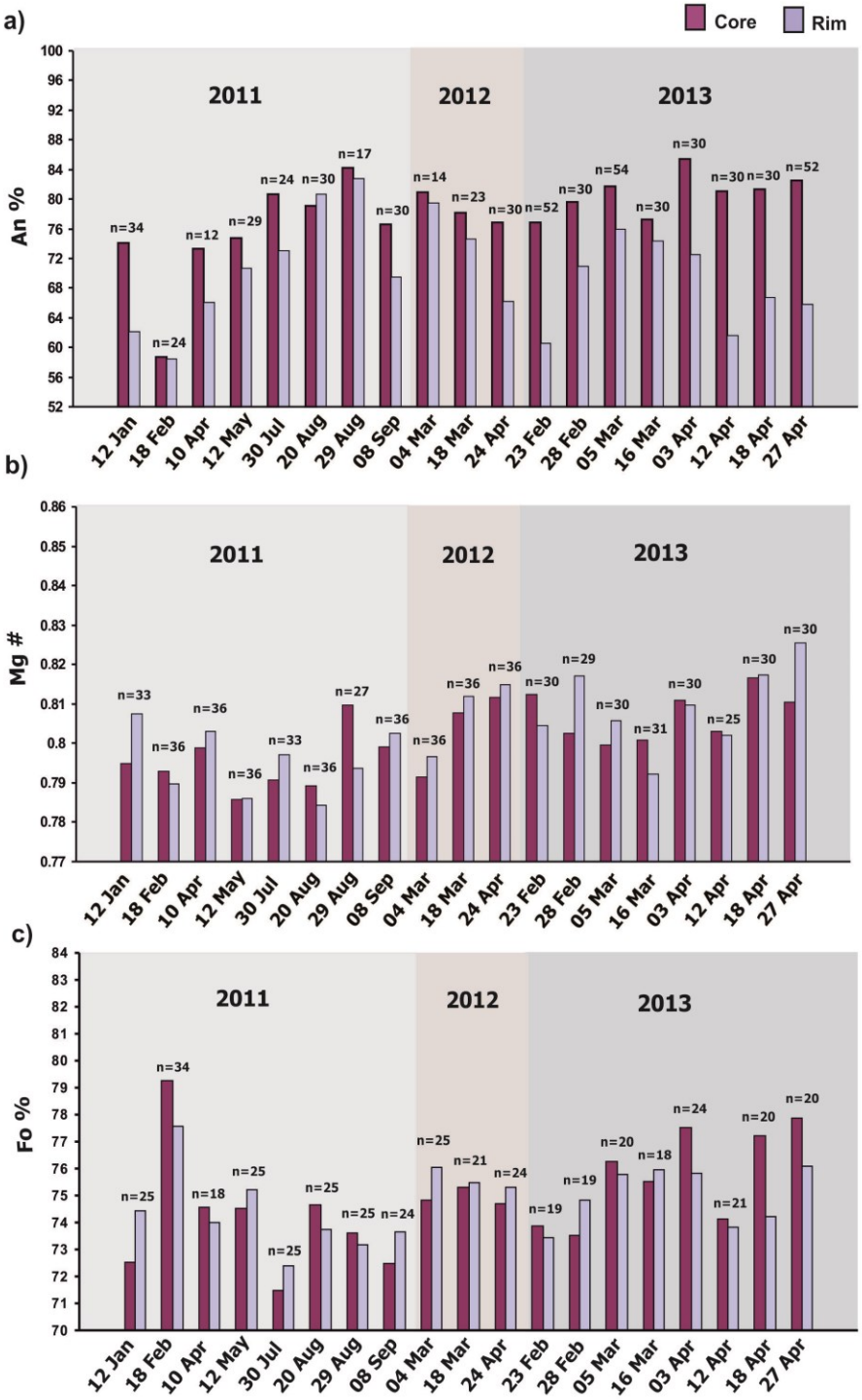

Figure 9. *Compositional variation throughout the January 2011 – April 2013 period of the average An contents in plagioclase, Fo in olivine and Mg# in augitic clinopyroxene. n:number of spot analyses collected at the core and rim of crystals.*

3.5 Textural and compositional features of plagioclase and olivine crystals

3.5.1 Plagioclase textures

The systematic study under optical and electron microscope of the products erupted at Mt. Etna during the 2011-2013 period of activity illustrates considerable differences concerning the plagioclase textures. The plagioclase assemblage is represented by several textures in variable proportion: oscillatory zoning, core disequilibrium textures (mainly coarse sieve-textures, strong dissolution/resorption), sieve texture at the rim, and other textures that indicate crystal growth at different degrees of undercooling (Viccaro et al., 2010; 2014; 2015; Nicotra and Viccaro, 2012a; 2012b). The frequency of occurrence of each plagioclase texture in volcanic products for the 10 selected episodes during the 2011-2013 period is shown in Figure 10. BSE images of some of the most representative growth and disequilibrium textures of plagioclase are also provided in Figures 11 (growth textures) and 12 (disequilibrium textures).

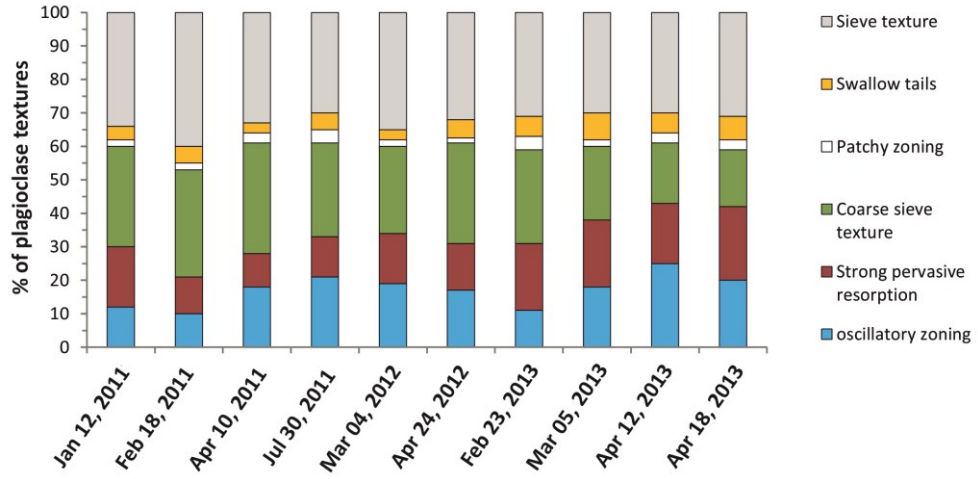

Figure 10. *Percentages of frequency of plagioclase textures in volcanic products for selected paroxysmal eruptions (oscillatory zoning includes both large- and small-scale patterns).*

Crystals with oscillatory zoning exhibit small (< ΔAn5 compositional variations with short ~10 μm wavelength) and large (~ΔAn5–10 and 20-30 μm wavelength) scale oscillations of the anorthite content that are similar to those already identified for other plagioclases of the recent post-1971 Etnean activity (cf. Viccaro et al., 2010, Nicotra and Viccaro, 2012a; Fig. 11). As a whole, small scale oscillatory zoning commonly pertains to microphenocrysts (100-200 μm size) and cores of large phenocrysts (> 1mm), whereas the large scale oscillation patterns occur with higher frequency in small and medium size crystal cores (200-600 μm size) or at the rims of the larger crystals. These different oscillation patterns can also occur within the same crystal (Fig. 11). Plagioclase characterized exclusively by oscillatory zoning composes approximately 10-20 % of the total crystals observed (Fig. 10) and they are found in all crystal sizes, but are more abundant in microphenocrysts. It is worth noting that the occurrence of large (1.0-1.5 mm) totally oscillatory zoned crystals is limited to few lava samples, e.g. those erupted on March 5-6, 2013. Detailed observations of BSE images reveal that the large-scale oscillatory zoning is commonly interrupted by minor wavy dissolution surfaces (Fig. 11). Moreover, oscillatory-zoned portions of plagioclase are often cross-cut by disequilibrium textures affecting both cores and rims.

Disequilibrium textures at the plagioclase cores show a different pervasive degree of resorption (Fig. 12). Among the more abundant textures are crystals strongly affected by pervasive dissolution/resorption (Fig. 12a) and crystals with coarse-sieve textures (Fig. 12b.). In these cases, evidence for crystal resorption is given by the occurrence of micron-sized glass inclusions randomly distributed within the cores, which generally acquire a rounded shape (Tsuchiyama 1985; Kawamoto 1992; Nakamura and Shimakita, 1998).

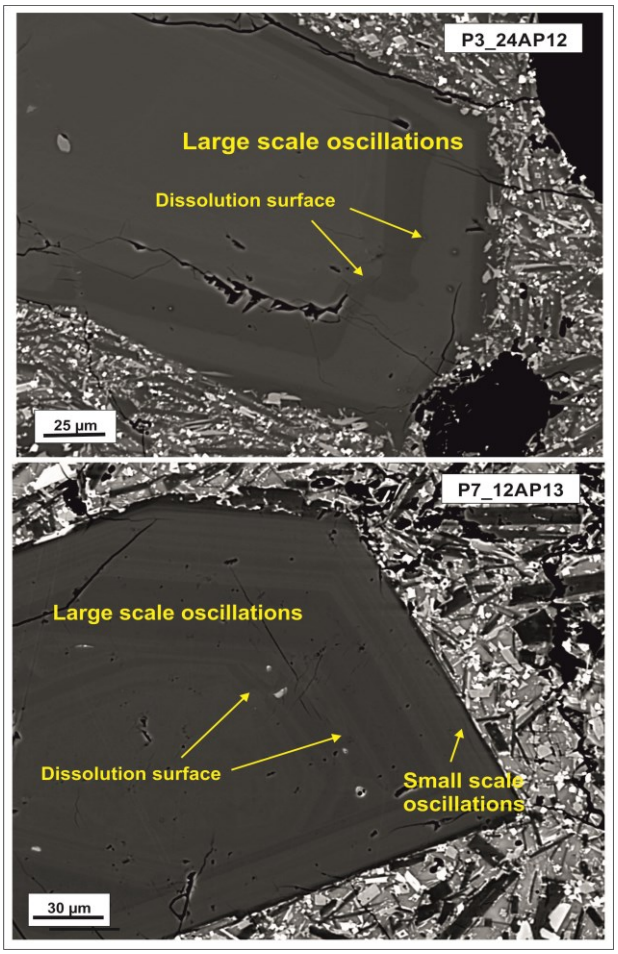

Figure 11. *Examples of coexistent small and large scale oscillatory zoning patterns in plagioclase crystals of the 2011-2013 paroxysmal activity. Note the occurrence of irregular surfaces due to minor dissolution events that affect the large scale zoning. All photos by BSE scanning electron microscope.*

Both textures mainly affect plagioclase of medium-large size (>500 µm). Coarse-sieve textures occur with high frequency around 30–40%, whereas crystals with strongly resorbed cores (i.e., strong pervasive resorption) compose about 20 % of the textures in plagioclase crystals (Fig. 10). Plagioclase cores are also characterized by textures similar to patchy zoning found in plagioclase crystals from past eruptions (cf. Viccaro et al., 2010; Nicotra and Viccaro 2012a), in which it has been recognized An-richer and An-

poor areas that are arranged in irregular patches (Fig. 12c-d). This feature is, however, rather unusual in the products under investigation, representing ~2-4 % of the plagioclase textures in observed crystals (Fig. 10).

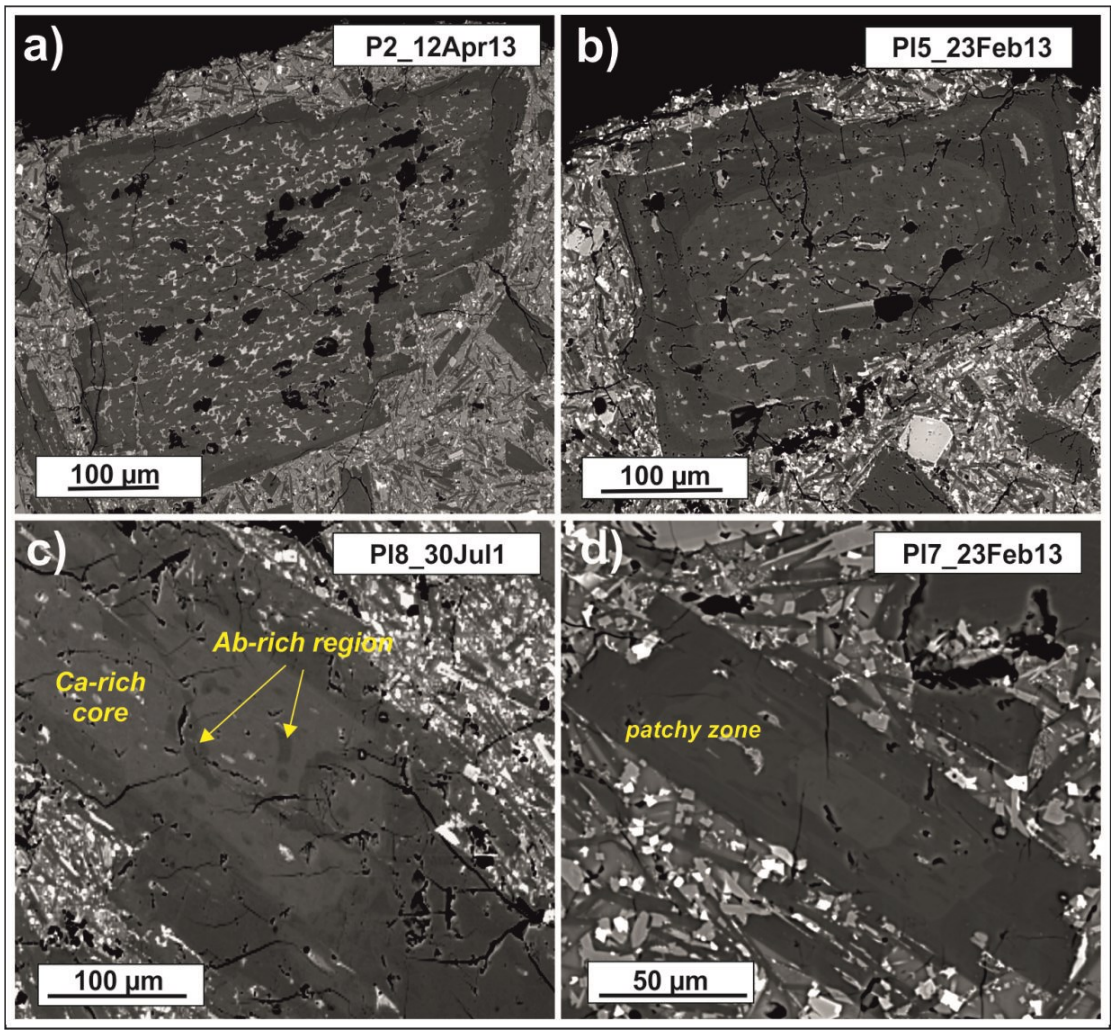

Figure 12. *Example of disequilibrium textures in plagioclase crystals of the 2011-2013 paroxysmal activity. a) plagioclase crystal with core affected by strong resorption; b) crystal showing a coarse-sieve textured core with rounded edge and sieve texture at the rim; c) patchy core characterized by zones at different composition. Darker areas have less calcic composition; d) another example of plagioclase with textures similar to patchy zoning. The crystal shows an oscillatory zoning core mantled by a patchy region with Ca-rich (light areas) and Ca-poor (dark areas) zones;*

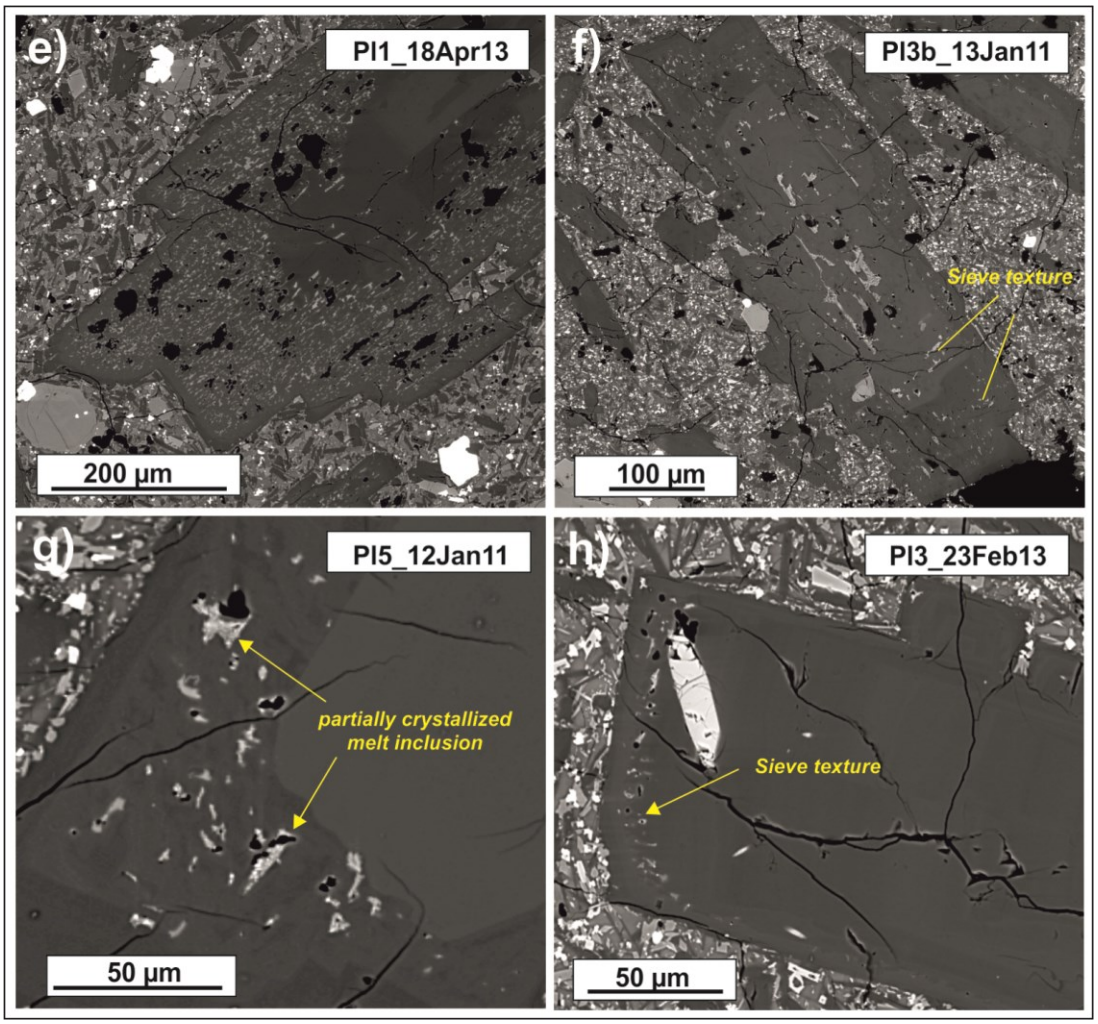

Figure 12 (continue). *Example of disequilibrium textures in plagioclase crystals of the 2011-2013 paroxysmal activity. e) plagioclase rim with extensive dusty sieve textures; f) complex plagioclase crystal displaying several type of disequilibrium features: the core has coarse-sieve texture and rounded shape; rims are affected by a double sieve texture; g) detail of a sieve texture surrounding a plagioclase core; h) example of an incipient sieve texture at the rim of an oscillatory zoned plagioclase crystal.*

Disequilibrium textures at the rim of plagioclase are present in all of the volcanic rocks under investigation, and affect crystals with very different sizes. In these cases, the rim of crystals is marked by sieved zones characterized by bands of glass inclusions usually cross-cutting the oscillatory zoning patterns (Fig. 12e-h). Some crystals also exhibit multiple sieved regions, sometimes evolving into dusty, thick textures with

interconnected melt channels (Fig. 12f). The frequency of sieve texture is between 30 and 40% of the total crystal fraction (Fig.10) and is typical of medium and large size crystals. Microphenocrysts usually exhibit slighter resorption than larger plagioclase phenocrysts, showing thin (15-25 μm large) sieve textures at the outermost rim (Fig. 12g-h).

3.5.2 Minor and trace element zoning in plagioclase and their relation with major element variations

Five to ten representative plagioclase phenocrysts were analyzed for major and minor elements by SEM-EDS in each selected sample; in addition, about a half of crystals was also analyzed for trace elements by laser ablation ICP-MS (compositions available at http://www.volcanology-unict.it/online_material/giuffrida_phd_thesis). Most of the Etnean plagioclase are characterized by multiple and extensive resorption zones both at their core and rim; for this reason, the collection of trace elements was limited to crystals wholly oscillatory-zoned or to portions of plagioclase not severely affected by μm-sized glass inclusions caused by disequilibrium. In this section, the anorthite zoning is described together with variations of some minor elements, e.g., Fe and Mg, and the Sr/Ba ratios for plagioclase crystals having different textures. It is worth noting that Mg contents in the Etnean plagioclases are usually lower than 0.8 wt.%. Therefore, in this study the Mg concentrations are evaluated in ppm, by taking into account values obtained by LA-ICP-MS that are more precise than data produced by SEM-EDS/WDS.

In oscillatory-zoned crystals, the anorthite content covers a wide range of composition from An_{55} to An_{91}. At the core of microphenocrysts An ranges from 55 to 70

mol%, with subordinate more calcic compositions of An 79-86 mol % (only 3 plagioclases within the whole population of oscillatory-zoned microphenocrysts; Fig. 13).

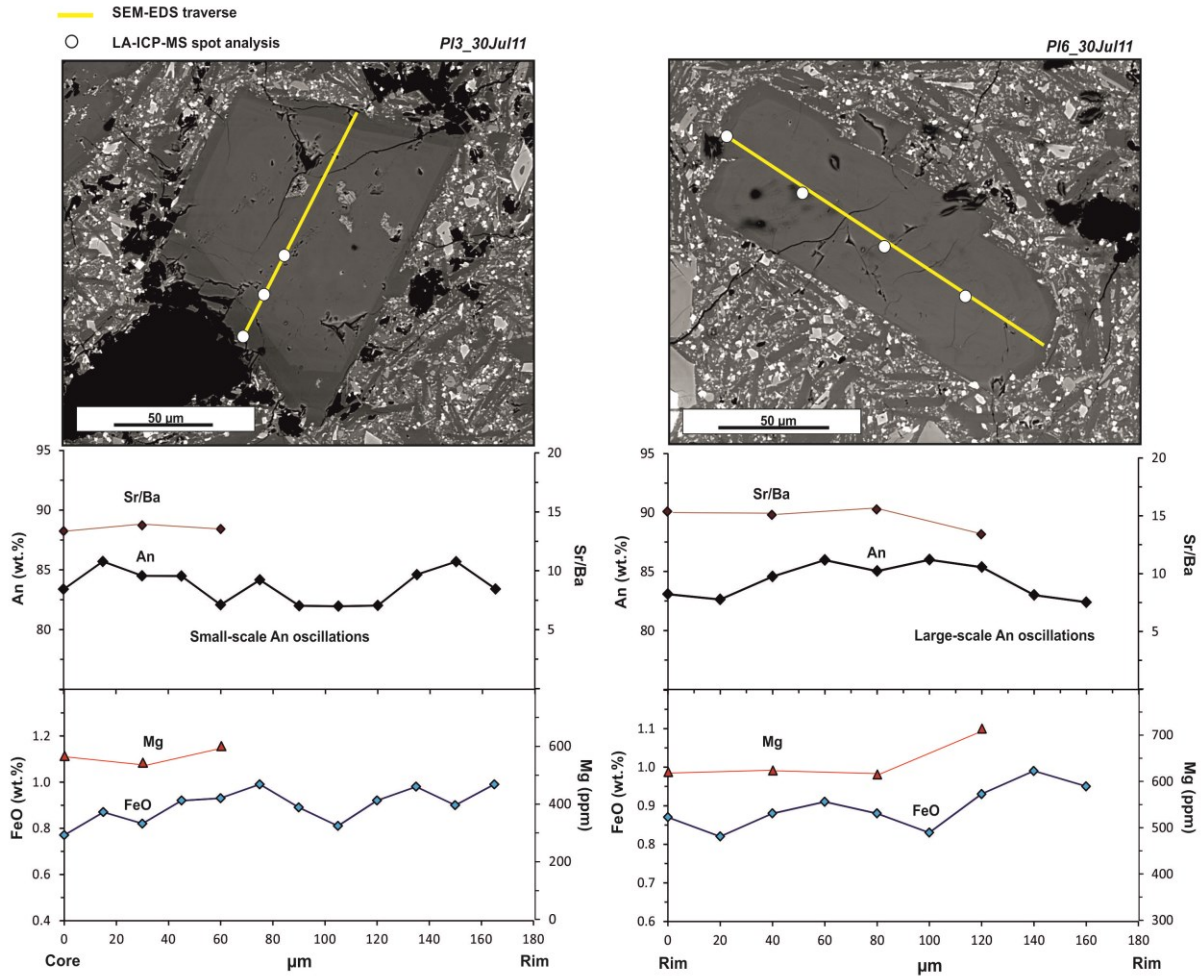

Figure 13. *Compositional characteristics of oscillatory-zoned plagioclase microphenocrysts. In diagrams the An zoning (mol%) is shown together with FeO (wt.%), Mg (ppm) and Sr/Ba profiles. Filled black diamonds: An mol %; filled brown diamonds: Sr/Ba ratio; filled blue diamonds: FeO wt.%; red triangles: Mg ppm.*

Oscillatory-zoned cores of plagioclase with size between 200 and 600 µm show two distinct dominant compositions at An 79-91 (Fig. 14) and An 55-70 mol % (Fig. 15). The

most calcic core compositions of 85-91 mol % were generally found in plagioclase crystals larger than 600 µm (Fig. 16). For all the analyzed crystals, also belonging to different size classes, FeO and Mg do not record important variations. FeO typically ranges between 0.50 and 1.20 wt. % at the core, whereas Mg varies between 370 and 790 ppm (Fig. 13-16).

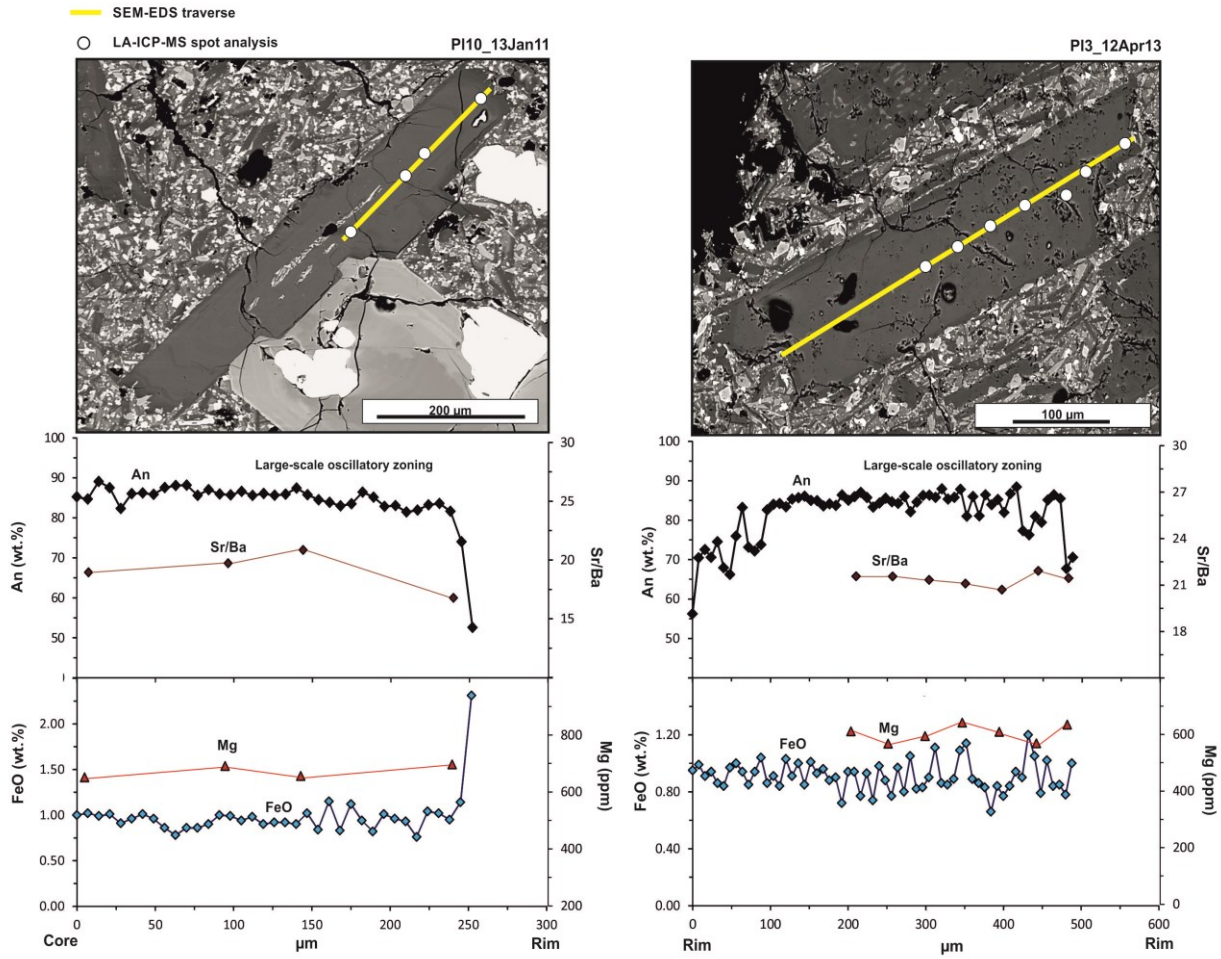

Figure 14. *Compositional characteristics of oscillatory-zoned plagioclase crystals with size between 200 and 600 µm, having low calcic core composition. In diagrams, the An zoning (mol%) is shown together with FeO (wt.%), Mg (ppm) and Sr/Ba profiles. Filled black diamonds: An mol %; filled brown diamonds: Sr/Ba ratio; filled blue diamonds: FeO wt.%; red triangles: Mg ppm.*

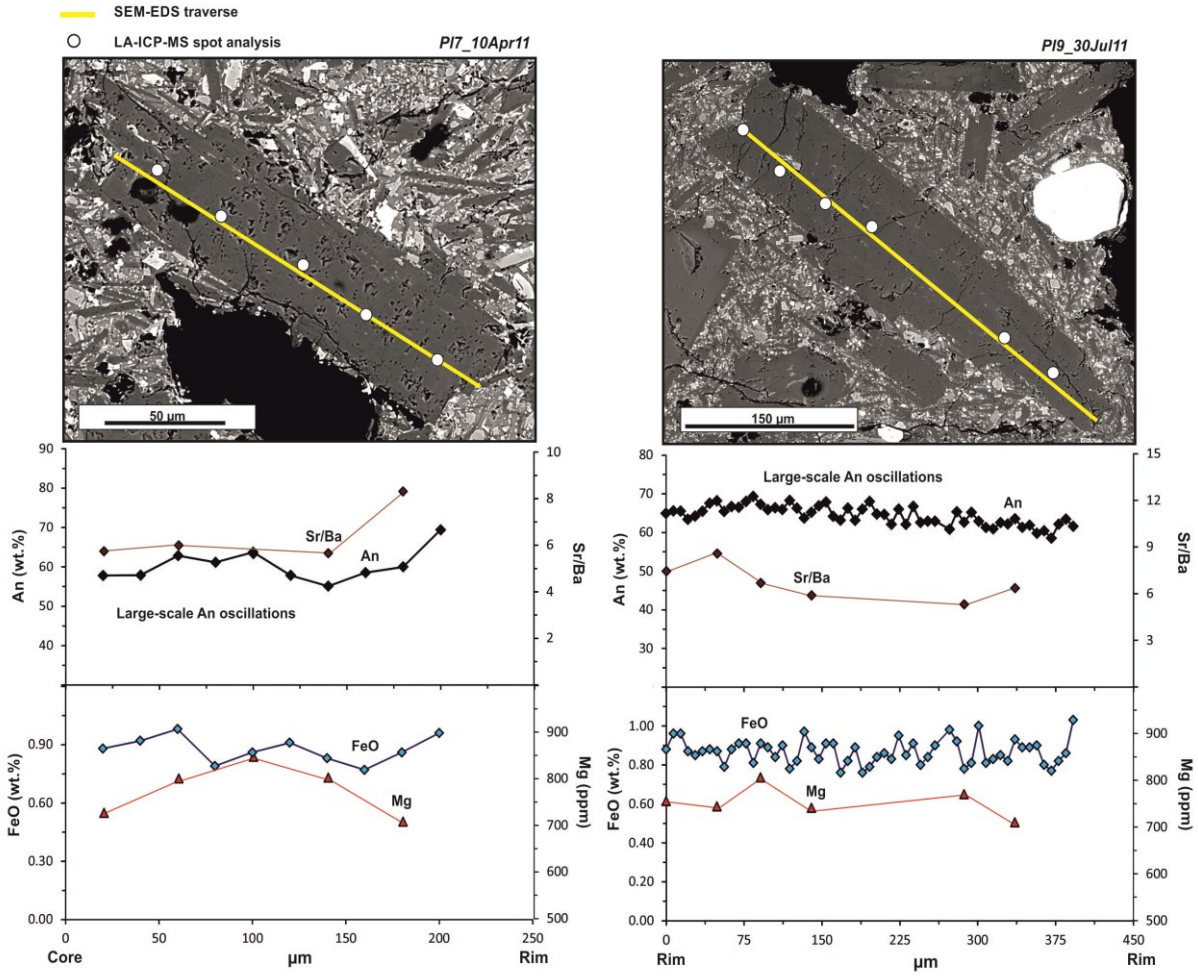

Figure 15. *Compositional characteristics of oscillatory-zoned plagioclase crystals with size between 200 and 600 µm, having low calcic core composition. Diagrams show the An zoning(mol%) together with FeO (wt.%), Mg (ppm) and Sr/Ba zoning patterns. Filled black diamonds: An mol %; filled brown diamonds: Sr/Ba ratio; filled blue diamonds: FeO wt.%; red triangles: Mg ppm.*

Some of the oscillatory-zoned crystals also show a concomitant enrichment of these two elements in the outermost 10-50 µm of the rims, where FeO and MgO display reverse zoning patterns, with concentrations up to ~2.0 wt.% and 790 ppm respectively. As a whole, the small-scale anorthite zoning of plagioclase generally forms concordant trends

with FeO and MgO variations, whereas anorthite fluctuations forming large-scale zoning patterns are concordant with MgO and discordant with respect to FeO variations.

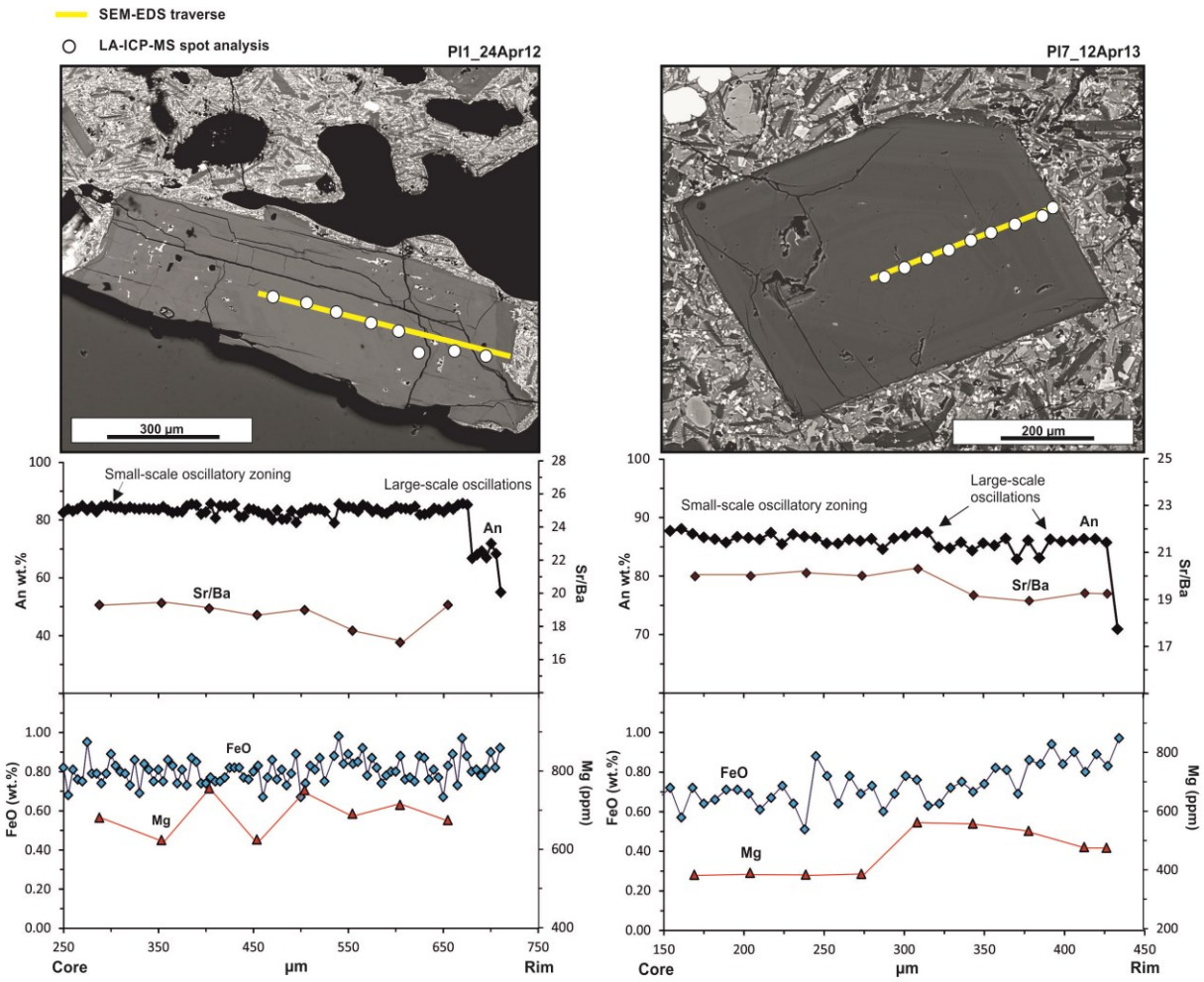

Figure 16. *Compositional characteristics of oscillatory-zoned plagioclase crystals with size >600 µm. Diagrams show the An zoning (mol%) together with FeO (wt.%), Mg (ppm) and Sr/Ba compositions. Filled black diamonds: An mol %; filled brown diamonds: Sr/Ba ratio; filled blue diamonds: FeO wt.%; red triangles: Mg ppm.*

Trace elements measurements across the oscillatory-zoned portions of plagioclase highlight marked difference in the average Sr/Ba ratios of these crystals. Most of the Etnean plagioclase crystals have Sr/Ba fluctuations between 15 and 32 (average Sr/Ba

ratios ~23), however, some crystals display a significantly lower Sr/Ba ratio at comparable An content (average Sr/Ba ratio ~8; Fig. 17). In particular, the average Sr/Ba ratio is lower for products erupted during the 2011 period of activity, from February 2011 to July 2011, and then increased throughout the 2012 and 2013, showing low values only in crystals from the February 23, 2013 eruption and March 04, 2012 (Fig. 17).

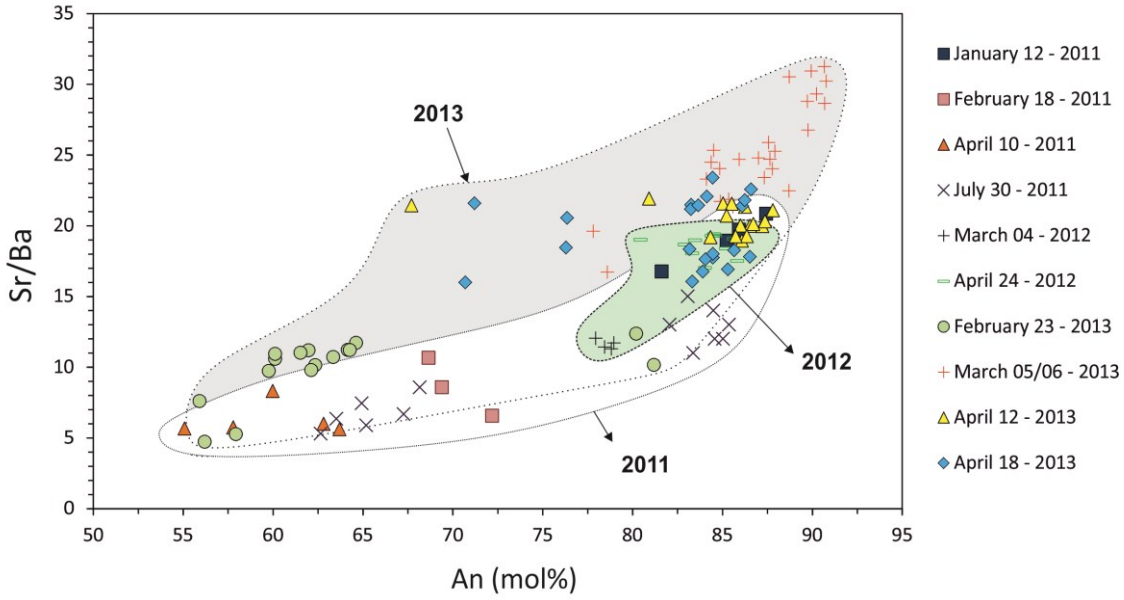

Figure 17. *Sr/Ba ratio plotted against An for oscillatory-zoned plagioclase crystals of the 2011-2013 activity at Mt. Etna. White Area: crystals of the 2011 eruptions; light green area: crystals of the 2012 eruptions; gray area: crystals of the 2013 eruptions.*

Crystals with disequilibrium textures in the core have average An values ~ 80-85 mol%, which are fairly constant throughout the zone of disequilibrium (Fig. 18). In some circumstances, crystals with marked rounding of the core present a sudden drop of anorthite (ΔAn ~20-30) just outboard of the resorption surface (Fig. 18). Iron and Mg display variations within a narrow range ((FeO ~0.4–1.2 wt.%, MgO ~400-650 ppm; Fig.

18). Within the patchy cores of the crystals, the An content does not show abrupt compositional shift, rather An varies in a range of 10-15 mol% and FeO variations are generally discordant relative to An (Fig. 19). The average Sr/Ba ratios within cores of crystals affected by disequilibrium textures are generally higher than 16, though few analytical spots at low (<10) Sr/Ba has been also observed in crystals emitted during paroxysmal episodes of 2011 (Fig. 18; see online material at http://www.volcanology-unict.it/online_material/giuffrida_phd_thesis)

.

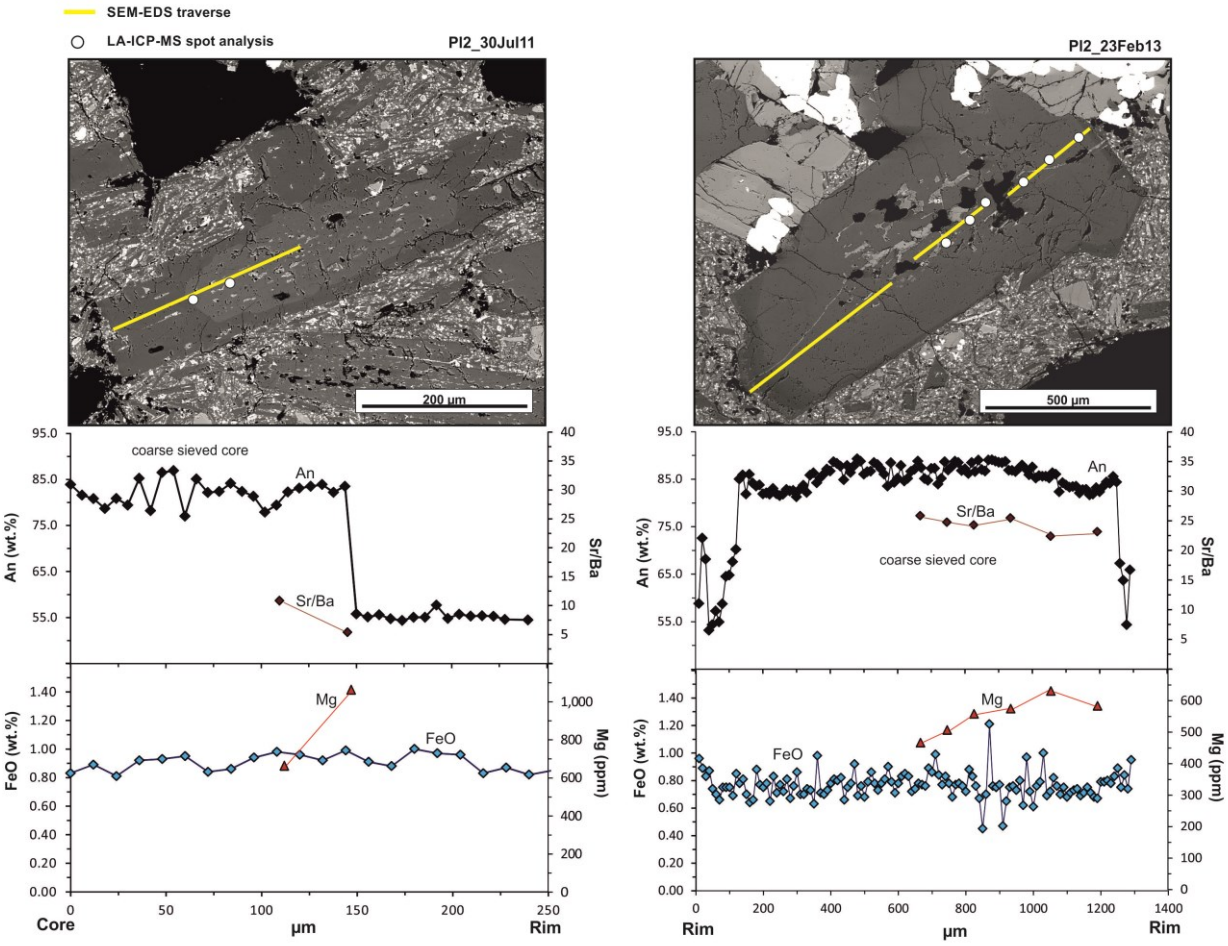

Figure 18. *Plagioclase crystals affected by coarse-sieve textures at the core and their associated An (mol%), FeO (wt.%), Mg (ppm) and Sr/Ba zoning patterns. Filled black diamonds: An mol %; filled purple diamonds: Sr/Ba ratio; filled blue diamonds: FeO wt.%; red triangles: Mg ppm.*

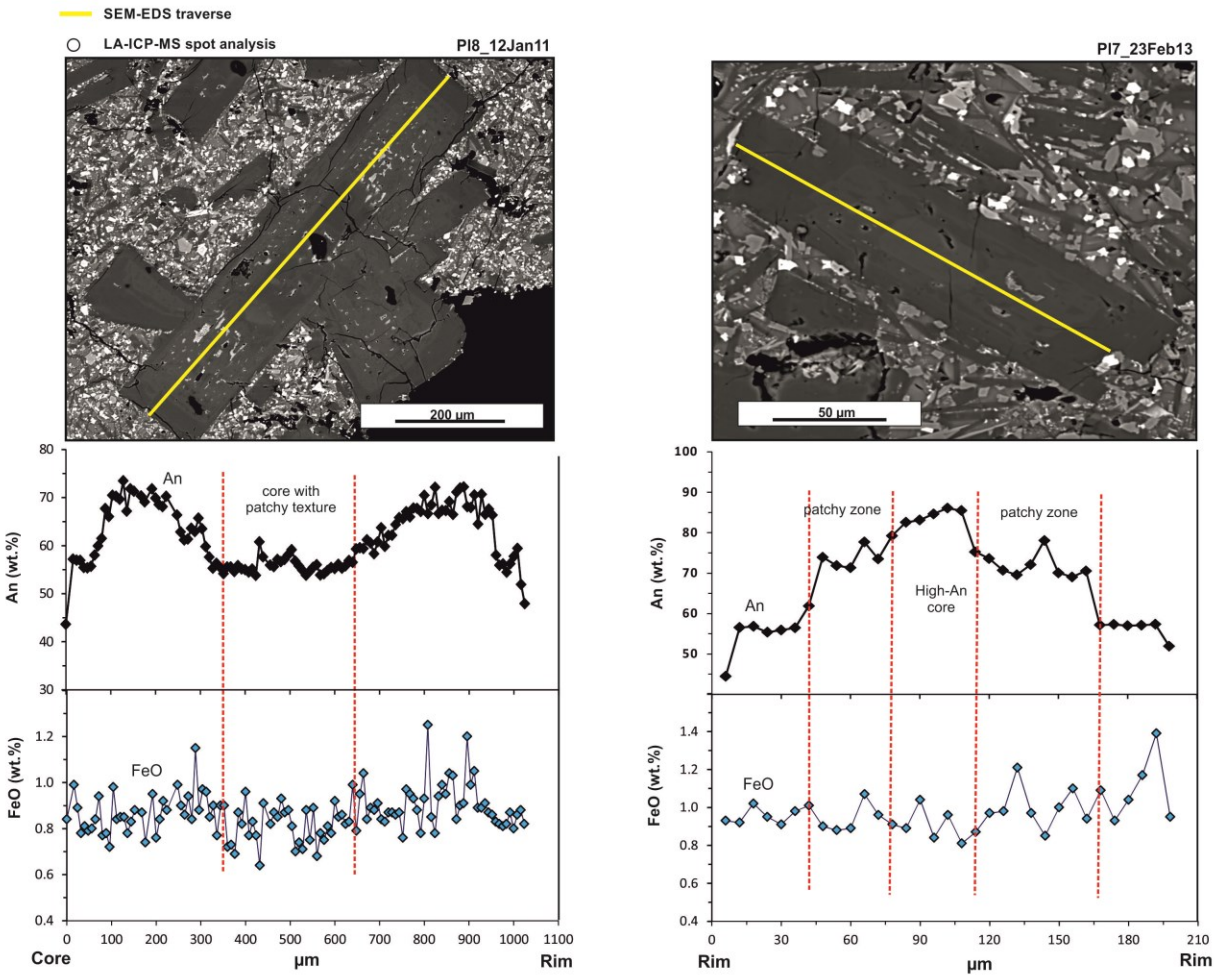

Figure 19. *Plagioclase crystals with patchy textures at the core and their associated An (mol%), FeO (wt.%) zoning patterns. Note that for most of the the crystals, such as those showed in BSE images, Mg (ppm) and Sr/Ba values were not measured. Filled black diamonds: An mol %; filled blue diamonds: FeO wt.%.*

In sieve-texture regions developed at the rim of plagioclase crystals, anorthite and iron show different trends of variation. Some crystals display concomitant increase of An (up to ~ΔAn_{20} mol%) and FeO (up to ΔFeO ~0.4 wt.%) within the sieved rims (Fig. 20). Moreover, in those crystals where collection of La-ICP-MS spot analyses was possible, an increase of Mg was also detected within these high Fe-An sieved zones (Fig. 20).

These compositional variations associated with the sieved rims are typical of crystals found in lavas emitted during long-lasting paroxysmal eruptions, which are also characterized by a low rate of volcanic tremor amplitude increase (see Table 2; cf. Viccaro et al., 2014). Other crystals with sieved textures at the rim show discordant trends of anorthite and iron, with An rather constant or slightly decreasing and FeO that increases (up to ΔFeO ~0.3 wt.%; Fig. 21). This compositional feature in plagioclase sieved rims is commonly related to plagioclases of lavas erupted during events characterized by a rapid temporal evolution, which had a high rate of increase in volcanic tremor amplitude (see Table 2; c.f. Viccaro et al., 2014). In these cases, Mg contents within the sieve textures vary in discordance with iron, showing decreasing concentrations. Due to the pervasive presence of glass inclusions, measurements of trace element concentrations were often not possible across sieve textures, so that changes in Sr/Ba ratios along sieve textures were not evaluated.

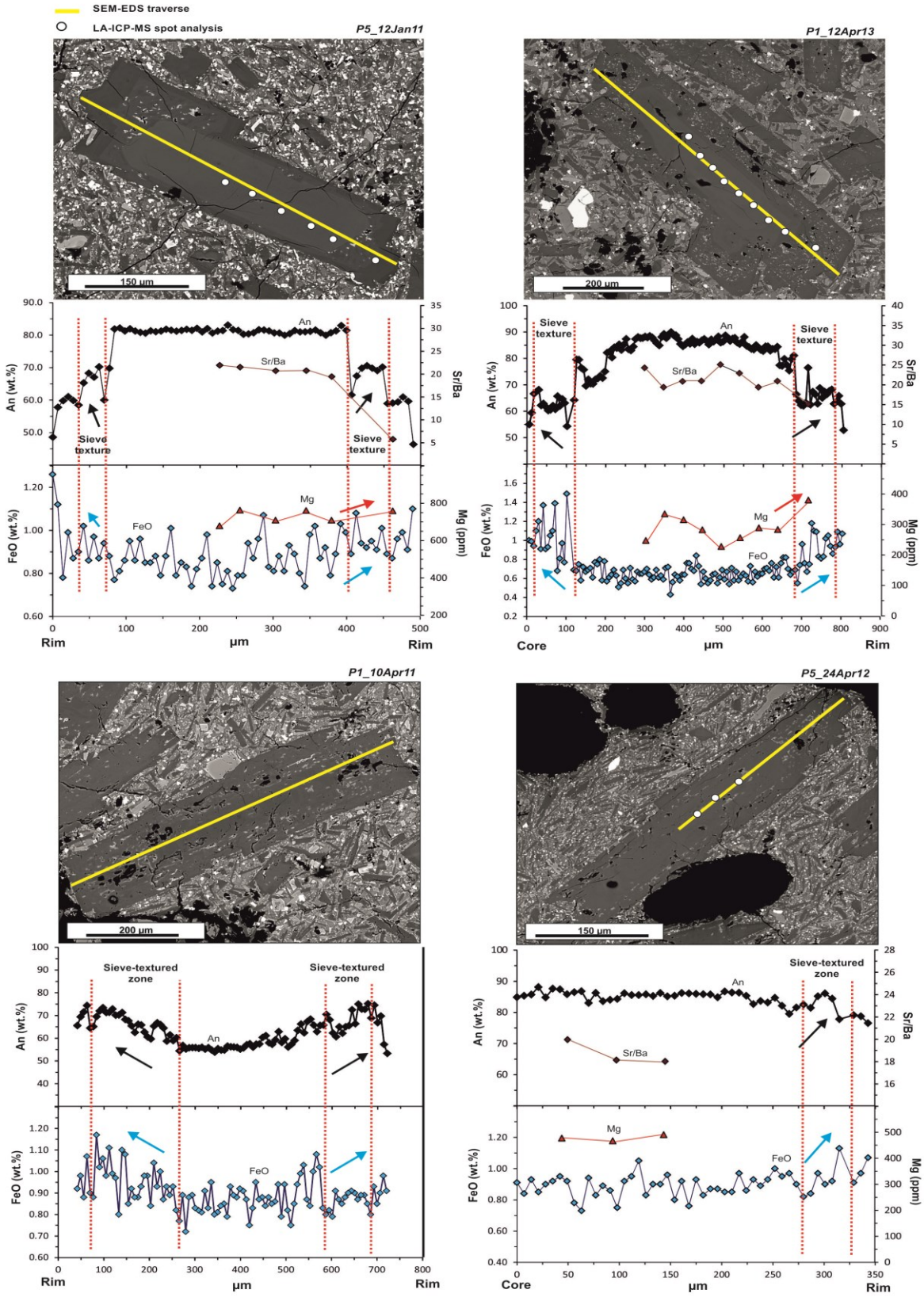

Figure 15. *Plagioclase crystals affected by disequilibrium textures at the rim and their associated An (mol%), FeO (wt.%), Mg (ppm) and Sr/Ba zoning patterns. Filled black diamonds: An mol %; filled brown diamonds: Sr/Ba ratio; filled blue diamonds: FeO wt.%; red triangles: Mg ppm. Diagrams show the type of sieve textures (areas within dotted lines) characterized by coupled increase of FeO, Mg and An contents.*

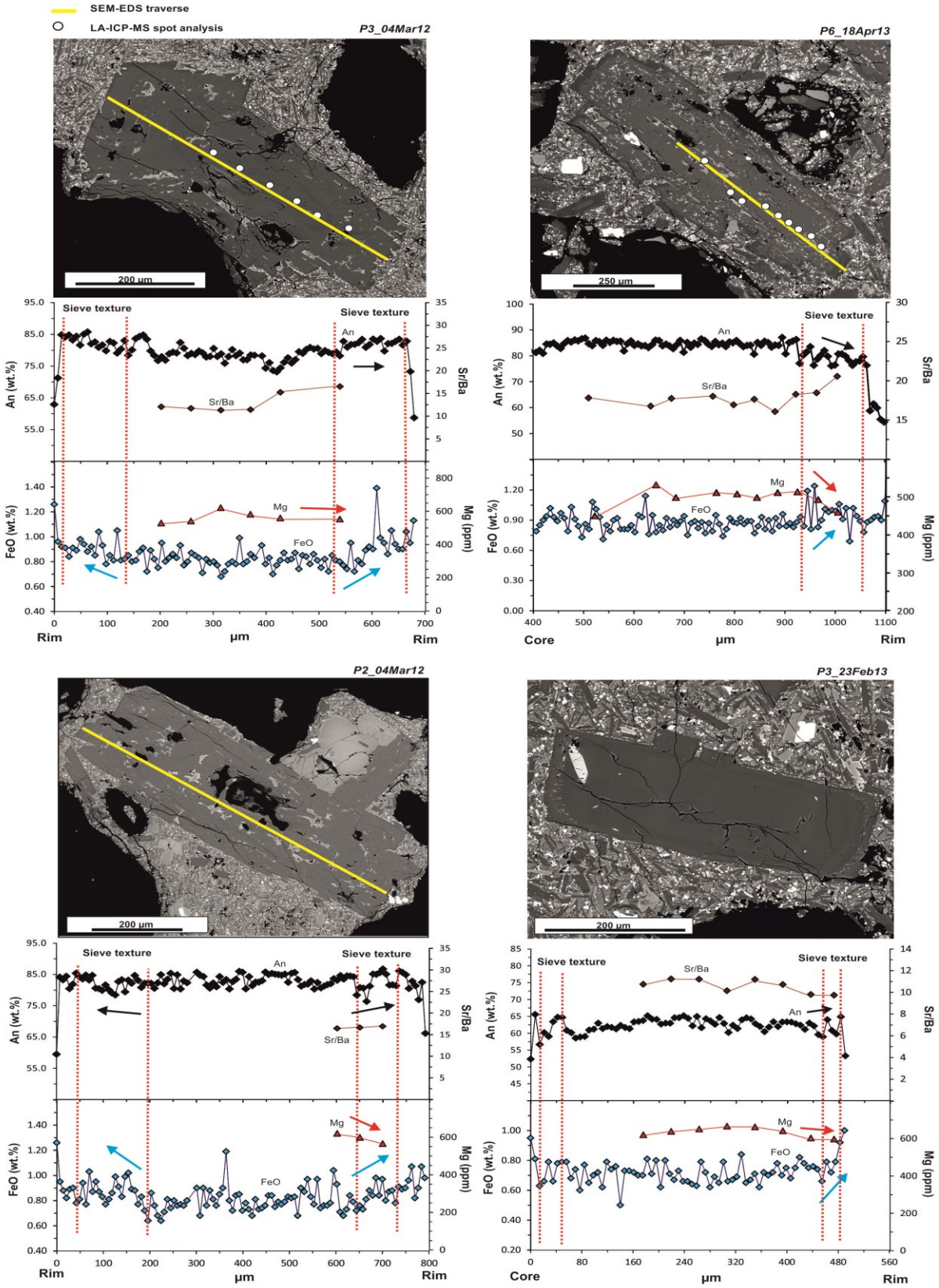

Figure 21. *Plagioclase crystals affected by disequilibrium textures at the rim and their associated An (mol%), FeO (wt.%), Mg (ppm) and Sr/Ba zoning patterns. Diagrams show the type of sieve textures (areas within dotted lines) characterized by iron increases that are not coupled to concomitant increases of An and/or Mg contents. Simbols as in figure 20.*

3.5.3 Lithium compositional gradients in plagioclase

Plagioclase crystals investigated by SIMS for lithium concentrations were taken from lavas of six different eruptions characterizing the 2012 and 2013 activity at Mt. Etna. All the crystals analyzed by SIMS are exclusively oscillatory zoning with sizes between ~500 and 950 μm. Li compositional variations are reported as variations of the $^{7}Li/^{30}Si$ ion ratios along 200-300 μm-long transects that follow the apparent c-axis orientation of plagioclase (see section 3.2 for the description of analytical procedures). $^{7}Li/^{30}Si$ values range from 2.7×10^{-3} to 0.4×10^{-4}, corresponding to absolute Li concentrations between 6.8 ppm and 0.1 ppm (Table 3). Examinations of the SIMS profiles reveal overall decreasing trends of the $^{7}Li/^{30}Si$ ratio toward the edge of all selected crystals (Fig. 22). These variations, which have been plotted in diagrams of Figure 22 together with the An concentrations, are apparently independent from the major element composition of plagioclase. It has been also noted short intervals within the Li profiles where the $^{7}Li/^{30}Si$ trend changes slope and begins to increase (Fig. 22). Main peaks of increasing $^{7}Li/^{30}Si$ have been observed at distance of ~230 μm from the plagioclase edge (i.e.,crystals P1_24Apr12 and P2_5Mar13), at ~160 μm (i.e. P6_23Feb13 and P7_12Apr13) and, in almost all analyzed crystals, at distance between 110 and 120 μm (i.e., P1_24Apr12, P6_23Feb13, P4_5Mar13, P7_12Apr13, and P7_18Apr13), as well as in the final 40-50 μm of plagioclase growth (i.e., P1_24Apr12, P3_24Apr12, P6_23Feb13, and P4_5Mar13; Fig. 22).

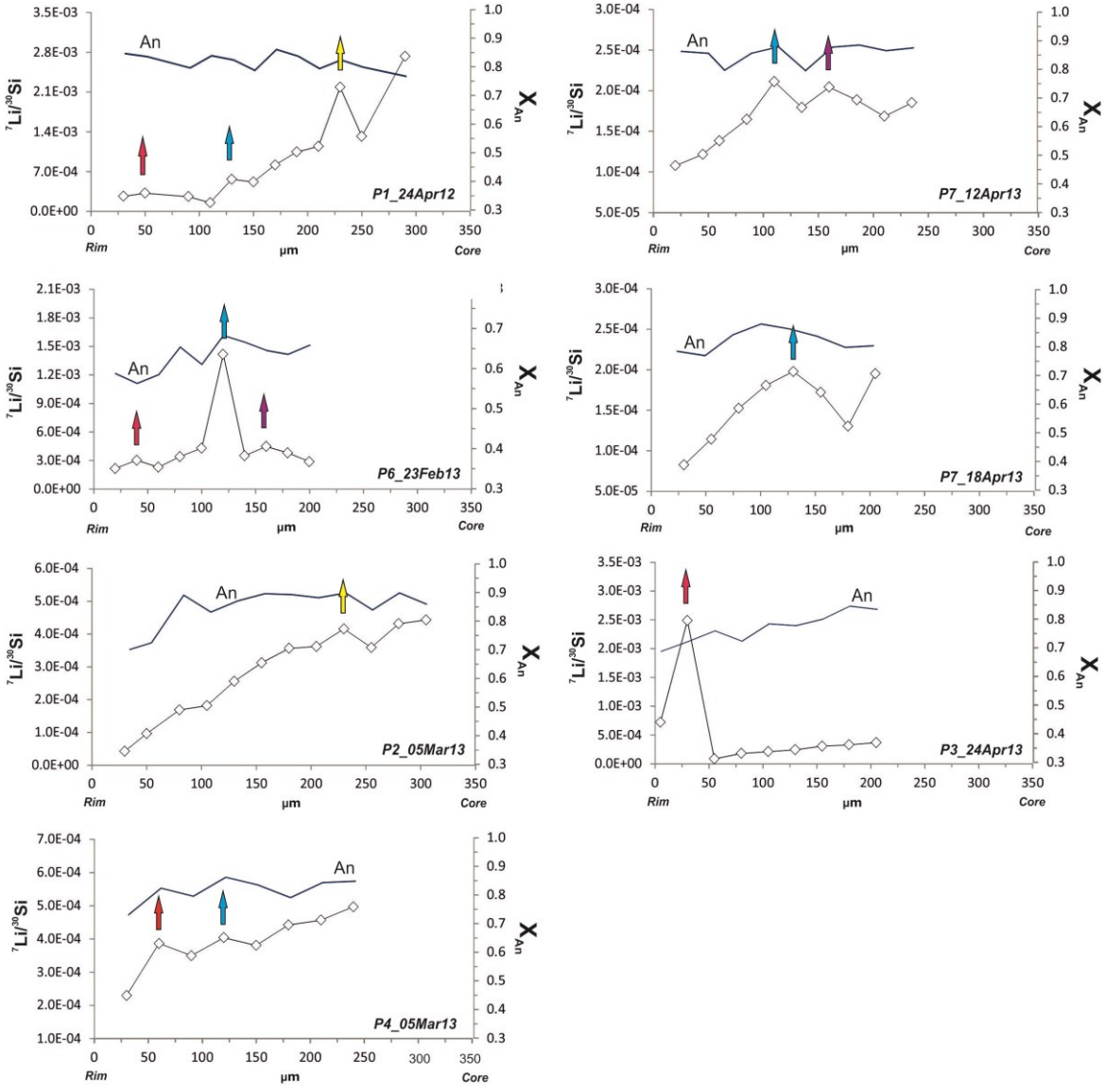

Figura 22. *$^{7}Li/^{30}Si$ concentration profiles and An composition for plagioclase crystals from lavas of the 2012-2013 Mt. Etna activity. Arrows of different colors indicate the lithium concentration peaks that were detected at precise distance from the plagioclase edge.*

Table 3. Ion microprobe determination of lithiumconcentrations (ppm) for selected plagioclase crystals from lavas of the 2011-2013 activity.

P1_24Apr12		*P3_24Apr12*		*P6_23Feb13*		*Pl2_5/6Mar13*		*Pl4_5/6Mar13*		*P7_12Apr13*		*P7_18Apr13*	
µm*	Li (ppm)	µm*	Li (ppm)	µm*	Li (ppm)	µm*	Li (ppm)	µm*	Li (ppm)	µm*	Li (ppm)	µm*	Li (ppm)
30	0.65	5	1.81	20	0.59	30	0.10	30	0.56	20	0.27	30	0.21
50	0.79	30	6.34	40	0.56	50	0.24	60	0.95	45	0.30	55	0.29
90	0.64	55	0.21	60	0.58	80	0.39	90	0.86	60	0.34	80	0.37
110	0.38	80	0.44	80	0.65	105	0.44	120	0.97	85	0.40	105	0.44
130	1.39	105	0.52	100	0.61	130	0.60	150	0.93	110	0.51	130	0.49
150	1.27	130	0.59	120	0.68	155	0.75	180	1.06	135	0.44	155	0.43
170	1.98	155	0.75	140	0.67	180	0.85	210	1.12	160	0.50	180	0.33
190	2.57	180	0.80	160	0.65	205	0.84	240	1.21	185	0.46	205	0.49
210	2.83	205	0.90	180	0.64	230	1.00			210	0.41		
230	5.36			200	0.66	255	0.88			235	0.45		
250	3.24					280	1.00						
290	6.79					305	1.08						

*Distance measured from the edge of plagioclase crystal

3.5.4 Olivine chemical zoning patterns

47 Olivine crystals related to the eruption sequences between January 2011 and April 2013 have been analyzed for major elements along traverses crosscutting the center of the crystal, with step of 7-13 µm between each analyzed spot. Within the same sample, olivine crystals often display different compositional zoning. The zoning patterns are either normal (decreasing Fo values toward the rims) or reverse (increasing Fo values toward the rim) in crystals displaying cores of comparable composition. It is also worth noting the occurrence of more complex zoning patterns, such as multiple reverse and normal zoning at the crystal rim.

Five main olivine populations (OP) have been identified on the basis on their core compositions, namely: 1) the first population (OP1) refers to olivine with Fo_{84} cores (Fig. 23a-b); 2) the second population (OP2) pertains to olivine with Fo_{80-82} cores (Fig. 23c-d); 3) the third population (OP3) is constituted by olivine cores at ~Fo_{78} (Fig. 23e-f); 4) the fourth population (OP4) is composed of crystals with core composition at Fo_{75-76} (Figs. 23g-h); 5) the fifth population (OP5) embraces the most evolved individuals, having cores at Fo_{70-73} (Figs.23i-l).

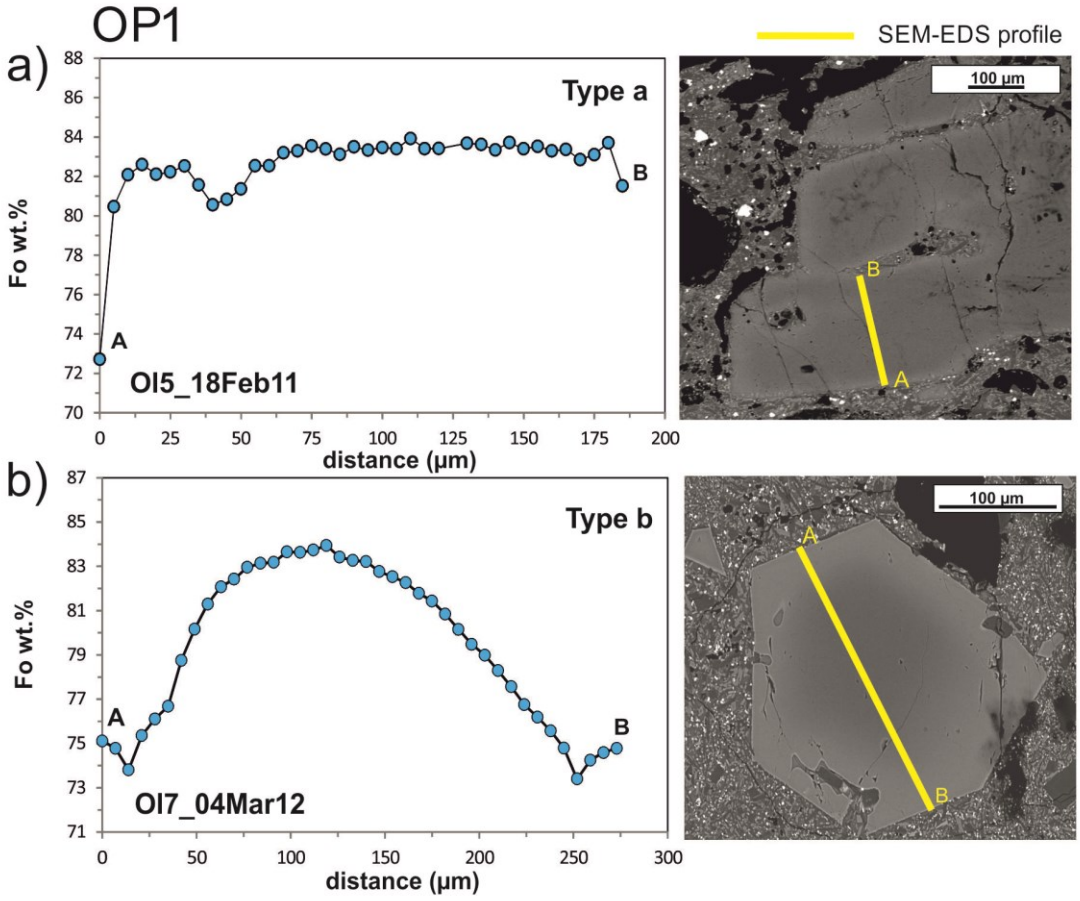

Figure 23a-b. *Illustration of the zoning patterns that characterize olivines OP1 with Fo_{84} core composition: a) normal zoning; b) normal zoning pattern followed by revers zoning toward the crystal edge. BSE image display the direction of the compositional traverse*

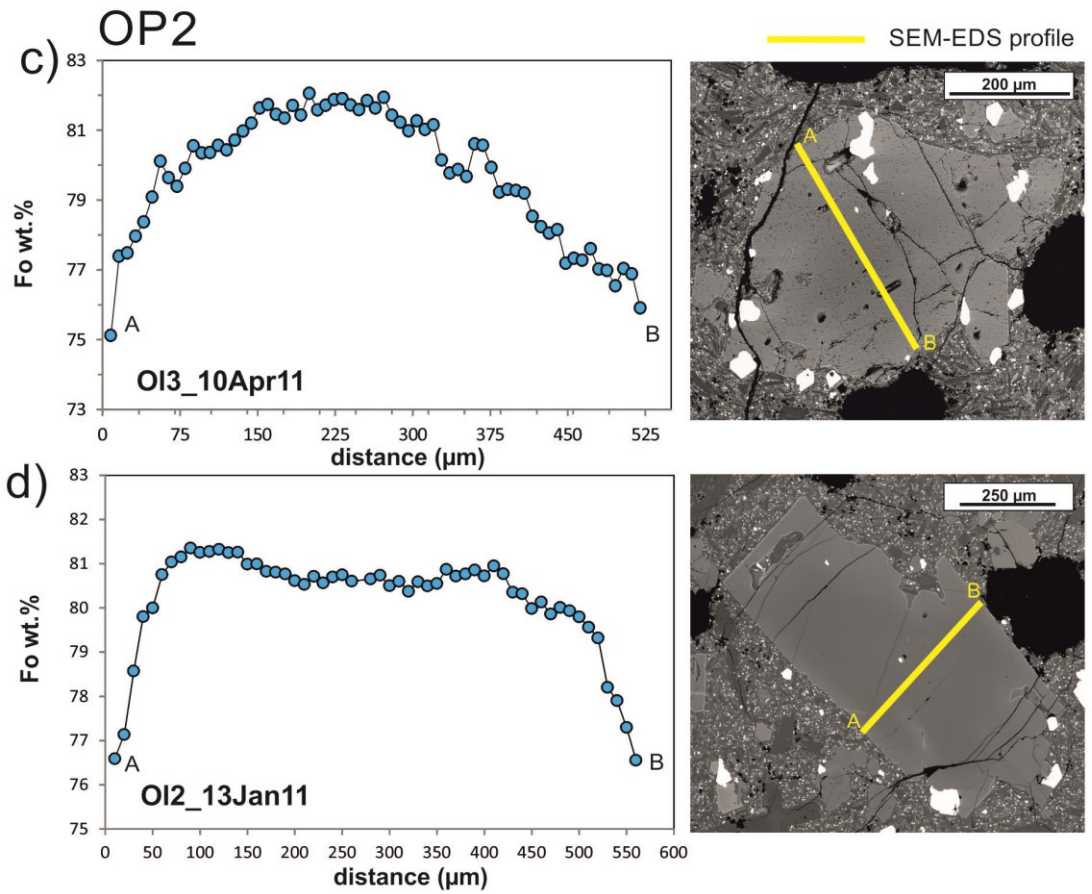

Figure 23c-d. *Illustration of the zoning patterns that characterize olivines OP2 with* $Fo_{80\text{-}82}$ *core composition: c) normal zoning; d) reverse zoning changing to normal zoning toward the rims. BSE image display the direction of the compositional traverse.*

The OP1 olivines (~Fo_{84}) are rather uncommon; a total of 4 individuals were found in samples collected from two distinct eruptions, namely the paroxysms of February 18, 2011 and March 4, 2012. These olivines are small and medium size phenocrysts (250-500 µm) having euhedral habitus, with the exception of one single individual which is resorbed and characterized by extensive embayments (Fig. 23a). Cores display nearly flat compositional profiles and are mantled either by normally zoned rims (OP1_Type a; Fig. 23a) or by regions with normal zoning pattern followed by

reverse zoning at the outermost 10-20 µm-wide rim (OP1_Type b; Fig. 23b). In the normal zoning patterns, the Fo concentration decreases to ~Fo_{72} and ~Fo_{80}. (Fig. 23a-b).

Olivines belonging to OP2 include large euhedral and embayed crystals, with size ranging from 700 to 1400 µm (Fig. 23c-d.). These olivines generally show rather constant ~Fo_{80-82} core composition and normally-zoned rims; a few crystals also display reverse zoning with slightly increasing Fo toward the rim (up to ~Fo_{82}). In the outermost envelopes (last 30-50 µm), all the OP2 crystals record normal zoning with decreasing Fo content to ~Fo_{76}.

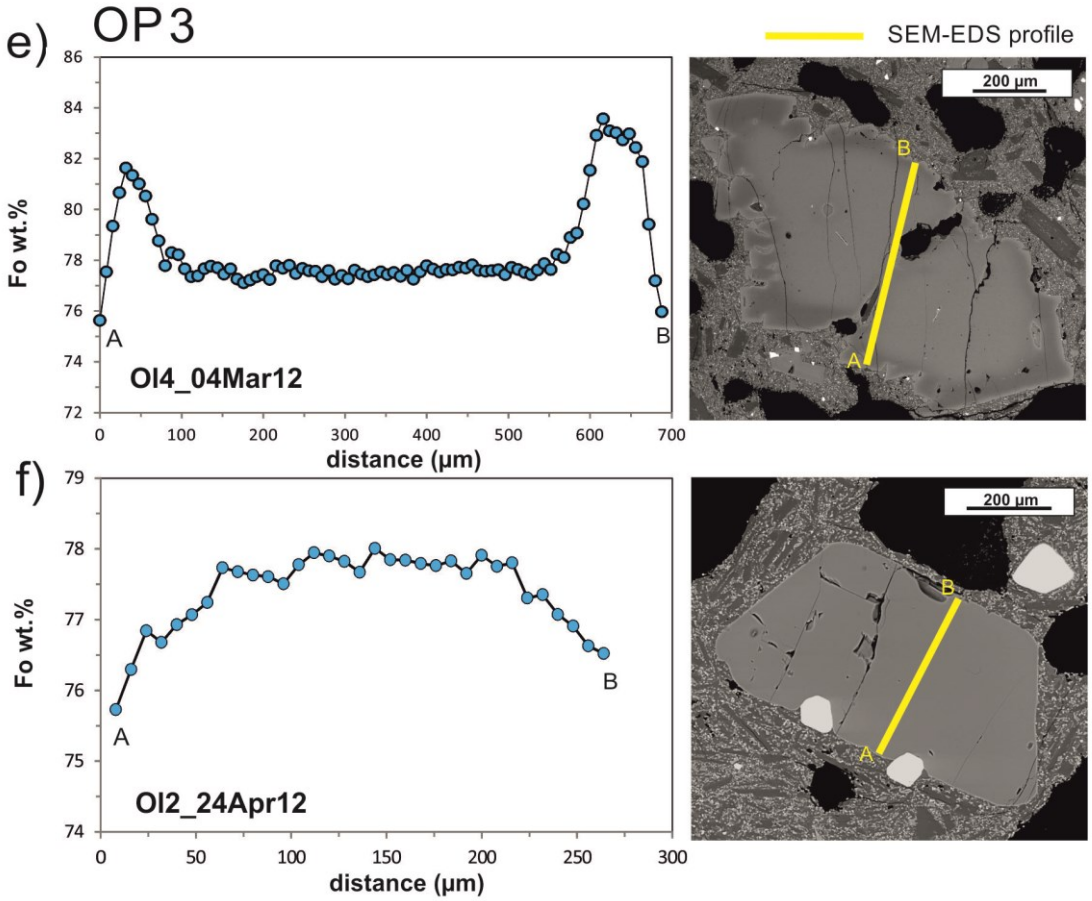

Figure 23e-f. *Illustration of the zoning patterns that characterize olivines OP3 with Fo_{78} core composition: e) olivine with rather homogeneous core composition followed by reverse zoning that finally change to normal zoning at the rim; f) olivine with normally-zoned rims. BSE images display the direction of the compositional traverse.*

OP3 olivines constitute the least abundant population, being ~8 % of the total analyzed olivine phenocrysts (Fig. 23e-f.) OP3 crystals are generally large, with sizes between 800 and 1300 µm, and are resorbed to a variable extent. The typical zoning pattern is constituted by a nearly flat core profile at ~Fo_{78} followed by reverse zoning toward the rims (Fig. 23e). The reversely zoned portion of the crystal displays consistent changes in the Fo concentration (~ΔFo_6) that produce high forsteritic envelopes at ~Fo_{84}. The outermost rims are normally zoned with decreasing Fo content to ~Fo_{76}. We observed also olivine OP3 having exclusively normal zoning patterns (Fig. 23f).

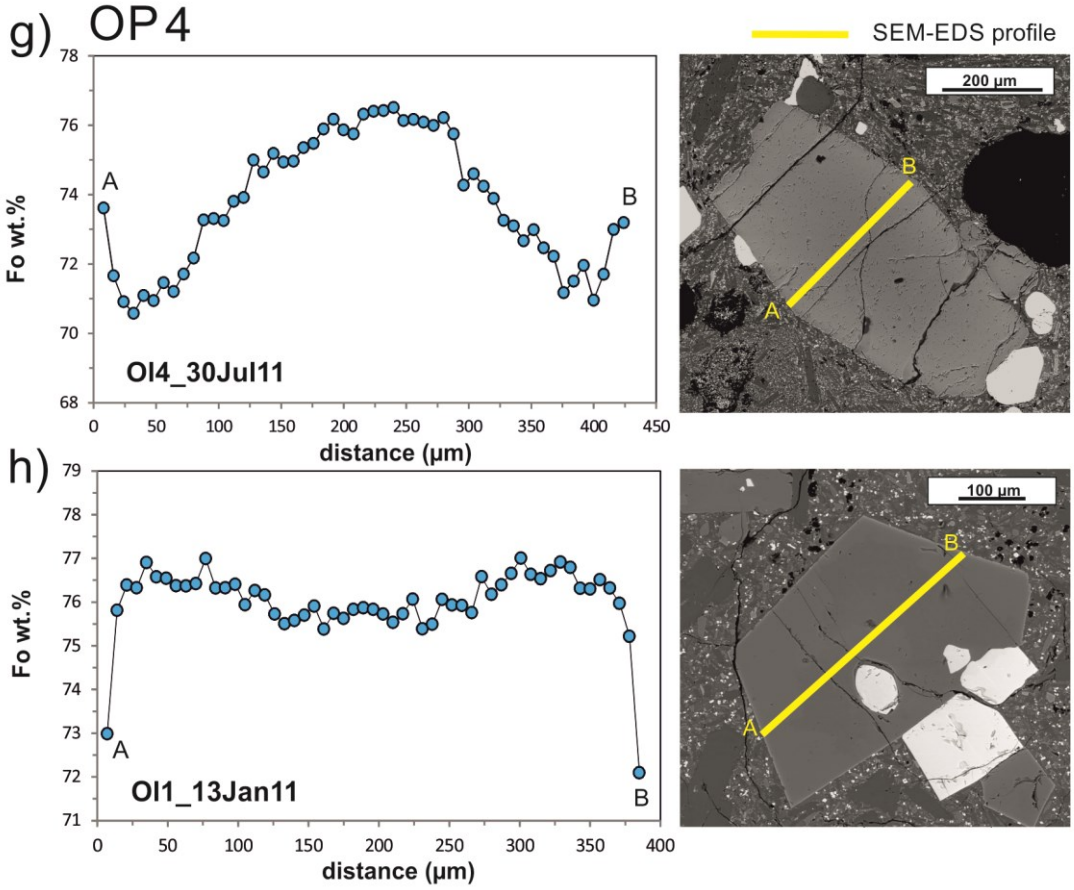

Figure 23g-h. *Illustration of the zoning patterns that characterize olivines OP4 with Fo_{75-76} core composition: g) complex zoning pattern formed by normal zoning around the core and reverse zoning at the outermost rim; h) olivine crystal with the core surrounded by a reverse-zoned region and normally-zoned rims. BSE image display the direction of the compositional traverse.*

Crystals in population OP4 exclusively occur in lava rocks from January 2011 to April 2012 eruptions, forming ~16 % of total analyzed olivines. These olivines show rather constant ~Fo_{75-76} core compositions (Fig. 23g-h). Two distinct zoning patterns have been distinguished at the crystal rims: the dominant zoning at the rim of OP4 crystals is normal zoning with decreasing Fo to ~72 mol%, that finally changes to reverse in the outermost rim (Fig. 23g); less common is the occurrence of reverse-zoned regions with very limited variations in Fo contents (~ΔFo_1), shifting to lower Fo values at the crystal edge (Fig. 23h). OP4 crystals are commonly euhedral with size between 300 μm and 1 mm. The largest crystals often are affected by embayments.

OP5 crystals (core composition ~Fo_{71-73}) are the most abundant in the samples under investigation (~60 % of the investigated olivine phenocrysts) and mainly occur in products from the 2012 and 2013 eruptive period (Fig. 23i-l). These crystals are euhedral with sizes ranging from ~250 to ~600 μm. The observed compositional zoning patterns are typified by flat compositional profiles in the crystal interior that shifts to higher Fo content towards the rim (Fig. 23i). These reverse zoning patterns show variable ΔFo: commonly the Fo content increases up to ~Fo_{74-76} (ΔFo_{1-4}), however olivine crystals from the March 4, 2012 show more significant variation up to Fo_{77-80} (ΔFo_{5-9}). Less common zoning patterns, often related to one single crystal, have been also recognized (Fig. 23l). From core to rim, these rare zoning patterns could be described as follows: a) rather constant composition + normal zoning (Fo decreases to ~Fo_{71}); b) rather constant composition + normal zoning (Fo decreases to ~Fo_{71}) + reverse zoning (Fo increase to ~Fo_{74-76}); c) rather constant composition + reverse zoning (with $\Delta Fo_{0.5-1}$) + normal zoning (Fo decreases to ~Fo_{71}).

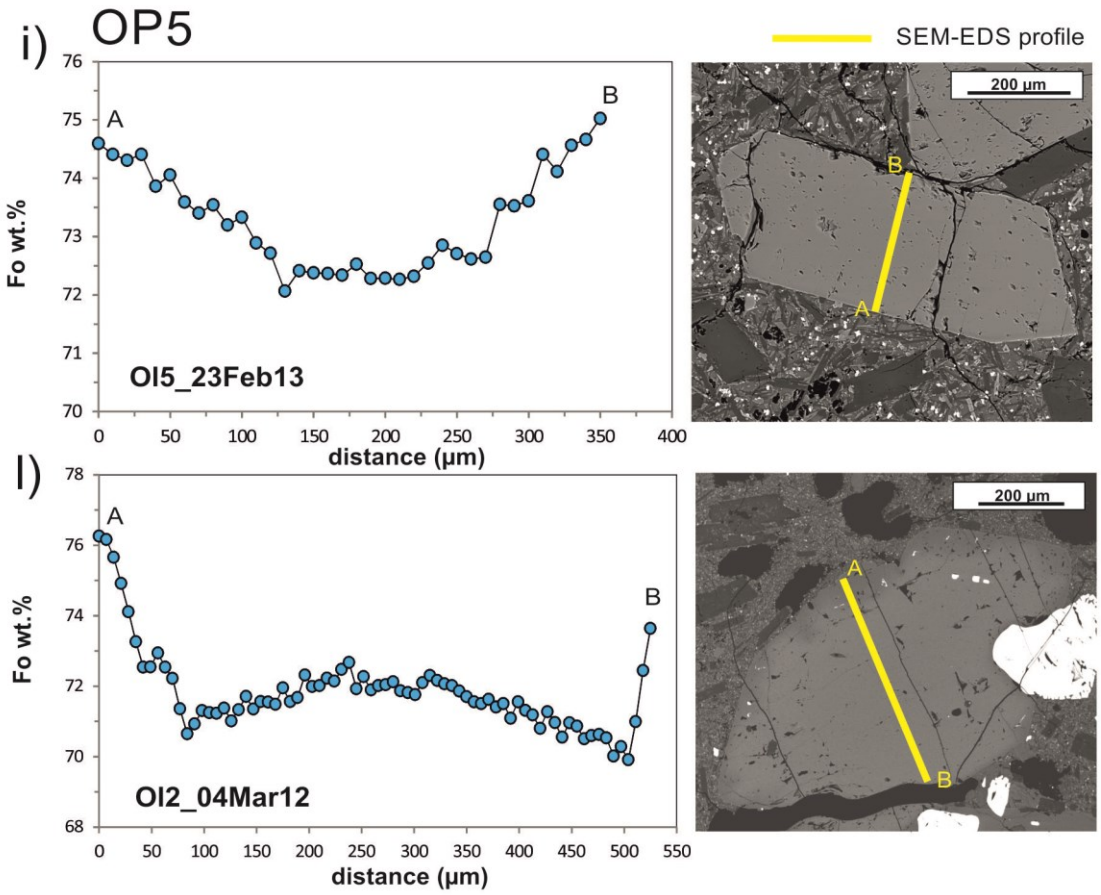

Figure 23h-i. *Illustration of the zoning patterns that characterize olivines OP5 with* $Fo_{70\text{-}72}$ *core composition: i) typical zoning pattern of OP2 crystal with a rather flat core profile and reverse-zoned rims; l) exemple of crystal characterized by a complex zoning pattern given by the combination of normal and reverse zoning. BSE image display the direction of the compositional traverse.*

3.6 Discussion

3.6.1 Evidence of magma evolution during the 2011-13 activity of Mt. Etna

Volcanic rocks formed during the 2011-2013 at the NSEC preserve chemical characteristics comparable to those of products emitted after the 1971 AD, in particular, for their progressive K enrichment, concentrations of some LILEs, such Rb and Cs, and for their Sr isotope compositions. In particular, whole rock data indicate a major compositional resemblance between lavas from the recent 2011-2013 episodes and lavas erupted at Mt. Etna after the 2001 eruption, which represent the most recent turning point concerning the geochemistry of emitted products and the eruptive behavior of Mt. Etna. These observations, already emphasized by Viccaro et al. (2015) and Viccaro et al. (2016b), are indeed consistent with the statement of many authors that since the 2001 AD the storage and transport system of Mt. Etna has been fed by a new volatile-rich magma, distinct in its geochemical signature from magmas previously emitted at the volcano (i.e., Metrich et al., 2004; Spilliaert et al., 2006a; Ferlito et al., 2012). Specifically, to better evaluate the compositional variability of products erupted at the NSEC during the 2011-2013 paroxysms in the framework of the post-2001 activity, major element compositions of the 2011-2013 lavas have been plotted in Figure 24 together with the compositions of products erupted since 2001. The comparison among these data suggests that magmas feeding the 2011-2013 activity inherited a signature very close to that of magmas that fed the 2007 paroxysmal episodes at the South East Crater (SEC) and the long-lasting 2008-2009 eruption, and they follow the trend of a common liquid line of descend (Figure 24). Products related to the early eruptions of 2012 (March and April) have a prominent

similarity with compositions of the volcanic rocks erupted during 2007 (see whole rock compositions available for the 2011 and 2013 eruptions at http://www.volcanology-unict.it/online_material/giuffrida_phd_thesis; cf. Viccaro et al., 2015), and they both exhibit the most basic compositions erupted at Mt. Etna since 2001. This could indicate a common magmatic source for the 2011-13 and 2007 lavas. The injection in the Etnean plumbing system of a magma with distinct geochemical/isotopic signature with respect to previously erupted has been detected since the end of October 2006 by Nicotra and Viccaro (2012a), integrating petrological data with the CO_2/SO_2 molar ratios measured in the gas plume during the 2006 eruptive episodes at Mt. Etna (data from Aiuppa et al., 2007). The minor differences that have been noted between 2007 and the 2011-2013 products could be chiefly referred to the evolutionary degree of magmas acquired through differentiation (Fig. 24; cf. Viccaro et al., 2015).

Mineral chemistry of the lavas under investigations put into evidence, however, some variations within the considered period of activity. The overall fluctuations through time of the anorthite content in plagioclase, Mg# in clinopyroxene and forsterite in olivine within the framework of the 2011-13 paroxysmal activity well accounted for changes of the physical and chemical equilibrium of the magmatic system (Fig. 9). In a number of well-studied magmatic systems, concomitant increase of these mineral parameters has been generally attributed to processes of replenishment by more basic magmas and mixing with the resident one (e.g. Streck et al., 2008 and references therein). For example, a similar approach of investigation based on variations of the Fo composition at the core and rim of olivine crystals from Mt. Etna has led Kahl et al. (2013) to detect major recharging events feeding the 2006 eruptive episodes. On the same line of evidence

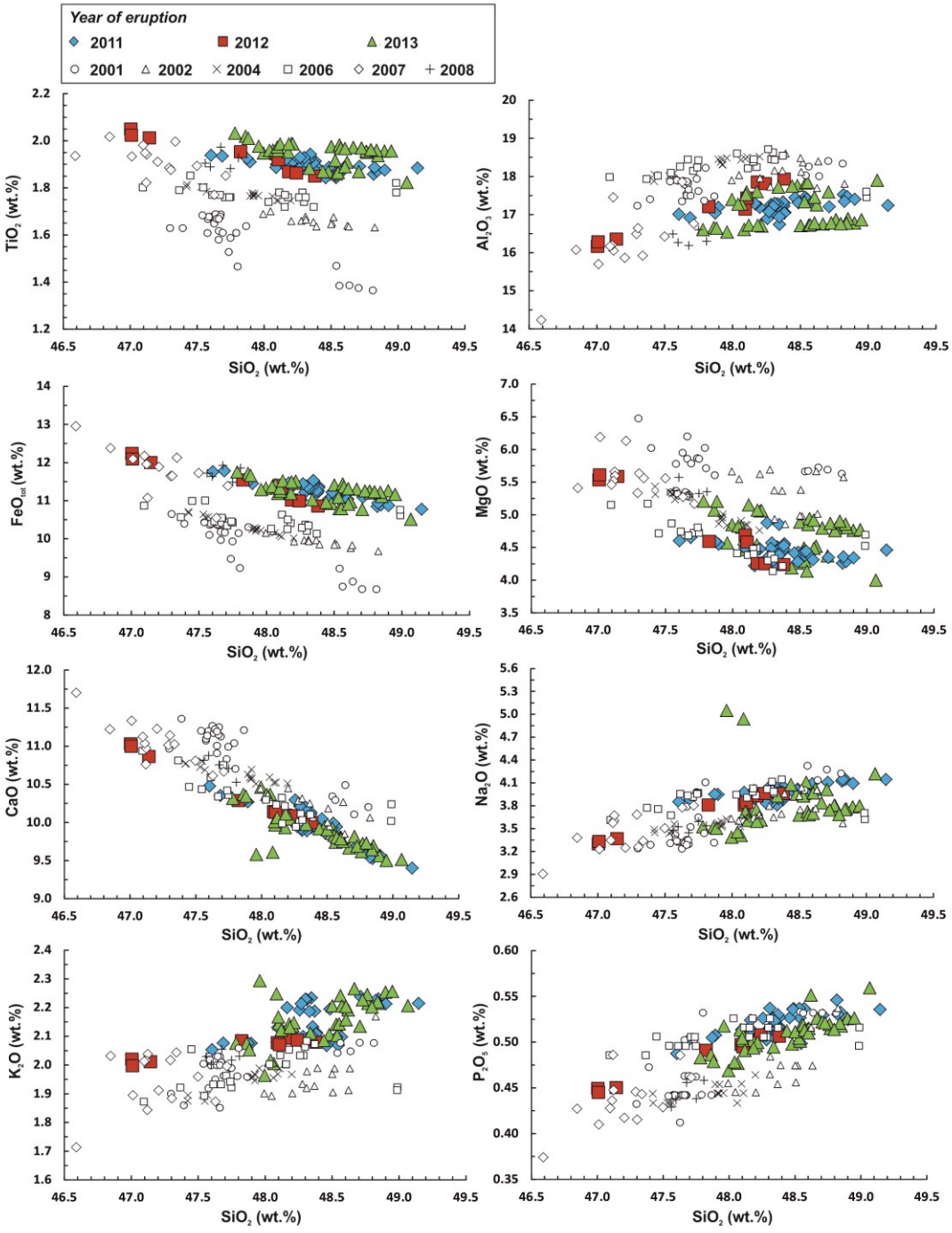

Figure 24. *Variations of major oxides for volcanic products erupted during the 2011-2013 period plotted together with compositions of lavas of the post-2001 volcanic activity of Mt. Etna.*

fluctuations of the evolutionary degree of the whole rock data (Figs.6-7) provide clear indications that mixing due to mafic recharge has a primary control on the composition of the 2011-2013 volcanic products. On the whole, the evolution through time of the key compositional parameters of the mineral phases, such as An%, Mg#, Fo% (Fig. 9) together with the variability of the bulk rock chemistry (Figs. 6-7), highlights repeated mafic events of replenishment in the Etnean feeding system during the period under investigation. Moreover, these compositional fluctuations toward more mafic terms cover relatively short period of time (weeks-months) throughout the 2011-2013 period, suggesting that processes of magma recharge feeding the paroxysmal activity at the NSEC have had an overall pulsating character. These recharge events may have caused pressurization in the shallow portions of the plumbing system, therefore acting as a trigger mechanism of the paroxysmal activity at the surface.

3.6.2 The importance of investigating mineral textures and zoning

Episodes of replenishment by more basic magma are common phenomena at Mt Etna, and have been often evidenced by the occurrence of geochemical mixing trends (e.g., Viccaro et al., 2006; Viccaro and Cristofolini, 2008). However, during complex pre-eruptive histories characterized by multiple mixing events and, moreover, after homogenization of the magmas, most information is lost from the whole rock geochemistry about the composition of recharging magmas, as well as about the concomitant occurrence of multiple differentiation processes (i.e., crystal fractionation and assimilation). It is, therefore, crucial to understand the nature of these processes and how they affect the evolution of a magmatic system during storage, ascent and eruption.

One approach to investigate magma dynamics is the study of the crystallization histories of minerals in volcanic rocks, using major, minor, and trace element zoning.

Plagioclase is the most suitable mineral for such a study because its major element zoning may faithfully record the compositional and physical changes of magmas at variable temporal and spatial scales, without significant subsequent re-equilibration. This is because the inter-diffusion of the CaAl and NaSi components is extremely slow, so that the anorthite zoning is preserved through time (Grove et al., 1984; Morse, 1984), whereas the diffusivity of some minor (e.g., Mg) and trace elements (e.g., Sr and Li) is considerably faster (Giletti and Casserly, 1994; Giletti and Shanahan, 1997). However, factors controlling plagioclase An composition are rather complex and difficult to separate (they have been discussed in the next section). The combined analysis of major, minor and trace element zoning has been demonstrated to provide a rather accurate record of the open system processes that magmas undergo during plagioclase growth history (e.g. Singer et al., 1995; Kuritani, 1998; Ginibre et al., 2002a and 2002b; Ginibre and Worner, 2007; Viccaro et al., 2010; Viccaro et al., 2012). This approach, if also associated with the observation of the textural characteristics of crystal, which are evidence of growth/resorption processes, is particularly appropriate to reconstruct a comprehensive working model of the plumbing system and modes of eruption of volcanoes.

Olivine crystals may also respond quickly to non-equilibrium conditions by dissolution/resorption (e.g., Donaldson, 1990) and diffusional re-equilibration (e.g., Costa et al., 2008) but, as in the case of other ferromagnesian minerals, the Fe-Mg zoning primarily reflect changes in composition of the melt (Streck, 2008). A careful analysis of the textural and compositional relationships of olivine crystals may yield evidence for

open-system processes of magma mixing, more clearly than plagioclase (e.g. Landi et al., 2007; Kahl et al., 2011, 2013, 2015; Viccaro et al., 2016a). However, in some cases, it is important to consider the correlation between Fe-Mg zoning and minor element concentrations (i.e. Ni) because they are important to exclude the influence of other factors such as changes in fO_2 (Streck, 2008).

In the following sections, factors controlling texture and zoning patterns of Etnean plagioclase and olivine crystals and, then, their significance in the framework of the 2011-2013 paroxysmal activity are discussed.

3.6.3 Processes controlling major, minor and trace element zoning in plagioclase

As previously mentioned, some limitations in interpreting plagioclase zoning patterns derive from the fact that the major element composition is controlled by several factors, such as temperature, pressure, melt composition and water content. Therefore, prior to discussing the zoning patterns observed in the Etnean plagioclases, some main issues need to be considered. Melt composition, temperature and water concentrations exert the dominant influence on the anorthite content of plagioclase. Specifically, the An composition decreases with increasing differentiation of the melt and decreasing temperature, if other parameters are constant. Extraction of water from the melt during decompression and degassing also results in increasing plagioclase stability, yielding to crystals with more sodic compositions (Blundy and Cashman, 2005). The effects of pressure on plagioclase composition are rather negligible compared to other variables involved, because pressure becomes significant only upon variations of several kilobars

(Hush and Luhr, 1991). However, in volatile-rich magmas, pressure strongly controls water solubility, and thus indirectly affects the composition of plagioclase. Indeed, if the melt is water-undersaturated, a pressure decrease will cause plagioclase dissolution and more calcic compositions (Nelson and Montana, 1992; Blundy and Cashman, 2001), whereas magma decompression under water-saturated conditions will induce degassing and crystallization of more sodic plagioclase (Blundy and Cashman, 2005). Based on all these considerations, it is evident that complex histories of crystallization, i.e. throughout a multi-storage magmatic system, would be extremely difficult to assess if taking into account only the plagioclase anorthite composition.

Variations of some minor and trace element may serve as evidence of changing melt composition (e.g. Fe, Mg, Sr) or may reflect changes in the plagioclase mineral-melt partition coefficients (e.g. Sr, Ba). Thus, minor and trace elements allow better identification of the causes of plagioclase zoning patterns, though the low spatial resolution of trace elements analytical techniques (i.e. LA-ICP-MS) does not permit the investigation of zoning at small scale.

Among the plagioclase minor elements, Fe and Mg are powerful indicators of changes in melt compositions. This is because their concentration in the melt is primarily related to the degree of melt differentiation, and indeed they correlate negatively with bulk SiO_2 as the evolution of the melt proceeds (Ginibre and Worner, 2007). Thus, if both Fe and Mg show similar compositional trends within plagioclase, this is evidence that such variations are indeed caused by changing composition of the melt (e.g., after episodes of recharge with a magma of different composition). However, Fe concentrations may be also controlled by other factors than melt composition. This means

that plagioclase crystals may record increasing Fe concentration without a concurrent increase in Mg if the melt composition remains unvaried. In this regard, Wilke and Behrens (1999) and, later, Sugawara (2001) demonstrated that Fe partitioning strongly depends on oxygen fugacity, which does not affect Mg. Following these authors, D_{Fe} and fO_2 are positively correlated, in a way that the higher is fO_2, the higher is the iron concentration in the plagioclase. Experimental determinations of Bindeman et al. (1998) and Sugawara (2001) also showed that the Fe partition coefficient is negatively correlated with temperature and An, whereas plagioclase-melt partitioning for Mg very weakly depends on these parameters (Sato 1989; Bindeman et al., 1998). While the influence of water on Fe and Mg partition coefficients is not known, changes in water concentration are likely to affect oxygen fugacity of the system (Ruprecht and Worner, 2007) and, therefore, may also induce significant effects on Fe compared to Mg.

The concentrations of Sr and Ba are relatively high in plagioclase, because they substitute for Ca; moreover their partitioning strongly depends on the structure of the plagioclase crystal (Blundy and Wood, 1991; Gilletti and Casserly, 1994). The Ba and Sr cations are accommodated by lattice strain in the host plagioclase lattice, but because the elasticity of the albite lattice is greater relative to anorthite, Sr and Ba are more easily accommodated in sodic plagioclase. In this regard, Blundy and Wood (1991) found a negative relationship between D_{Sr} and D_{Ba} and the An mole fraction (XAn), indicating that both elements are more compatible in albite than anorthite, therefore, demonstrating that crystal chemistry has dominant influence on partitioning of Sr and Ba into plagioclase. However, the larger Ba cation is less compatible than Sr as An content increases. Temperature, pressure, and fluid composition may also exert an influence on

the crystal structure (Blundy and Wood, 1991), but their overall effects on trace element partitioning between plagioclase and silicate melts are negligible compared to the crystal chemical control.

3.6.4 *Crystallization conditions and magma dynamics inferred from chemical zoning and textures of plagioclase*

Oscillatory zones and significant An jumps often associated with textural changes, are expressions of very different responses of plagioclase crystals to changing thermodynamic equilibria of their host melt. Oscillatory zoning is a feature that plagioclase crystals may acquire during growth under near-equilibrium condition (Anderson, 1984). Crystallization of an oscillatory-zoned pattern requires, therefore, nearly constant magmatic temperature, pressure, and water content. On the contrary, prominent An variations may form in response of important P-T-H_2O changes in the host melt, testifying plagioclase crystallization under disequilibrium conditions.

Plagioclase crystals from the recent paroxysmal activity at Mt. Etna exhibited both small-scale (<5 μm) and large-scale (10-15 μm) compositional oscillations. The origin of such types of zoning in plagioclase has been the focus of much scientific debate for a long time. Following a number of authors (Allegre, 1981; L'Heureux and Fowler, 1994, 1996; Pearce, 1994; Ginibre et al., 2002a, b; Tsune and Toramaru, 2007), small-scale An oscillations are kinetically controlled, while large-scale zonings with An variation on the order of 10 mol% likely reflect crystal growth in a magmatic environment, characterized by small but more prominent chemical and/or physical changes. In the 2011-2013 Etnean plagioclase crystals, small-scale oscillatory zoning patterns have been generally found at

the cores of large phenocrysts (1-2 mm in diameter). This observation is consistent with an early phase of plagioclase growth in a magmatic system that is at or near equilibrium and, therefore, not affected by important chemical or physical changes. The existing kinetic models invoke localized compositional variations in the melt at the crystal-melt interface as the main cause for the development of small An fluctuations during the plagioclase growth. These models, however, fail to explain the occurrence of resorption surfaces cross-cutting portions of plagioclase that grow in equilibrium. For this reason, the development of slightly major compositional oscillations (10-15 μm amplitude) observed at the rim of large crystals and in micro-phenocrysts of the 2011-2013 Etnean products appear more consistent with small-scale convective movements of crystals in a magma storage zone. Crystal convection along small thermal and compositional gradients well accounts for the development of minor wavy dissolution surfaces that cross-cut the observed oscillatory zones (Pearce and Kolisnik, 1990; Singer et al 1995). Following Couch et al. (2001), heating of the resident magma by recharge may also cause variations in the melt temperature able to generate compositional gradients in oscillatory-zoned plagioclase on the order of 10 mol% An or higher. However, it has been noted that the anorthite trends are only weakly or not correlated to Fe and Mg variations within the crystals. This would indicate that the origin of large-scale oscillatory-zoned crystals is likely related to minor changes in temperature and/or dissolved H_2O of the system, hence suggesting the presence of differently degassed domains in the magma reservoir. In any case, the presence of large-scale oscillatory zoning dominantly at the rim of plagioclase phenocrysts denotes dynamic conditions of the magmatic system during the late-stage of plagioclase growth at shallow depth. These features have been previously attributed to

plagioclase crystallization within the open, steady degassed conduit of Mt. Etna (Viccaro et al., 2010; Nicotra and Viccaro, 2012a, 2012b). Investigating the volcanic activity of 2011-2012, Viccaro et al. (2014) proposed that large-scale An oscillations at the rim of plagioclase crystals may form during magma residence in a shallow storage zone that was detected at ~1-2 km beneath the New South East Crater on the basis of recent geophysical investigations (Patanè et al., 2013; Viccaro et al., 2016a). Here, crystals recording different early histories of crystallization within the storage and transport system of Mt. Etna certainly merged before eruption. This inference is based on the observation that each single lava sample contains crystals having different size, textures and compositions. In this regard, the average anorthite compositions of co-existing wholly oscillatory-zoned crystals span over a wide range, from about An 55 to 85 mol%. Moreover, Etnean K-trachybasalts have narrow range of temperatures at the vent, close to 1080°C (Tanguy and Clocchiatti, 1984), which indicate rather constant temperature at intratelluric conditions. This means that the observed compositional diversity of plagioclase may be justifiable only assuming crystallization at different depths from magmas with different degrees of differentiation and/or with variable volatile content that finally merge at shallow depth prior to eruption.

Another consideration that needs to be taken into account is that most of the oscillatory-zoned crystals having similar anorthite composition display a significant difference in the average Sr/Ba ratios (Fig. 17). In particular, plagioclases from the 2011 period of activity record Sr/Ba values significantly lower (in average ~8) compared to those from the 2012 and 2013 products (average Sr/Ba values ~ 23). In both cases, the Sr/Ba variations exhibit a good correlation with the An composition, following similar

decreasing or increasing trends along the plagioclase compositional profiles (Figs.13-16). This implies that the trace element behavior in the Etnean plagioclases is mainly controlled by crystal/melt partitioning, probably associated with processes of crystal fractionation. Indeed, Sr and Ba are compatible in plagioclase, and therefore their concentrations in the melt decrease during crystallization and differentiation, but partition coefficients of both elements decrease with increasing An content. Blundy and Wood (1991) also found that Ba is less compatible than Sr in plagioclase as the An content increases; thus, the higher the An content, the higher the Sr/Ba ratio in the plagioclase. Therefore, the observed correlation between An and Sr/Ba at the core of oscillatory zoning crystals is consistent with variations in the partition coefficients, more than variations in the melt composition. Crystal/melt partitioning from a melt with a similar geochemical signature, however, fails to explain the presence of two suites of plagioclase crystals with low (~ 8) and high (~23) Sr/Ba ratio at similar An content, features that can be only justified by assuming variations in the geochemical characteristic of the host melt. This means that the two suites of plagioclase probably originated from distinct parental magmas, with low and high Sr content respectively, and they acquired distinct geochemical signatures during their early stage of crystallization. Viccaro et al. (2016b) highlighted similar discrepancies between the Sr/Ba content of plagioclase crystals from several historic (pre-1971) and recent (post-1971) eruptions of Mt. Etna, and they interpreted the low Sr/Ba values (in the pre-1971 magmas) as a feature inherited from a melt with different geochemical signature with respect to the magma feeding the recent activity. The intrusion into the deep Etnean plumbing system of this high-Sr/Ba melt should have progressively replaced the former one over the last decades. Crystals found

in magmas feeding most of the paroxysmal episodes of the 2011, as well as those erupted during February 23, 2013, have a geochemical signature very similar to that of historic plagioclases because of their average Sr/Ba ratio (Sr/Ba = 8.5 for the pre-1971 crystals; cf. Viccaro et al., 2016b). This would be a confirmation that magma batches inheriting different geochemical signatures coexist in the plumbing system of Mt. Etna, and they can be activated contemporaneously (Viccaro and Cristofolini, 2008; Viccaro et al., 2011).

In addition to oscillatory zoning patterns, plagioclase cores and rims related to the 2011-2013 Etnean activity record major episodes of destabilization that manifest as several types of disequilibrium textures. Taking into account the existing experimental studies on plagioclase stability, the development of resorption textures in plagioclase coupled with major changes of compositional parameters (ΔAn~20-30%) may be formed in response of two main different scenarios: a) Decompression of magma under water-undersaturated conditions; and b) Chemical and/or thermal interaction with recharging magmas. The first process produces an increase in partial volatile pressure of the magmatic system. Progressive pressure decrease during magma ascent, therefore, reduces the plagioclase stability field, causing resorption. At the same time, the liquidus plagioclase composition changes toward the calcic end-member (Nelson and Montana, 1992). In the second case, the stability and composition of crystallizing phenocrysts may be also severely affected. As an example, mixing with a more mafic melt will change the composition of plagioclases to more Ca-rich. The same effect will be produced by heating due to injection of hotter magma into a cooler system, even if the two magmatic end-members have similar composition (Tsuchiyama and Takahashi, 1983; Tsuchiyama, 1985). The coexistence of phenocrysts having similar size within the same sample, but

cores with disequilibrium textures at variable pervasive degree of resorption (i.e. coarse sieve, strongly resorbed, patchy) is clear evidence that they underwent different destabilization processes during their early stages of crystallization. I believe that decompression of water under-saturated magma is the main process controlling the formation of this wide spectrum of core disequilibrium textures, as well as the large compositional gradients between core and rim, more than recharge and heating. This interpretation is supported by the rather constant, low Fe and Mg concentrations within cores affected by disequilibrium. Both elements show a general lack of correlation with respect to the An trends, in contrast to what is expected from processes of recharge. However, crystals that undergo the same degree of chemical/physical disequilibrium during decompression cannot develop the same texture. For this reason decompression under variable rates and/or dissolved water content appear the most plausible processes to explain this wide spectrum of textures despite similar anorthite content and size of crystals involved. This hypothesis is consistent with the geometry of the plumbing system of Mt. Etna, which is thought to be constituted by a dense network of magma batches distributed between 2 and 6 km b.s.l. (cf. Patanè et al., 2006, 2013). Throughout the complex transport system of the volcano, magmas can ascend following several unconnected pathways, so that crystals can experience variable chemical/physical conditions and different degrees of destabilization during their history of crystallization.

Disequilibrium textures at the rims of plagioclase crystals primarily manifest as sieve textures of variable width and composition, overgrowing crystal interiors characterized by oscillatory zoning or other disequilibrium textures. The sieve textures preserved in Mt. Etna plagioclases usually display more calcic composition with respect

to the adjacent zones (ΔAn_{20-30}), moreover the highest An compositions ($An_{80–85}$) were found in correspondence of the dustier zones. One of the main chemical features that need to be carefully evaluated for interpretation of plagioclase sieve-textures is that the anorthite variations correlate with minor elements in two different modes within the sieved zones. A first type of sieve texture shows good positive correlation between An and, both Mg and Fe contents, while a second type has increasing Fe at rather constant or decreasing Mg and An. Tsuchiyama (1985) demonstrated that dusty high-An zones may originate during incorporation of plagioclase into a melt with more calcic plagioclase liquidus. Accordingly, sieve textured rims, which show concomitant increase of An, Fe and Mg, may be formed as a result of compositional mixing. Some phenocrysts might be incorporated into recharging melt of a different, more mafic composition, developing high-An resorbed zones prior to the eruption. In such circumstances, the differences in An, Fe and Mg concentration between single crystals should reflect different degrees of chemical interaction between distinct magmatic end-members. Recharge and compositional mixing, however, fail to explain the general lack of correlation between major and minor (Fe, Mg) elements compositions that characterize the second type of sieve textures. Because the iron partitioning in plagioclase is greatly controlled by oxygen fugacity (Wilke and Beherens, 1999; Sugawara, 2001) that in turn does not affect An or Mg content, increasing FeO at rather constant or slightly decreasing An and Mg could be likely the effect of changing fO_2 conditions of the system. The role of oxygen fugacity was previously invoked by a number of authors to describe trends of increasing Fe not associated with major element or Mg increase (e.g. Ginibre et al., 2002b; Ginibre and Worner, 2007; Ruprecht and Worner, 2007; Viccaro et al., 2010; Viccaro et al., 2012;

Viccaro et al., 2014). Ruprecht and Worner (2007) stated that the oxygen fugacity of the system depends on changes in water concentrations, and it can rise in response to increased dissolved H_2O in the melt or exsolved from it. However, increasing dissolved H_2O should shift the plagioclase composition toward the calcic end-member. On the other hand, a process of degassing lowers the water content in the magma, which in turn causes extensive crystallization, and hence it cannot account for development of resorption in plagioclase. In this study, I follow the hypothesis of Viccaro et al. (2014) that, integrating geophysical data with petrological observations, attributed the development of high-Fe sieve textures to the release of dominant gas flushes from deeper levels of the plumbing system, a process that is able to justify the increase in fO_2 of the magmatic system at shallow depth.

As a whole, the chemical zoning associated with resorption textures at plagioclase rim indicates two mechanisms that could have triggered the paroxysmal activity at Mt. Etna between 2011 and 2013: 1) refilling with more mafic volatile-rich magma; and 2) inputs of prevalent gas into the shallow residing system. The occurrence of multiple sieve-textured layers within a plagioclase also indicates that these processes were transient, and likely several inputs of gases or gas-rich magmas at shallow depth were necessary to overcome the partial volatile pressure threshold of the system and finally triggered the eruption.

3.6.5 Magma storage zones and recharging processes inferred from olivine compositional zoning

The investigation of the volcanic rocks emitted at Mt. Etna during the 2011-2013 activity evidenced at least five olivine populations, on the basis of the core compositions.

Compositional and textural differences of these populations of olivine crystals necessarily imply changes of chemical-physical parameters of the magmatic environment in which they form. Experimental determination of Fe-Mg partitioning between olivine and basaltic liquids showed that the $^{Ol/Liq}K_{DFe\text{-}Mg}$ in only slight dependent on temperature and melt composition, being rather constant at 0.30 at pressures <2-3 GPa (Roeder and Emslie, 1970). Conversely, the pressure dependence of $^{Ol/Liq}K_{DFe\text{-}Mg}$ is more marked, in a way that it is positively correlated with pressure (Herzberg and O'Hara, 1998; Putirka, 2005; Toplis, 2005). This means that olivines crystallizing from liquids that are similar in their temperature and composition evolve to lower Fo contents under decreasing pressure. Various studies also demonstrated that, in basaltic systems, oxygen fugacity strongly affects the stability of mafic minerals such as olivine and pyroxenes (e.g., Roeder and Emslie, 1970; Carmichael and Ghiorso, 1990; Snyder and Carmichael, 1992; Berndt et al., 2005; Feig et al., 2010), and exerts a main control on diffusion rates of Fe and Mg (Costa and Morgan, 2010). Indeed, development of resorption and embayments in the mafic phases has been commonly attributed to fO_2 increase of the system more than to variations of the composition or physical parameters of the liquid (Carmichael and Ghiorso, 1990 and references therein). Crystals of olivine and augitic clinopyroxene found in lava samples erupted during short-lasting paroxysmal eruptions (e.g. the episodes of February 28, 2001 and March 04, 2012) exhibit evidence of disequilibrium at their rim; in contrast, disequilibrium is uncommon in crystals of volcanic rocks emitted during the long-lasting paroxysms. This is further confirmation for the important role of fO_2 increase to induce destabilization in the pre-eruptive magmatic system, as also evidenced by the presence of high-Fe sieve textures in plagioclase crystals from lavas

erupted during short lasting paroxysms (see section 3.6.4). In agreement with previous inferences (i.e., occurrence of discordant An% and FeO wt.% behavior in plagioclase sieve textures), the fO_2 increase could be primarily related to processes of gas injection at crustal depths that triggered the paroxysmal activity.

A common feature of the identified olivine populations is that core profiles are rather flat, i.e. they do not present significant compositional zoning over widths of about one hundred μm or more. The occurrence of such features is attributed to crystal residence for significant periods of time within specific magmatic environments, each characterized by definite melt composition, pressure, temperature, oxygen fugacity and volatile component, allowing unperturbed growth of crystals (Kahl et al., 2011, 2013, 2015). In this paper, each identified magmatic environment has been indicated as M_i. At Mt. Etna it was possible to identify five distinct M_i that account for the compositional diversity of the olivine cores: M1 indicates the crystallization environment of the olivine cores at Fo_{84} (OP1); M2 accounts for olivine cores at Fo_{80-82} (OP2); M3 refers to crystals with Fo_{78} cores (OP3); M4 designates the magma where Fo_{75-76} olivines (OP4) form; and M5 accounts for crystals with Fo_{70-73} core compositions (OP5). Different zoning features at the rim of these crystal populations clearly indicate different magmatic histories before the eruption. The compositional zoning observed at the olivine rims is mainly the result of processes of magma exchange between compositionally-different reservoirs, which produced reverse zoning patterns in crystals involved in hybrid magmas originated by mafic recharge and mixing. At the same time, the normal zoning could be evidence of melt differentiation due to fractional crystallization during transfer and subsequent diffusive relaxation of the olivine zoning after intrusion into a more differentiated melt.

Chemical zonings of olivine crystals provide, therefore, key information on the connection among pathways between magmatic environments and the processes of magma intrusion and mixing they underwent during ascent. Prior to analysing these processes is important to understand the P-T-fO_2 characteristics associated with each Mi environments and conditions of crystallization of the olivine populations. Indeed, the opportunity to determine timescales of magmatic processes primarily depends on the definition of physical variables associated with each Mi environment in which olivine grow. Physical parameters such as temperature and fO_2 changes of the magmatic system play, indeed, a main control on processes of chemical diffusion in olivine crystals, and therefore on their final compositional zonings. The effect of pressure on olivine composition and diffusion rate is typically low; this is only significant for $P>10^3$ bars (Costa and Morgan, 2010), which means that it can be neglected in most of the cases. However, we also need to define the pressure of crystallization of the olivine populations to understand whether the identified Mi environments differ in depth, and therefore whether they are part of a single zoned magma reservoir or they are physically separated within the plumbing system of Mt. Etna. Such issues could be addressed using tools based on thermodynamic equilibria such as geothermobarometers. Their use, however, requires the occurrence of mineral phases that coexisted in equilibrium during magma evolution. In a complex magmatic system such as that of Mt. Etna, which is affected by multiple and repeated mixing events, it is difficult to recognize coexisting equilibrium compositional pairs, an issue that was also highlighted by Kahl et al. (2015) for the definition of thermodynamic parameters of Mt. Etna magmas during the period 1991-2008. Moreover, several olivine compositional populations were found in the same lava sample. This

means that the use of modern barometry, based for example on clinopyroxene and/or plagioclase equilibrium, is not appropriated to constrain the physical nature of magmas in which olivines form.

The approach adopted in this study consists of simulating the physical-chemical evolution of Etna's magmas, from the crustal-mantle transition depth to the surface, using rhyolite-MELTS software (Gualda et al., 2012). The use of MELTS modelling to constrain the P-T-fO_2 crystallization conditions of our compositionally distinct olivine crystals is possible because the olivine cores are characterized by rather constant Fo composition, which reflect initial growth of crystals under precise magmatic conditions (a combination of melt composition, pressure, temperature, oxygen fugacity, and dissolved H_2O+CO_2 volatiles) that represent equilibrium or near-equilibrium conditions held constant for some time. We tried to reproduce the observed olivine compositions together with the composition of the plagioclase populations that are present in the volcanic rocks, attempting to evaluate which composition of plagioclase could have reasonably coexisted with a given olivine population.

Magma differentiation was simulated starting from a primitive melt obtained from the bulk rock composition of the most basic products of the 2011-2013 activity at Mt. Etna, i.e. the composition of a lava sample from the March 04, 2012 paroxysm (Table 4). This is one of the most basic magmas emitted since 2006 that could likely represent the less differentiated magma actually present in the feeding system. Because the crystallization of the most forsteritic olivine found in our samples (i.e. Fo_{84}), required a more primitive starting composition, the composition of the March 04, 2012 sample was first equilibrated to a composition representative of equilibrium with a primary liquid

generated from a mantle peridotite. The re-equilibration procedure was performed by introducing back into the system the mineral assemblage we observed in thin section (plg+ol+cpx+ox in a total volume of 23%); then, the primary melt composition was constrained by adding 46% of a mafic mineral assemblage, constituted by Fo_{86} olivine (60 vol.%), clinopyroxene with Mg# 85 (10 vol.%), Ti-oxide (6 vol.%) and amphibole (2 %) until the crystallizing olivine within the magma was equilibrated to the composition of forsteritic olivine found in mantle peridotite ($Fo_{88–90}$).

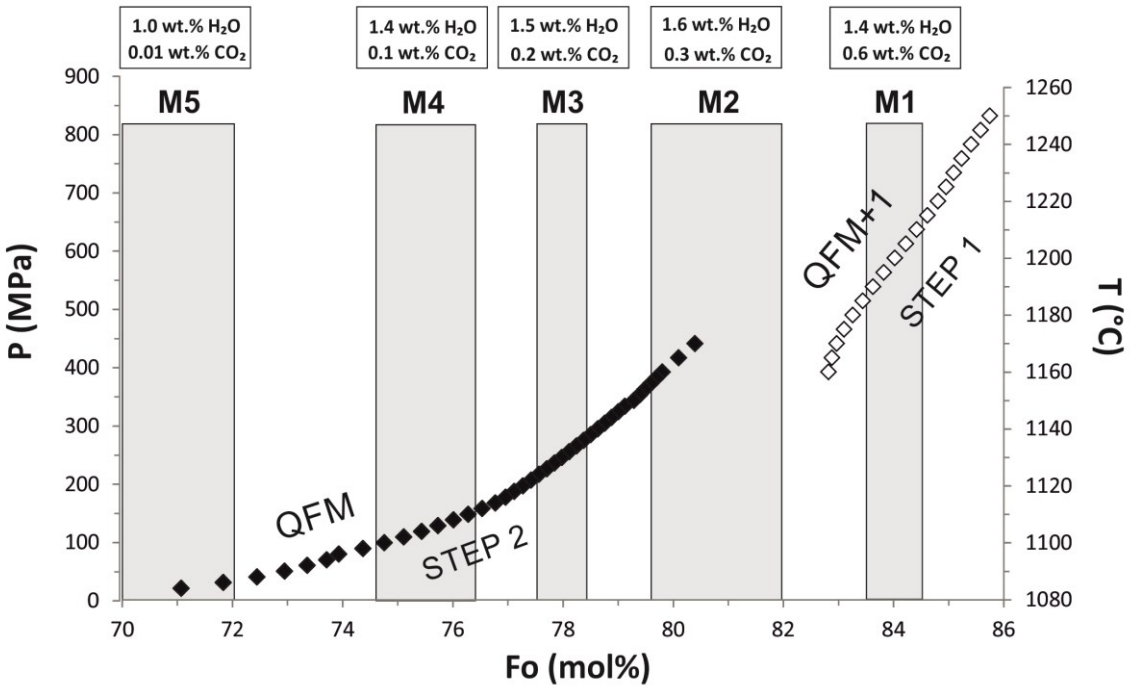

Figura 25. *Schematic illustration of thermodynamic parameters related to distinct magmatic environments (Mi) at Mt.Etna, as defined by rhyolite-MELTS modeling. The evolution of the melt was reproduced through two steps of modeling: the first step (white diamonds) was performed at the QFM+1 buffer, while the second (black diamonds) at the buffer QFM. The changing composition of the melt during evolution (Fo mol% on the x-axis) is shown as a function of pressure and temperature (vertical axes). For each identified environment,the average H_2O and CO_2 content is reported in white boxes at the top.*

Starting from this primitive melt composition, which is given in Table 4, the chemical evolution of melt has been tracked along multiple P-T intervals, assuming that differentiation takes place during crystal and fluid fractionation (i.e. separation of H_2O and CO_2 from the magmatic system), and assuming variable fO_2 buffer (QFM+1, QFM, QFM-1). Several hundred runs (n>500) have been conducted in order to fix reliable chemical (fO_2, H_2O and CO_2 contents) and physical (P, T) constraints of the system able to reproduce a mineral assemblage consistent with petrographic and compositional observations. Specifically, the temperature range has been investigated from the *liquidus* to 1080°C, which is the lowest value obtained from direct measurement of lava temperatures at the volcano vents (Tangui and Clocchiatti, 1984). The range of pressure has been varied between 900 MPa and 30 MPa to simulate the differentiation of magma from the crust-mantle boundary (~25 km depth; c.f. Cristofolini et al., 1985) up to the shallower portions of the plumbing system (at~ 1.5 km below the summit craters; c.f. Bonaccorso et al., 2011; Patanè et al., 2006, 2013). We also used several initial concentrations of H_2O and CO_2 in the range 3.5-0.5 wt.% and 0.5-2.0 wt.%, respectively. The choice of these values was based on the H_2O-CO_2 content of melt inclusions that were found in primitive olivine from recent Etnean eruptions (Metrich et al., 2004; Spilliaert et al., 2006a; Collins et al., 2009). Within these chemical-physical constraints, the most appropriate MELTS simulations consistent with our petrographic and microanalytical observations, were obtained in two steps, by reproducing the magma differentiation along two distinct P-T-X intervals, assuming an oxygen fugacity buffer QFM+1 at high (>400 MPa) pressure conditions and QFM for differentiation at low (<400 MPa) pressure. The first step simulates melt differentiation in a range of

temperature of 1250-1160 °C and pressure of 850-400 MPa. This leads to clinopyroxene, oxide and Fo_{86} olivine as the first crystallizing phases at the highest P-T values. The most basic Fo_{84} olivine (OP1) found in our samples occurs at temperature 1210-1200°C, and pressure 650-600 MPa, for fO_2 between 1 and $1.9*10^{-7}$ bars. The initial water content was assumed as 1.1 wt.%. This value is in the range of water concentrations given by Collins et al. (2009) for melt inclusion found in olivine of the 2007 magma, which is the magma most similar in composition to the 2011-2013 products for which melt inclusion data are available. The CO_2 content was set at 0.5 wt.% . Although the 2007 and post-2007 products have proved to be volatile-rich with respect to the CO_2 component (Aiuppa et al., 2007; Collins et al., 2009; Nicotra and Viccaro, 2012a), their water content is low compared with the H_2O proportions of magmas emitted in past years (>3 wt. % for the 2001 and 2002-2003 magmas; Metrich et al., 2004; Spilliaert et al., 2006a). This could reflect relative melt dehydration coupled to CO_2-flushing already experienced in the deep portion of the plumbing system. It is also worth noting that assuming higher initial H_2O and CO_2 content, phase equilibria and mineral compositions do not match those identified from petrography and microanalytical data. The crystallization of more evolved (<Fo_{82}) olivine populations requires, however, changes in the redox conditions of the system. For this reason, a second step modelling was performed at the QFM oxygen fugacity buffer to reproduce melt differentiation throughout the low-intermediate (from 400 MPa) and shallow (down to 30 MPa) feeding system of Mt. Etna. The starting melt composition was obtained from the first step at P=400 MPa, T=1060 °C, with 1.64 wt.% of dissolved H_2O. The concentration of CO_2 in the system was increased to 2.0 wt.% in order to allow low-pressure crystallization of the more evolved olivine populations. The addition of more

CO_2 also accounts for the more reduced redox condition associated with the magmatic environments located at pressure above 400MPa. Assuming these initial physical and chemical conditions, the system produces olivine Fo_{80} (OP2) within a P range of 400-380 MPa, T between 1160 and 1156°C, and fO_2 of 3.5-3.0*10^{-9} bars. Olivine Fo_{78} crystallizes from 290 MPa at 1136 °C and fO_2=1.4*10^{-9} bars, to 230 MPa at 1126°C, fO_2 1.0*10^{-9} bars. The occurrence of Fo_{75-76} olivine (OP4) is consistent with magma storage and differentiation at pressure between 160 and 130 MPa, corresponding to magmatic temperatures of 1112-1106 °C and fO_2 of 5.9-4.7*10^{-10} bars. Within this P-T space, Fo_{76-75} olivine coexists in equilibrium with plagioclase An_{80}, which represents one of the most common plagioclase compositions found in the Etnean samples. The most evolved Fo_{73-70} olivine (OP5) forms at very low pressure conditions of ~30 MPa, and temperature of 1088°C, with fO_2 2.3-2*10-10 bars. At these conditions, the OP5 olivine coexists with Ca-poor plagioclase with composition An_{70-65}.

Table 4. *Major oxide composition (wt.%) of the most basic lava erupted during the 2011-2013 paroxysmal sequence (sample 04Mar12) and its re-equilibrated composition used as starting melt composition for rhyolite-MELTS modeling.*

Sample	SiO_2	TiO_2	Al_2O_3	FeO_{tot}	MnO	MgO	CaO	Na_2O	K_2O
04Mar12	47.01	2.02	16.28	12.09	0.22	5.61	11.00	3.33	2.00
Primitive melt	45.42	1.52	13.08	11.75	0.18	14.53	9.66	2.27	1.25

The accuracy of these results relies on the good correspondence between the retrieved olivine and plagioclase compositions, very close to those found in rock samples, and the P-T path at which they should forms based on rhyolite-MELTS modelling. In particular, the pressure intervals characterizing the M*i* environments of all the compositions with Fo≤78 are in good agreement with depths of the main storage volumes in the intermediate and shallower parts of the plumbing system constrained on the basis of geophysical data (e.g. Bonaccorso et al., 2011; Patane et al., 2013). All the models present in literature provide, indeed, evidence for an elongated storage volume ranging between ~2 and ~6 km below sea levels, which constitute the intermediate portions of the plumbing system of Mt. Etna. Considering that the crustal density beneath the volcano is about 2.8 g/cm^3 (Corsaro and Pompilio, 2004), these depths correspond to a pressure range spanning from ~130 to ~260 MPa, which match well the pressures of crystallization of olivine with composition Fo_{76} and Fo_{78} respectively. The crystallization of olivine Fo_{72-70} is also largely consistent with magma differentiation during its final stage of ascent, from the shallowest magma zone located at 1-2 km above sea level (~40 MPa; Patanè et al., 2016) to the surface. One compositional aspect that deviates from MELTS results is that the full range of plagioclase compositions was not reproduced through this two-step modelling. Specifically, the crystallization of the most calcic An_{85-90} plagioclase implies a very different P-T-X-fO_2 evolutionary path for magmas than those followed for the other compositions. Conditions that better reproduce plagioclase An_{85-90} include low pressure <100 MPa, temperature <1090°C, and higher water content >2 wt.%.

Thermodynamic modelling suggests that olivine populations form in physically distinct magma environments located at distinct depths of the plumbing system, each

characterized by its own temperature, oxygen fugacity and volatile content. By a systematic analysis of the compositional heterogeneities of olivine crystals, it is now possible to define how the different M_i are interconnected with each other and how they were reactivated before each paroxysmal episodes at Mt. Etna. In order to illustrate the connection between reservoirs and processes of magma exchange for the eruptive episodes of the 2011-2013 periods, we used a method of illustration similar to that used by Kahl et al. (2011; 2015). This method involves boxes that represent the compositionally different M_i and arrows to indicate the pathways of magma transfer between the M_i storage zones (Figs. 26-27.). The normally zoned rims overgrowing the most magnesian (Fo_{84}) OP1 cores indicate preferential magma transfer from M1, toward more evolved M2 and M5 storage zones, where OP1 olivines likely reside for a certain period of time, undergoing partial equilibration of the Fe-Mg zoning prior to eruption (Fig. 23a-b).

The crystallization of the OP2 olivines (~Fo_{80-82}) occurred from a magma M2 that is slightly more evolved than M1. The normal zoning patterns of OP2 with prevalent decreasing concentration to Fo_{75-76} indicate that the M2 magma intrudes in the M4 reservoir (Fig. 23c). In contrast, the reversely zoned envelopes observed in some OP2 olivines (up to ~Fo_{84}) reflect interaction with a magma that is necessarily more basic, and whose equilibrium olivine must be more forsteritic than Fo_{81}. Because we observed decreasing Fo content to ~Fo_{80} at the rim of OP1 olivines coupled with Fo increase around some OP2 crystal cores, it appear evident that a mixing process involved M1 and part of the M2 magma, (Figs. 23a-d). The result of this partial mixing between M1 and M2 is a hybrid magma, which carried during its ascent the OP1 and OP2 olivines toward

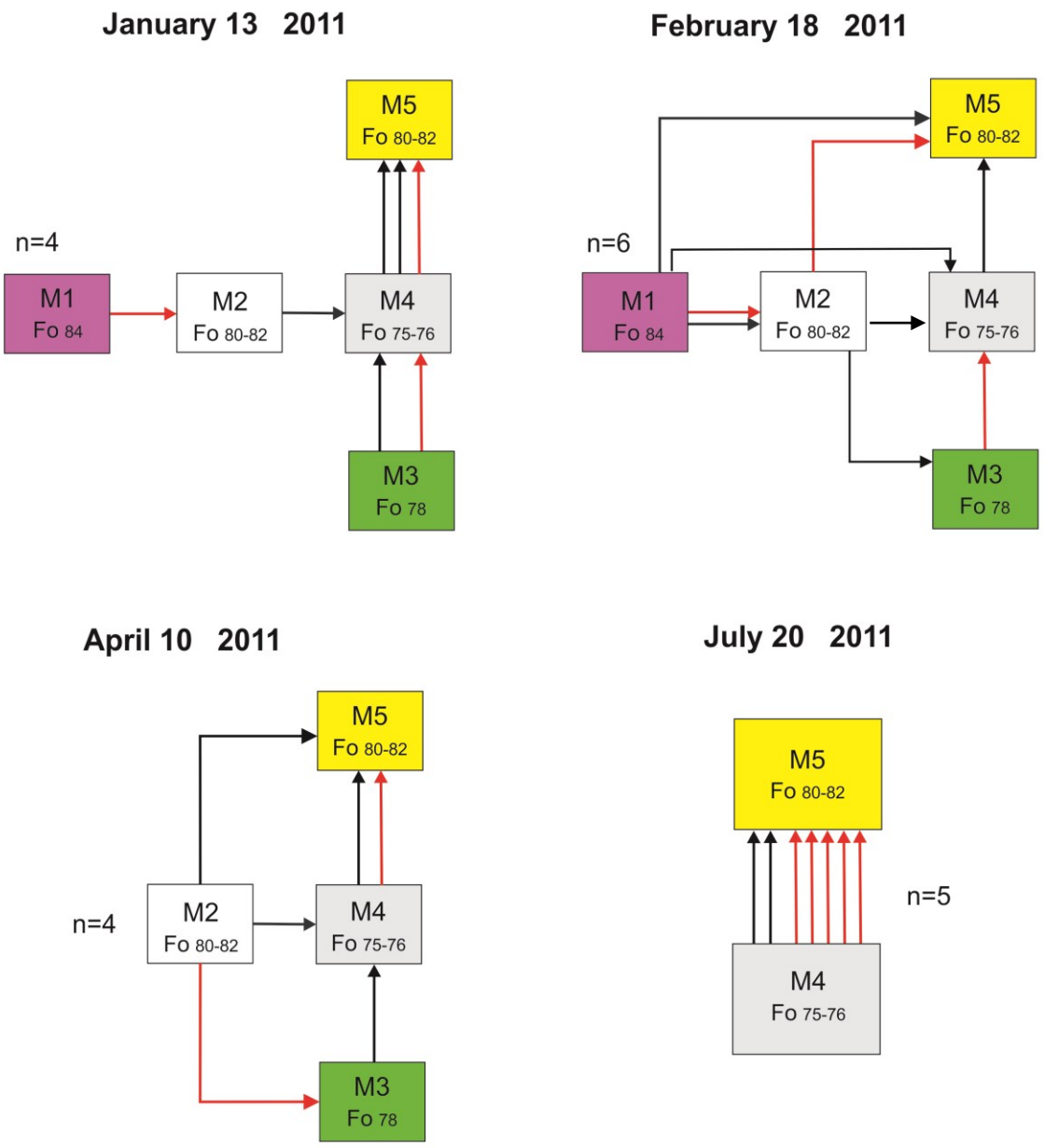

Figure 26. *Connections between the magmatic environments defined throughout the zoning patterns of olivine crystals found in lavas of the 2011 paroxysmal episodes. Each colored box represent a different magmatic environment. Arrows indicate the direction of magma transfer as recorded from olivine zonings. Black arrows: normal zoning; red arrows: reverse zoning patterns.*

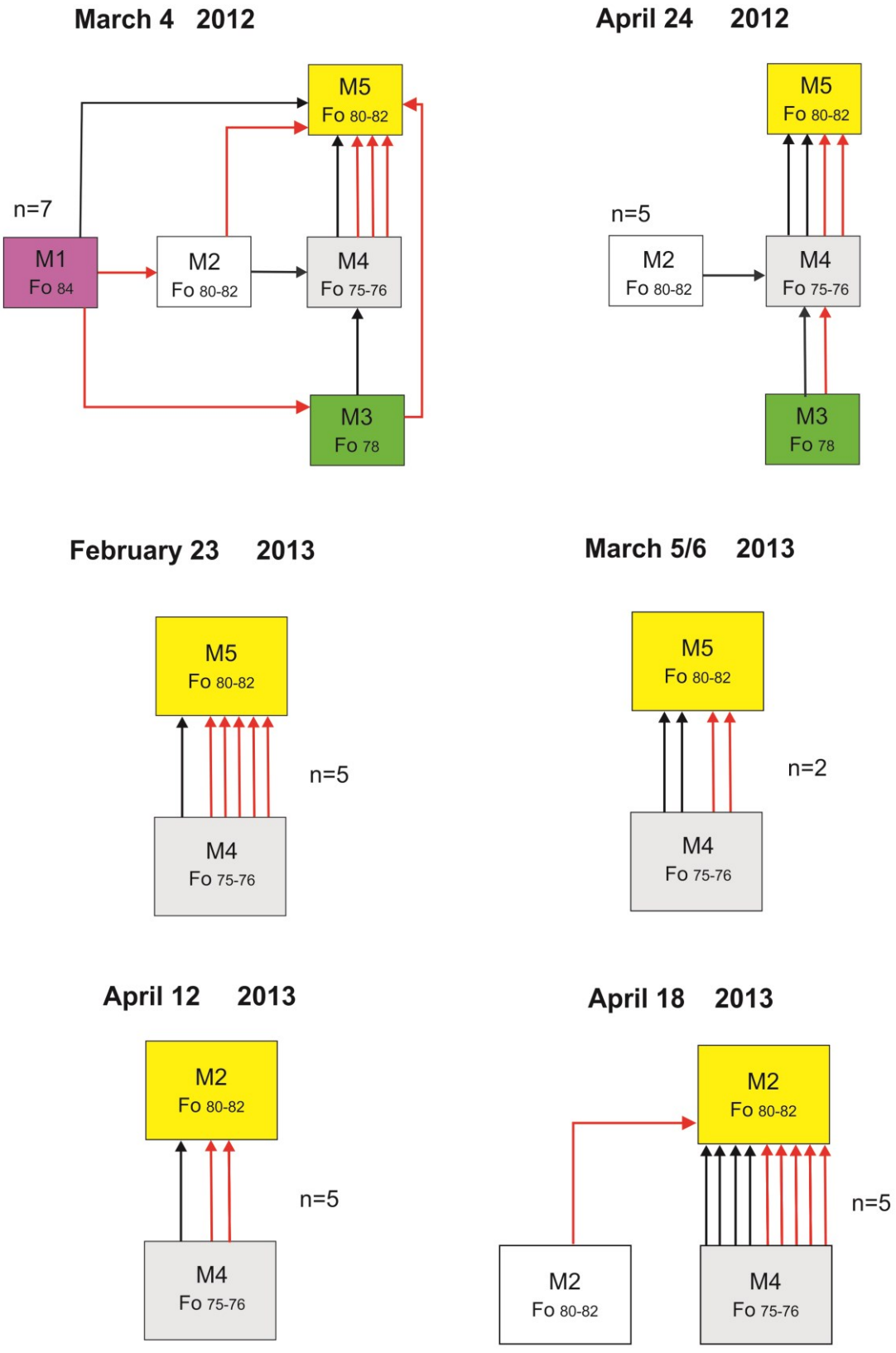

Figure 27. *Connections between the magmatic environments defined throughout the zoning patterns of olivine crystals found in lavas of the 2012 and 2013 paroxysmal episodes. Boxes and arrows as in Figure 26.*

the shallow M4 reservoir. This is consistent with the observation that, both, OP2 and some of the OP1 crystals record normally zoned rims with decreasing Fo to about Fo_{76} (Figs. 23a-d). We also can infer that the mixing process between M1 and M2 had very fast timescales because the majority of the OP2 olivines did not register any reverse zoning. This feature could be attributed to lack of complete homogenization of the magma volume involved in the mixing process probably due to the rapid magma ascent towards shallow levels (i.e. toward the M4 storage zone). This prevented the development of compositional changes to higher Fo in some of the OP2 crystals.

Compositional zoning data support the occurrence of further episodes of mixing between compositionally distinct end-members at shallower depths beneath the NSEC (Figs. 26-27). Processes of magma interaction clearly occurred between M1 and a more evolved magma stored in the crust, namely M3, as suggested by the more fayalitic core compositions of OP3 olivine crystals (~Fo_{78}) with respect to OP1 and OP2. Magma mixing is, indeed, markedly evident at the rim of OP3 olivines, which typically show increasing Fo content from Fo_{78} at the cores up to $Fo_{82\text{-}84}$ towards the rims (Fig.23e). End-members of another interaction are the M2 and M4 magmas. In this case, only the minority of the OP4 olivines (Fo_{76}) have reverse zoning patterns with slight Fo concentration increases (about ΔFo1%; Fig. 23h). This feature is similar to that observed for the OP2 ($Fo_{80\text{-}81}$) crystals, suggesting the occurrence at shallow crustal depth of another fast process of magma mixing involving partial homogenization of the resident system, i.e. the M4 magma. On the whole, olivine populations crystallizing from M2, M3 and M4 record direct transfer histories to the most differentiated M5 environment (Figs. 26-27). Here, the arrival of magmas with different degrees of differentiation from deeper

levels of the plumbing system caused the reverse zoning that characterizes the rim of OP5 crystals ($Fo_{70-73;}$ Figs. 23i-l). The differences in Fo concentration recorded at the edge of these crystals could reflect different degrees of chemical interaction between M5 and the more basic M2, M3 and M4 magmas. Eruptions occurring during the 2011-2013 period are likely direct consequences of these recharge and mixing processes within the more evolved shallow storage zone (at ~1-2 km of depth), from which magmas rise directly to the surface. Clear evidence of this hypothesis is that OP5 olivines generally do not record any subsequent normal zoning at the outermost rim, a feature in accordance with a relatively fast migration of magma to the surface (Figs. 23i-l).

The compositional range preserved in olivine crystals from the 2011-2013 eruption sequence mainly highlights processes of multi-stage magma mixing and transfer that involve five end-member magmatic environments, which are variously connected with each other. The frequency of different olivine populations and their different zoning patterns within each lava sample provide also the opportunity to understand how the M*i* environments have been activated before each episode of the 2011-2013 sequence (Figs. 26-27). In these regard, we observed that magmas feeding the paroxysmal eruptions rose up stepwise toward surface, following two dominant routes of migration: a) from M1 to M2 and, then, to M4 and M5; and b) from M3 to M4 and finally M5 (Figs. 26-27). In the case of some short-lasting paroxysms, I recognized preferential routes that have facilitated the transfer of primitive Fo_{84} and Fo_{82-80} magma toward surface by a single step of decompression, prior to the final stage of ascent upon eruption. For example, olivine zoning patterns from lavas of the February 18, 2011 and March 04, 2012 episodes suggest processes of replenishment of the shallow M5 reservoir with the mafic M1 and M2 melts,

therefore highlighting a main connection route between the M1 or M2 and M5 storage zones (Figs. 26-27). This implies that crystals and their host melts do not pass through all the intermediate storage zones or, alternatively, that the transfer of magma was too quick to be recorded in the chemical zoning of olivine with intermediate composition between OP1 and OP5. Because we observed that these migration routes can be found only in some eruption products, they could represent routes of magma transfer that were reactivated only occasionally, and thus were selectively recorded in the zoning profiles of all the olivine crystals.

3.6.6 Time constraints of magma residence and transfer by modeling the chemical zoning of plagioclase and olivine crystals

The complex compositional and textural features of the Etnean plagioclase provide primary evidence that crystals experienced different crystallization histories from nucleation to eruption, developing specific growth/resorption features depending on the chemical and physical conditions of the magmatic system. In particular, the distinct characteristic found at the plagioclase cores (i.e. resorption texture with distinct pervasive degree of resorption) suggests that the timing and rates of magma transfer from the deep portion of the plumbing system to the surface may have been different over the period under investigation. On the other hand, the chemical record of the olivine crystals provides information on the number of storage zones in which magmas reside before eruption, how they are interconnected with each other, and the routes magmas have followed during ascent. However, some first-order questions remain still unsolved, such as how long crystals remain in the plumbing system of Mt. Etna prior to the eruption, how

long they reside within different magma storage zones, and at what rates they moved from one reservoir to another before emission. Understanding the rates of such processes is crucial for the development of models of magma emplacement, remobilization and eruption at active volcanoes, which have, in turn, important implications for volcanic hazard assessment and mitigation. Time constraints to the above mentioned magma dynamics are provided by modeling the observed plagioclase and olivine zoning patterns by diffusion. Specifically, diffusive relaxation through time of the strontium zoning in plagioclase has been used to define maximum residence times of crystals in the plumbing system of Mt. Etna for selected eruptions of the 2011-2013 paroxysmal sequence. Normal and reverse zoning patterns of olivine crystals were modeled by Fe-Mg diffusion in order to constrain timescales of magma intrusion and residence in the each crustal reservoirs, and the rates of migration between them. Details on the diffusion modeling strategies on plagioclase and olivine crystals and modeling results are provided below.

3.6.6.1 Plagioclase residence time in the plumbing system of Mt. Etna

The diffusive relaxation through time of the strontium zoning in plagioclase has been used to define maximum residence times of crystals in the plumbing system of Mt. Etna during the 2011-2013 paroxysmal sequence. The efficacy of modeling Sr diffusion in plagioclase relies on the very fast diffusivity of Sr (Gilletti and Casserli, 1994) compared to other element diffusion (Grove et al., 1984). This behavior prevents the re-equilibration of An content over time, while Sr concentrations change at variable rates, depending on the compositional and physical characteristic of the host melt. The diffusion rate of Sr in plagioclase of different compositions has been experimentally calibrated (Gilletti and Casserly, 1994), and can be calculated for the Etnean plagioclases if the

anorthite composition and the temperature are known. If the initial Sr concentration profile in plagioclase can be also estimated, a diffusion model can be used to calculate the time required to attain the observed concentration profile.

Plagioclase crystals from the Etnean magmas have been modeled using a one-step diffusion approach, namely the model provided by Zellmer et al. (1999), which has the advantage of calculating average residence times for the entire crystal by modeling the strontium diffusive relaxation after the crystal has formed. It is worth noting that chemical diffusion in natural crystals can be modeled either in one single step, under the assumption that diffusion started after the entire crystal had grown, or zone by zone, using multistep models (e.g. Druitt et al., 2012). Compared to the one-step model, the multistep approach ensures a more detailed tracking of the crystal history, because it can yield time estimates for each step of growth that a crystal experienced before eruption. However, a multistep modeling approach on plagioclase crystals from Mt. Etna is extremely hard to reproduce because most of the Etnean plagioclase crystals are characterized by multiple and extensive resorption zones both at their cores and rims. This means that some portions of crystals have been removed, hence the model would yield inaccurate residence times. Application of the multistep diffusion modeling would be therefore restricted only to crystals with oscillatory-zoned patterns or to portions of crystals not severely affected by μm-sized glass inclusions caused by disequilibrium. However, even in these cases, the occurrence of repeated minor dissolution surface cross-cutting the oscillatory zoning envelopes precludes proper estimations of the total residence time of plagioclase crystals.

The modeling approach used in this study (i.e. Zellmer et al., 1999) assumes that diffusion starts after the entire crystal has grown, and therefore, the retrieved crystal

residence times at magmatic temperatures could be overestimated with respect to the time of growth of the crystal. The definition of parameters such as the An content and the temperature, which affect the Sr diffusivity, or the choice of the initial strontium concentration can also produce errors in the final residence time calculations of orders of magnitude. These sources of errors have been, therefore, minimized by considering the highest An content in the crystal, which ensures the lowest diffusion velocity and, therefore, leads to maximum residence time estimations.

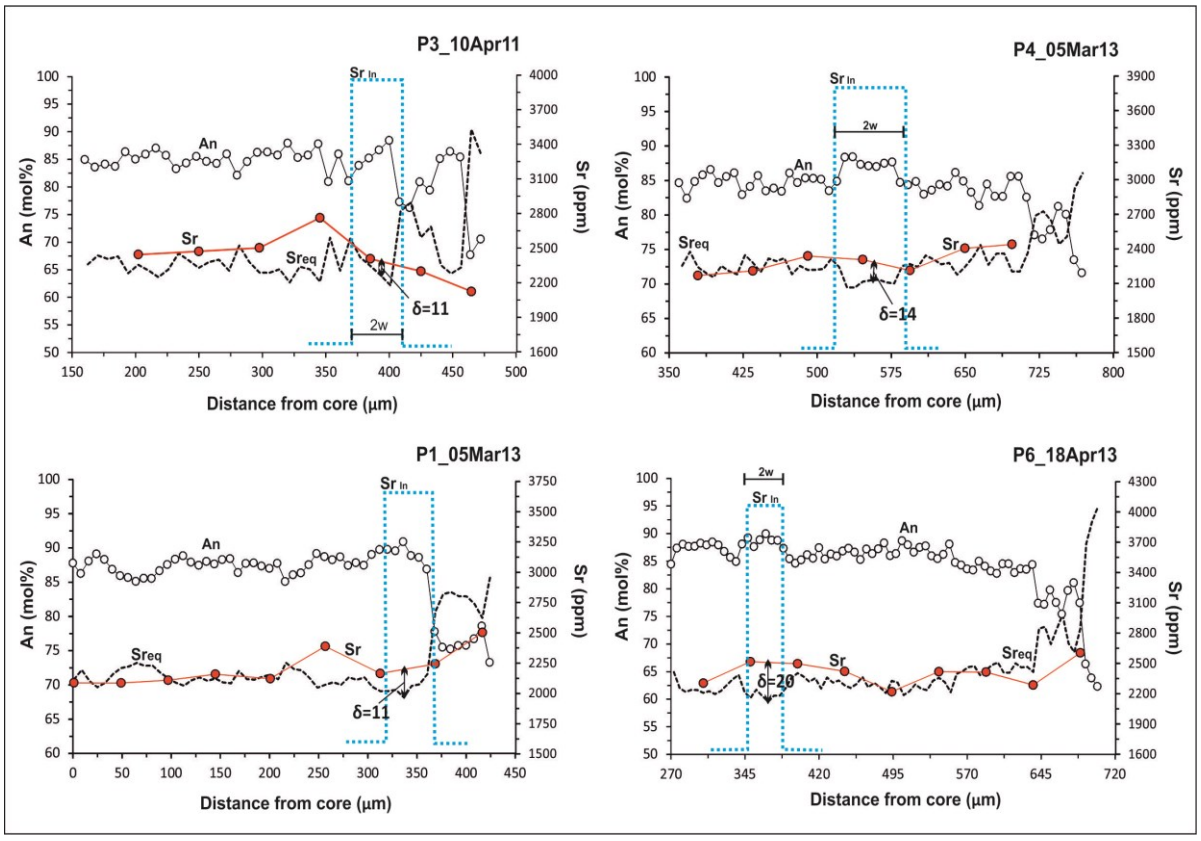

Figure 28. *Examples of application of Sr diffusion modeling to plagioclase crystals from 2011-2013 volcanic products of Mt.Etna. The maximum range in the initial Sr concentration is represented as a square-wave signal (dotted blue lines) of width 2w. Sr_{in} is the strontium concentration at the time t=0. After a total residence time t, the amplitude of the signals drops to the measured Sr concentration in the crystal. Sr_{eq} represents the strontium concentration when equilibrium through diffusion is achieved. δ (in %) is the un-diffused portion of Sr remains un-diffused before eruption. $\delta = Sr-Sr_{eq}/Sri_n-Sr_{eq}$*

Based on these assumptions, the adopted modeling strategy may be described as follows. After the crystal has grown, its compositional zoning is given by alternating zones with initial Sr concentrations (Sr_{in}). Over time the initial Sr zoning amplitude decreases towards the equilibrium compositions (Sr_{eq}), while the An content of the crystal remains rather unvaried. After eruption, if complete equilibration has not been reached, the measured Sr profile within the crystal lies between the initial and the equilibrium concentrations. The first step to model the Sr diffusion in plagioclase crystal requires, therefore, to test if the measured Sr concentrations are or are not in diffusive equilibrium. In order to evaluate the degree of Sr disequilibrium across the plagioclase zoning, we have first calculated Sr equilibrium compositions using the plagioclase-melt partition coefficient for Sr (D_{Sr}) from Blundy and Wood (1991). Because the partitioning of Sr in plagioclase is largely controlled by the crystal chemistry and relates to the An content, equilibrium profiles have been determined using An-dependent Sr partition coefficients that account for An variation across the plagioclase crystals (cf. Zellmer et al., 1999; 2003). D_{Sr} was calculated for all the crystals at the temperature of 1100°C, in accordance with the experimental geothermometer of Pompilio et al. (1998) calibrated for Etnean hawaiites and for liquids in equilibrium with plagioclase, augitic clinopyroxene, titaniferous magnetite ± olivine.

Following Zellmer et al. (1999), one way to assess the initial Sr profiles is the definition of the maximum range in the Sr concentration. This compositional range within a single plagioclase crystal has been found to vary by no more than a factor of 2.5, on the basis of published data. This allows estimation of the initial Sr concentration that can be represented as a square 2w-width wave signal in each crystal (Fig. 28). Starting from the

initial Sr concentration, the time required to reach the measured Sr compositional profile was calculated by means of a standard diffusion equation that depends on the Sr diffusivity and the width of the zone over which diffusion processes can be modeled (i.e. Eq. 12 in Zellmer et al., 1999; Fig. 28). A proper selection of the zoning interval suitable for calculation of the maximum timescales of crystal residence requires two conditions: a) occurrence of Sr diffusive disequilibrium; b) identification of the crystal zone with the slowest diffusivity, which implies that the 2w-square wave is centered on the highest XAn zone of the crystal (Fig. 28). Calculation of the Sr equilibrium profile has been performed for all the analyzed crystals, however only 17 plagioclases show the two above-mentioned conditions, making them suitable for application of the Sr diffusion modeling. The Sr diffusivity (ĐSr) in the Etnean plagioclases was calculated on the basis of experimental results of Giletti and Casserly (1994) at the temperature of 1100 °C and at the highest An concentration (mole fraction) of any crystal. Calculated ĐSr values range from $1.14x10^{-18}$ to $9.52x10^{-19}$ m^2s^{-1} for a X_{An} range of 0.65-0.90 (Table 5).

Following the model of Zellmer (1999), the diffusive relaxation of Sr with time could be expressed as variation of δ, which represent the undiffused portion of Sr with respect to its initial value (Sr_{in}) in any plagioclase crystal; diffusion curves resulting from the application of Eq.12 of Zellmer et al. (1999) are shown in Fig. 29.

Maximum residence times calculated for plagioclase crystals range from a minimum of ~5 years for a plagioclase of the January 13, 2011 eruption to a maximum of 31 years for a crystal emitted during the eruption of March 5, 2013 (Figs. 29-30; Table 5). On the whole, Sr diffusion calculations indicate that the residence times in the plumbing system are, on average, longer for crystals of magmas erupted during the first months of

the 2013 AD (i.e., eruptions of February 23, and March 05, 2013), whereas crystals from the activity at the beginning of 2011 (i.e. eruptions between January 11 and April 2011), and those from the eruptions occurred at the end of the paroxysmal sequence (i.e., eruptions of April 2013) exhibit generally shorter timescales, on the order of 5-10 years (Fig. 30). It is also noted a good positive correlation between the plagioclase sizes and timescales of crystal residence, in a way that the greater is the size of the modeled crystal the longer is the time elapsed in the magmatic system (Fig. 30). This is in accordance with the assumption that plagioclase crystals greater in size start to form at deeper levels of the plumbing system.

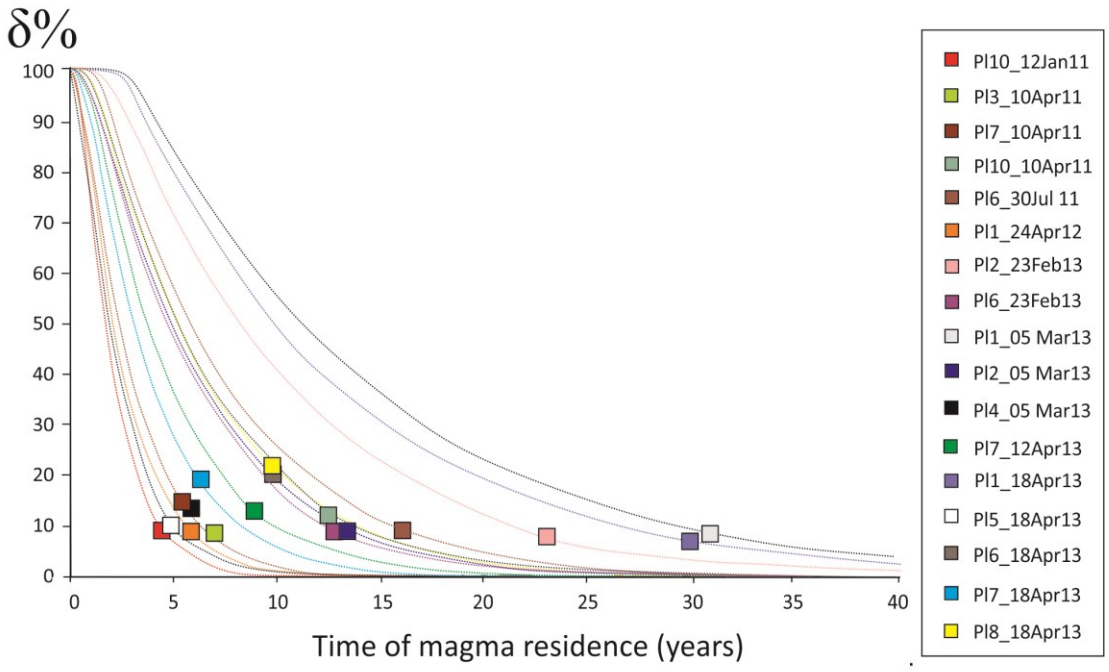

Figure 29. *Illustration of Sr diffusion curves showing the decrease with time of the parameter δ for plagioclase crystals of the 2011-2013 period of eruption. Colored squares indicate the δ value of each modeled crystal and the associated time of residence. δ was determined by taking into account the compositional gap between the measured and the equilibrium profile of Sr within the plagioclase zone at highest An.*

These results refer to average maximum residence times of crystals in the magmatic system, which may be overestimated with respect to timescales derived using other approaches for magma residence calculation, as mentioned previously (cf. Armienti et al., 1997; Kahl et al., 2011; 2013; 2015; Druitt et al., 2012). Uncertainties of ±10°C in the choice of temperature do not significantly affect these estimations, indeed the error on the final calculated timescale is of order ±2 years. Even considering overestimations due to application of a one-step diffusion modeling or the associated errors, these calculations highlight important differences in the residence times of crystals related to different eruptions over the entire 2011-2013 period of activity. Moreover, despite the general correlation between crystal sizes and calculated residence times, some crystals from the same eruption, and with similar size and texture, exhibit difference in residence time on the order of 7 years (i.e., plagioclase P2 and P4 from the eruption of March 05, 2013). This behavior could be the consequence of different modes and rates of magma transfer within the complex plumbing system of Mt. Etna, an issue already evidenced through textural investigations of plagioclase crystals. The recent study of Kahl et al. (2015) also supports this inference, demonstrating for the eruptive period 1991-2008 at Mt. Etna that transfer times and migration routes between different magmatic environments may change substantially even within a single eruption at the scale of years/decades.

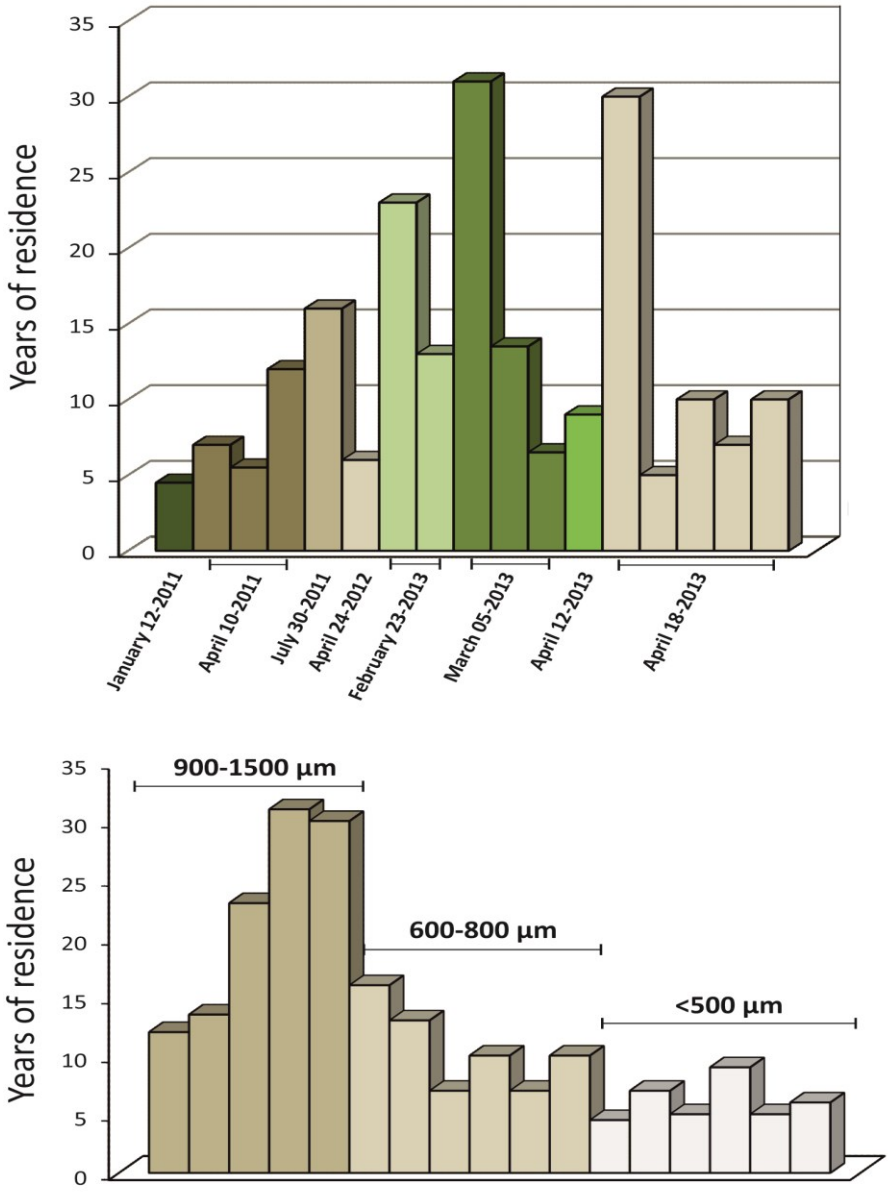

Figura 30. *Calculated residence times (years) for plagioclase crystals of the 2011- 2013 eruptions***.** H*istograms at the top highlight the differences in residence time among distinct eruptive episodes for which plagioclase diffusion modeling was performed. Histograms at the bottom shows the retrieved timescales for plagioclase crystals having distinct size.*

***Table 5**. Parameters used for diffusion modelling on plagioclase crystals suitable for calculations with estimation of residence times. All crystals modelled at temperature of 1100°C.*

Crystal	Eruption year	X_{An}	ĐSr (m^2/s)	2*w* (μm)	δ %	Time (yrs)
12Jan11_P10	2011	0.89	$5.88*10^{-19}$	18	10	4-5
10Apr11_P3	2011	0.88	$6.46*10^{-19}$	24	10	7
10Apr11_P7	2011	0.69	$6.22*10^{-18}$	50	16	5-6
10Apr11_P10	2011	0.87	$6.46*10^{-19}$	45	14	12
30Jul11_P6	2011	0.86	$7.80*10^{-19}$	40	11	16
24Apr12_P1	2012	0.85	$8.58*10^{-19}$	28	10	6
5Mar13_P1	2013	0.91	$4.86*10^{-19}$	44	11	31
5Mar13_P2	2013	0.91	$4.43*10^{-19}$	28	11	13-14
5Mar13_P4	2013	0.88	$6.46*10^{-19}$	24	14	6-7
12Apr13_P7	2013	0.88	$7.01*10^{-19}$	30	14	9
23Feb13_P2	2013	0.89	$5.88*10^{-19}$	40	10	23
23Feb13_P6	2013	0.65	$5.61*10^{-18}$	150	11	13
18Apr13_P1	2013	0.67	$4.64*10^{-18}$	150	10	30
18Apr13_P5	2013	0.87	$7.10*10^{-19}$	21	12	5
18Apr13_P6	2013	0.90	$5.35*10^{-19}$	30	20	10
18Apr13_P7	2013	0.87	$7.0*10^{-19}$	91	17	7
18Apr13_P8	2013	0.84	$1.04*10^{-18}$	28	22	10

3.6.6.2 Fe-Mg diffusion modeling in olivine crystals and timescale of magma storage and recharge beneath Mt. Etna

In order to assess timescales of open system processes such as magma intrusion and mixing that preceded the paroxysmal episodes at Mt. Etna between January 2011 and April 2013, the approach of Costa et al. (2008) and Costa and Morgan (2010) was adopted to model the diffusion-controlled relaxation of the Fe-Mg zoning of olivine. The used model is a one-step type, but the modelling strategy is quite different than that used for modelling plagioclase crystals. Following Costa and Morgan (2010), diffusion processes are described through partial differential equations and, then, solved numerically. In numerical implementations, concentrations are described as a function of space (x) and time (t) and are directly related to values of the diffusion coefficients (D) along the measured profile. This allows evaluation of the evolution through time of the initial concentration profile of the crystal that can be traced until a new profile that fits the measured concentration profile is obtained.

Due to the strong diffusion anisotropy, olivine crystals were preliminarily selected to minimize uncertainties on time determination related to the section orientation with respect to the fast diffusion direction (c-axis), following the selection criteria listed in Costa and Chakraborty (2004) and Shea et al. (2015). The modelling has been performed by using Fick's Law-based diffusion equations with concentration-dependent diffusion coefficients ($D_{Fe\text{-}Mg}$) and assuming the measured concentrations at the rim of crystals as boundary conditions. The expression for calculating the Fe-Mg diffusion coefficients along [001] is from Dohmen and Chakraborty (2007). Coefficients were calculated for each OP population by using the T, P and fO_2 parameters that were determined through

MELTS simulations, as described in Section 3.6.5. The chosen parameters therefore define a physical environment that is consistent with the range of crystallization conditions and the depths of magma storage recognized for the Etnean plumbing system (see Section 3.6.5 for details).

Anisotropy-corrected diffusivity along the direction of the profile (D*trav*) was obtained taking into account how the compositional traverses were oriented with respect to the olivine crystallographic a, b and c axes (respectively coinciding with the optical indicatrix axes X, Y and Z measured by conoscopic observations under a polarizing optical microscope equipped with a Zeiss 4 axis universal stage) to further improve the accuracy and precision on time calculations (cf. Costa and Chakraborty, 2004; Shea et al., 2015). After application of all the correction criteria (i.e. influence of sectioning, diffusion anisotropy, crystal morphology), the model replicates diffusion times with a high degree of precision, although the number crystals suitable for calculation is considerably reduced (i.e., 22 olivine crystals). Uncertainties are mainly related to the temperature and oxygen fugacity determination. A temperature uncertainty of ±10°C yields errors of 2.8 days (2σ) on the timescale estimates; fO_2 variation of one order magnitude produces errors of ca. 10 days (2σ). Conversely, the pressure dependence is small, with time oscillations of ca. 0.6 years for pressure changes of 10 MPa, at constant temperature and fO_2.

As mentioned in the chapter *3.6.5*, the chemical records preserved in olivine cores of the K-trachybasalts erupted at Mt. Etna are evidence of at least five compositionally-distinct magmatic environments, where crystals grew close to equilibrium. Indeed, the occurrence of compositional plateaux at the crystal cores implies an early growth stage in

a host magma under unperturbed chemical and physical conditions. Later, at the rims, crystals developed chemical gradients as a consequence of changed conditions. Awareness of the magmatic process causing these chemical gradients in olivines is crucial to set the initial composition before re-equilibration of the system through diffusion. In this regard, the development of normal zoning patterns at the olivine rims has been attributed to processes of interaction with a more evolved magma after emplacement at shallower crustal levels. Therefore, through the Fe-Mg diffusion model, we tried to estimate the timescales of crystal residence at the new magmatic conditions, after intrusion of the host melt to shallower levels (Fig. 31). Reverse Fo zoning at the rim of the identified populations well reflects mixing resulting from mafic recharge, which produced chemical gradients at the crystal rim. Diffusion modeling of the reverse zoning patterns leads, then, to define timing of these mixing events between compositionally different magmatic end-members (Fig. 32).

Based on diffusion calculations, the spectrum of timescales estimates is fairly large, ranging from 21 to 560 days. However, the majority (~65 %) of the recorded timescales of intrusion and mixing are less than 5 months, suggesting very active behaviour of Mt. Etna during the investigated period. It is important to note that although the sequence and compositions of the magmatic environments recorded through the chemical zoning of olivine is similar, crystals from different eruptive episodes of the 2011-2013 period sometimes have revealed contrasting magma storage and recharge timescales. For instance, calculated average timescales for the long-lasting paroxysmal eruptions (i.e., the episodes of January 12, July 20, and April 10, 2011, and April 12, 2013) reveal that transfer of magma between different sections of the plumbing system

occurs over significantly longer times (4 to 17 months) than those estimated for short-lasting eruptions (21 to 52 days).

A more detailed picture of how long magma takes to migrate throughout distinct reservoirs is given taking into account independent time estimates for single episodes of transfer and mixing that have been identified through olivine zoning patterns. Calculated timescales are shown for different eruptive episodes of the 2011-2013 sequence in Figure 33.

The chemical zoning of the more primitive OP1 (Fo_{84}) olivines requires on average 30 days to re-equilibrate through diffusion to the composition Fo_{80-82} after migration and intrusion into the M2 reservoir, and ~37 days to re-equilibrate to the composition of the more evolved M4 (Fo_{76}) environment (Fig. 33). Reverse zoning recorded at the rim of OP2 (Fo_{80-82}) and OP3 (Fo_{78}) crystals is also consistent with the intrusion of the OP1 host melt (i.e. M1) into the M2 and M3 environments. Diffusion calculations on these zoning patterns indicate average timescales of ~170 days for mixing between the M1 and M2 magmas, whereas M1 and M3 interact and mix ~ 83 days before the eruption (Fig. 33).

OP2 (Fo_{80-82}) olivines record processes of migration from the environment M2 into the M3, M4 and M5 reservoirs. Intrusion into M3 and M5 is estimated to happen in 52-120 days, whereas timescales of transfer and storage into the magma M4 is generally much longer, ranging from 229 to 237 days (Fig. 33).

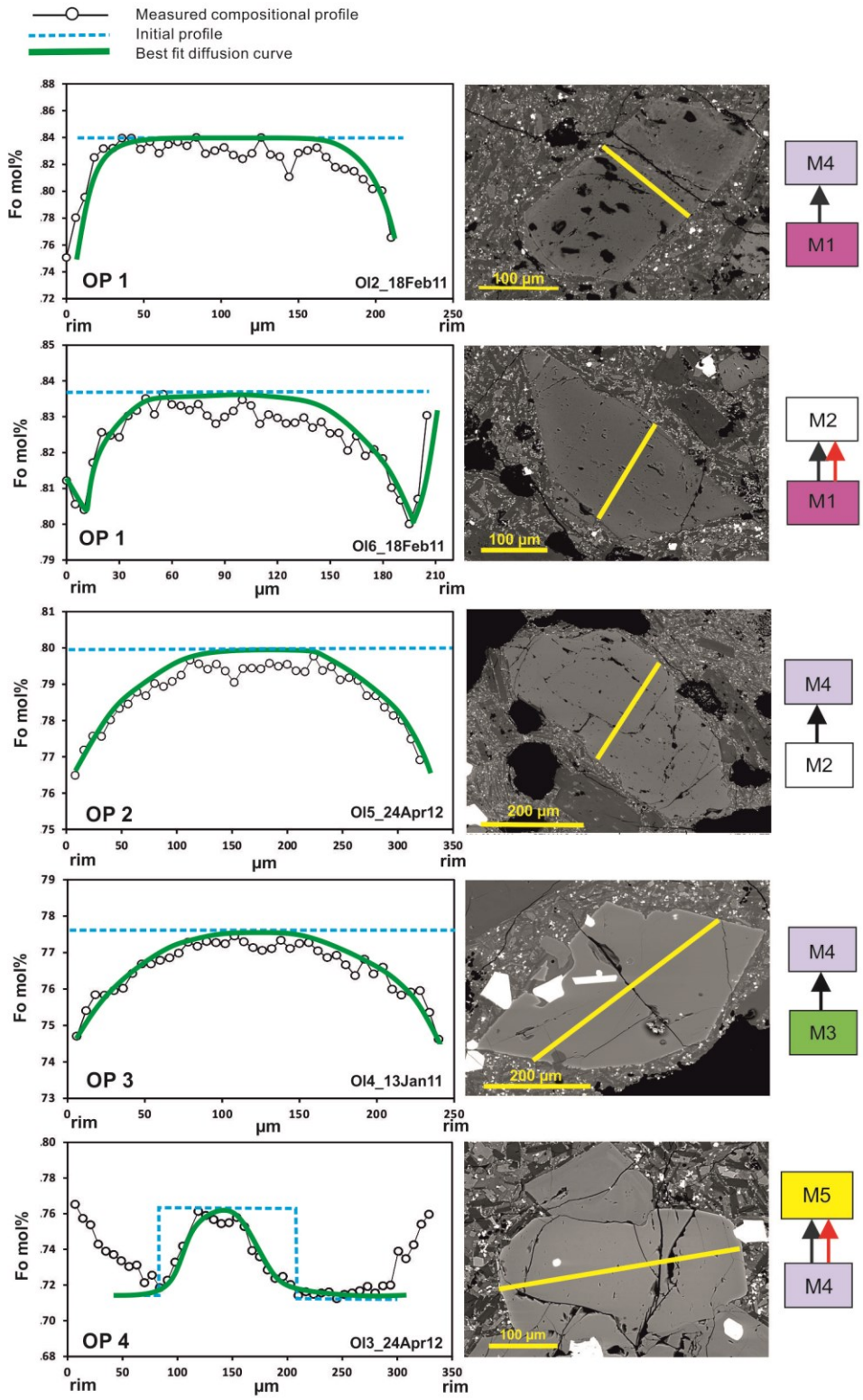

Figure 31. *Rim-to-rim compositional profiles and Fe-Mg diffusion modeling of representative olivine crystal characterized by normal zoning patterns. Light blue dashed lines indicate the initial concentration profile of the crystal, whereas the green lines represent the best-fit diffusion curves for the observed zoning profile. On the left it is shows the type of connection between distinct magmatic environments (coloured boxes), as revealed by the olivine zoning. Boxes and arrows as in Figure.26 and 27.*

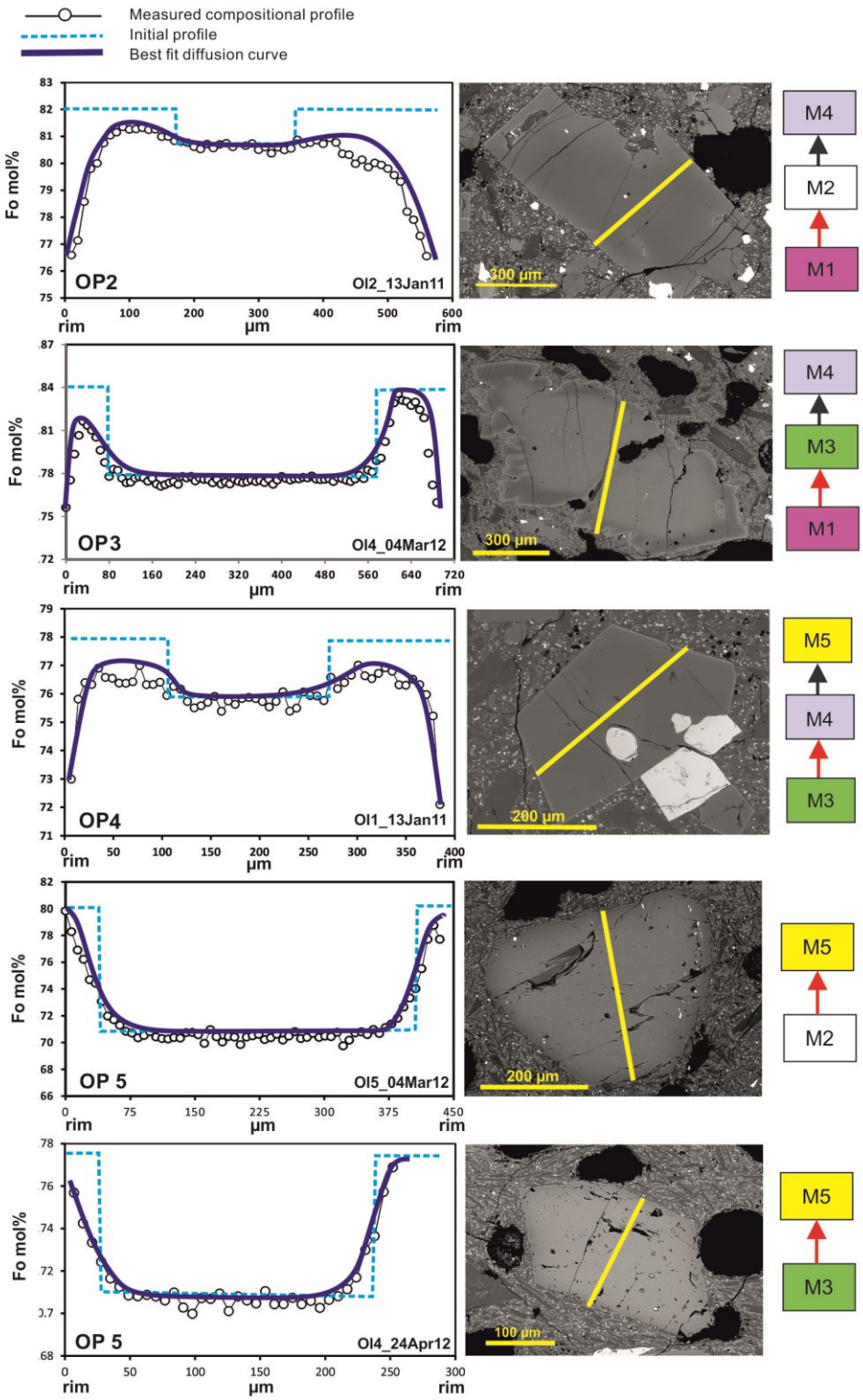

Figure 32. *Rim-to- rim compositional profiles and Fe-Mg diffusion modeling for representative olivine crystal characterized by reverse zoning at the rim. Light blue dashed lines indicate the initial concentration profile of the crystal, whereas the dark blue lines represent the best-fit diffusion curves for the observed zoning profile. On the left it is shown the type of connection between magmatic environments (coloured boxes), as revealed by the olivine zoning. Boxes and arrows as in Figure 26 and 27.*

The transfer and input of the M3 magma (Fo_{78}) into the environment M4 (Fo_{76}) is recorded by both the normal zoning patterns of OP3 olivines and the reverse zoning of OP4. Calculated timescales of re-equilibration of the OP3 zoning to the composition of the M4 environment are relatively rapid (109-119 days), and are rather comparable with timescales of mixing between M3 and M4 obtained by modelling the reverse zoning of OP4 (150-164 days; Fig. 33).

At shallow depths of the plumbing system, the injection of OP4 (Fo_{76}) crystals into the more evolved M5 (Fo_{70-72}) environment occurs over a wide range of timescales, from 53 to 560 days. However, longer timescales have been calculated for one single crystal erupted during the episode of July 20, 2011 (Fig. 33). Diffusion modelling calculations on the reverse zoning of OP5 (Fo_{70-72}) olivines also provide very variable timescales of mixing between the M4 and M5 end-member during the 2011-2013 eruption sequence. In particular, crystals erupted during the episodes of April 24, 2012 and April 18, 2013 record shallow mixing that occurred 3-6 weeks before the eruptions, whereas longer timescales of 5-6 months have been calculated for other crystals found in the products emitted during the February 23, 2013 eruption (Fig. 33).

OP5 crystals from the March 04, 2012 sample reveal further episodes of recharge with more mafic M1 and M2 magmas that affected the shallower M5 reservoir. Timescales associated to these processes of mafic intrusion at low pressure (<40 MPa) occurred over timescales (252-117 days) longer than those calculated for other short-lasting eruptive episodes (~20-157 days, i.e. the paroxysms of April 18 and February 23, 2013). This may indicate that intrusion of primitive magmas into the environment M5 before the eruption of March 04, 2012 happens intermittently, by recharge of minor

magma pulses that begins several months before the eruption, becoming more frequent and voluminous only shortly before the paroxysm.

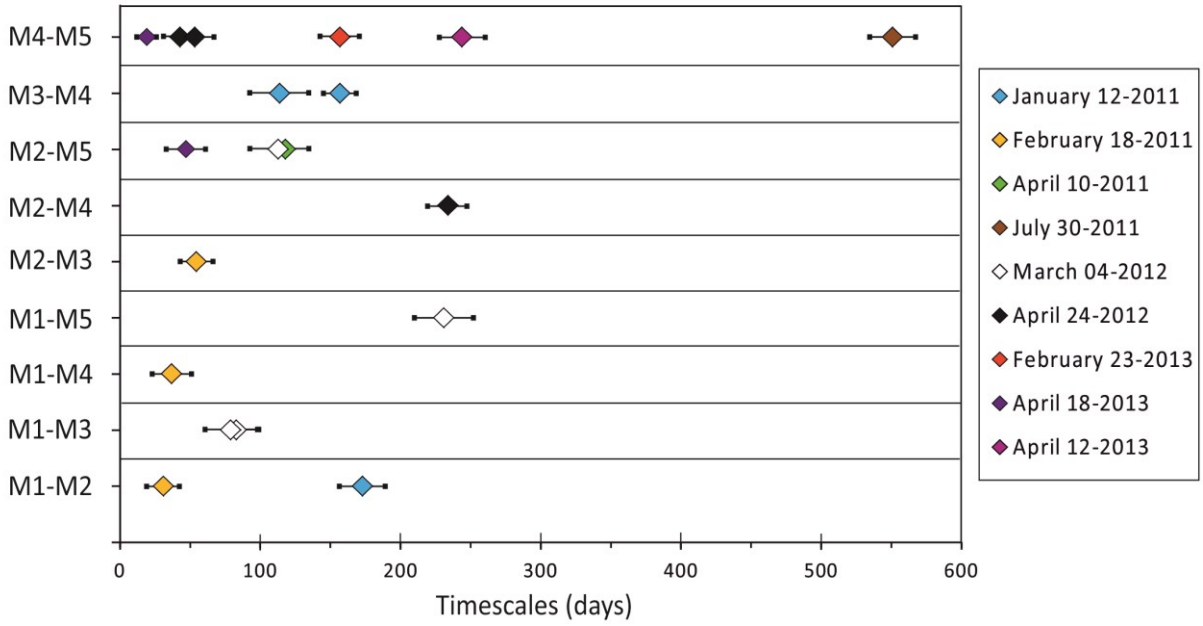

Figura 33. *Timescales of magma transfer and mixing throughout distinct reservoirs (left side) calculated for different eruptions between 2011 and 2013 throught Fe-Mg diffusion modeling in olivine crystals.*

3.6.7 The origin of lithium chemical gradients in plagioclase crystals

The quantification of volcanic processes involved in the final stage of magma ascent during eruption, such as the rates of gas-rich magma ascent and vesiculation, is a hard task of the modern volcanology, because direct measurements are not possible. Rther, timescales of syn-eruptive processes are typically inferred from the characteristics of the products discharged during eruptions (e.g. Klug et al., 2002; Shea et al., 2010), or through experimental simulations (e.g. Austin-Erikson et al., 2008; Kremers et al., 2010; Cichy et al., 2011). A different, more direct method to quantify the rates of these processes involves investigation of diffusive processes of lights element, such as Li, Be and B, which in the past were used as indicators of the magmatic source or as tracers of subduction-related processes (e.g., Leeman and Sisson, 1996; Moriguti and Nakamura, 1998; Leeman et al., 2004). In particular, the last years have seen the proliferation of a number of studies involving the compositional variation of lithium in plagioclase for tracking process of volatile exsolution from magmas ascending to the surface (e.g. Berlo et al., 2004; Kent et al., 2007; Generau and Clarke, 2010; Generau et al., 2009; Charlier et al., 2012; Cabato et al., 2015). This is because the ascent of gas-rich magmas and their vesiculation upon eruption occurs at rates too fast to be traced by mineral-melt diffusion of major or other trace elements. The increasing interest in studying Li concentrations and its diffusive processes is based on the observations that lithium is extremely mobile and prefers the exsolved fluid phase relative to melt at low pressure (Webster et al., 1989). Richter et al. (2003) recognized that the diffusion of lithium between the melt and the gas phase is faster than H_2O. Moreover, Li diffusion rates in plagioclase are on the order of 10^{-11}-10^{-12} m^2*s^{-1} (Gilletti and Shanahan, 1997), which are several orders of magnitude

faster than NaSi-CaAl interdiffusion (Grove et al., 1984; Liu and Yund, 1992). This means that Li is able to record extremely fast volcanic processes, operating over timescales of hours or less (cf. Charlier et al., 2012). All these characteristics make, therefore, the investigation of lithium chemical gradients in plagioclase crystals particularly useful for the identification and quantification of syn-eruptive magma ascent and degassing processes that occurred shortly before, and even during paroxysmal eruptions of the 2011-2013 activity.

Plagioclase crystals from Mt. Etna paroxysms have shown overall trends of decreasing lithium concentrations from the crystal interior toward the edge, which cover distances of ~200-300 μm. Systematic shifts in the Li content with localized perturbations to higher values were also recognized within these spatial ranges.

Decreasing concentrations of lithium toward the edge of plagioclase crystals have been emphasized in previous studies on the eruptions at Mount St. Helens (e.g. Berlo et al., 2004; Kent et al., 2007), Montserrat (Generau and Clarke, 2010; Generau et al., 2009) and Nea Kameni, Santorini (Cabato et al., 2013). This behaviour has been generally interpreted as superimposition of the effect of mineral-melt partitioning and loss of Li from the melt due to preferential transport of Li into the gas phase during eruption. Bindeman et al. (1998) and Bindeman and Davis (2000) demonstrated that the plagioclase-melt partitioning coefficient for Li is quite independent of An content; this means that a plagioclase in equilibrium with the host melt should have the same Li concentration from core to rim. Moreover, the extremely rapid diffusion of lithium would have homogenised any Li concentration gradients to create a flat profile within plagioclase, unless arrested by sudden cooling of magma after emission (Cabato et al.,

2013). In contrast, the addition or depletion of lithium in the melt will be reflected in positive or negative trends that deviate from those expected for diffusive equilibrium. The general rim-ward declines of Li in plagioclase imply, therefore, significant diffusive disequilibrium between Li and An during the final stage of crystal growth. This behaviour may have been caused by two different processes: a) loss of Li from the melt due to volatile exsolution, or b) intrusion of the crystal into a Li-poor magma volume. As mentioned in the previous chapters of this study, processes of low-pressure gas loss are common at Mt. Etna, which discharge large amounts of mantle-derived gases during its eruptions, but also continuously during its period of rest from both the summit craters and the volcano flanks (Allard et al., 1991; 1997; Aiuppa et al., 2002; 2007; Shinohara et al., 2008). Magma ascent and degassing paths for past eruptions of Mt. Etna have been well tracked by several melt inclusion studies (Metrich and Rutherford, 1998; Spilliart et al., 2006a; Metrich et al., 2004), but no Li-poor magma batches stored at low pressure have been detected before. Because lithium is easily released from the melt through degassing, the decreasing concentration of Li at the rim of the 2011-2013 plagioclase crystals is more consistent with gas separation during magma ascent and depletion of Li from the crystal due to preferential, rapid transport of Li into the fluid phase (Generau and Clarke, 2010; Generau et al., 2009).

In contrast with this interpretation, the occurrence of Li enrichments localized at regular intervals within the plagioclase rims require an increase of the Li abundance in the melt. Charlier et al. (2012) observed excess of lithium toward the margin of plagioclase crystals from the products of the Oruanui eruption (Taupo, New Zealand), and interpreted such changes as a consequence of changing Li partitioning behaviour due to preferential

exsolution of chlorine from the system during decompression. These authors argued that when a significant amount of chlorine is removed from a melt at subcritical fluid conditions, this has an important effect on partitioning of Li that forms hydroxides LiOH (Charlier et al., 2012 and references therein). This process would make Li far less compatible, increasing its chemical activity in the melt, and thus providing the driving force for Li diffusion back into plagioclase crystals. A similar process could also occur at Mt. Etna, where the high explosivity is determined by the high volatile richness of its magmas (>4 wt.%; Allard et al., 1997; Metrich et al., 2004; Spilliaert et al., 2006b). Data from melt inclusions entrapped in primitive olivine from Mt. Etna eruption of the last decades revealed concentrations of chlorine between 0.13 and 0.18 wt.%, which tend to increase (up to 0.26 wt.%) as the melt becomes more evolved.. These values are far higher than those estimated for chlorine concentrations at Taupo volcano (c.f. Charlier et al., 2012). According to Spilliaert et al. (2006b), chlorine exsolution begins at a pressure of ~100MPa, but becomes important only during magma degassing at very shallow depth (~10MPa). This behaviour strongly depends on the dynamics of magma ascent and, therefore, on kinetic effects; indeed, extensive magma vesiculation and fragmentation during the most energetic fountaining phases enhances Cl release from the melt (Spilliaert et al., 2006b). This assumption is also supported by decompression experiments on volatile-rich rhyolitic melt (cf., Gardner et al., 2006), demonstrating that the amount of Cl retained in the melt depends on the size of pumice clasts, and therefore on the degree of magma fragmentation. Despite similar effects that may also occur in basalts in which Cl diffusion would be faster, extensive extraction of chlorine with consequent repartitioning of Li back into the melt, would result in an increase of Li at the plagioclase rim. This

process, therefore, cannot account for the observed Li increases that are superimposed on a dominant trend of decreasing lithium contents. Rather, localized lithium enrichments along the plagioclase rims could likely reflect transient dynamic processes associated with gas migration from deep portions of the Mt. Etna plumbing system. Evidences that volatile–rich Etnean magmas can exsolve a gas phase at high pressure (higher than 250 MPa) are confirmed by numerous data on primitive glass inclusions in olivines (e.g. Metrich et al., 2004). In this regard, several authors have attributed the increasing explosivity of Mt. Etna in the last decades to the ascent and degassing of unusually volatile-rich magma batches rising up from deep reservoirs (e.g. Aiuppa et al., 2007; Nicotra and Viccaro 2012a; Ferlito et al., 2014). Based on these observations, one of the most plausible hypotheses for the enrichments in Li is that Li-bearing gases released from the deep levels of the plumbing system systematically rose up and accumulate in shallow reservoirs, where they partially re-equilibrate with the melt during its storage, and thus lead to increase the Li content of the melt. Processes of gas flushing were previously invoked to explain the significant enrichment of lithium in melt inclusions from Mount St. Helens samples (e.g., Blundy et al., 2008; Kent et al., 2007; Berlo et al., 2004). In these studies, the Li enrichment is supposed to have been caused by transfer of a lithium-rich gas phase from deeper parts of the Mount St. Helens plumbing system; subsequently, the separation of the gas phase at the top of the magma chamber would have led to the formation of a Li-rich brine (Blundy et al., 2008; Kent et al., 2007). Berlo et al. (2004) also argued that the longer a magma body is stored at low pressures, the higher the amount of lithium in the melt. In spite of a lack of published data about lithium distribution in melt inclusions to confirm the ascent of Li-rich gas phases at Mt. Etna, the

occurrence of multiple peaks at higher Li concentration is consistent with repeated cycles of gas flushing from depth, which are systematically recorded by plagioclase during its growth. Gas bubbles rising and accumulating in shallow reservoirs may cause pressurization and, therefore, are thought to act as a recurrent trigger mechanism for explosive events at basaltic volcanoes (Allard et al., 2005, 2010; Aiuppa et al., 2007, 2010b; Pichavant et al., 2013).

3.6.7.1. Lithium diffusion and timescales of magma degassing

As mentioned above, the diffusivity of Li in plagioclase is very high, which means that the gradients in Li concentrations would equilibrate within hours, minutes or even less, depending on the magmatic temperature of the system under investigation (Gilletti and Shanahan, 1997). This also implies that the process of degassing responsible for Li disequilibrium preserved in the rims of plagioclase crystals is inevitably a short-lived process, occurring shortly before or even during the fountaining activity. Modelling the diffusion of lithium between the plagioclase and its host melt provides, therefore, the opportunity to evaluate the timing of syn-eruptive decompression-driven degassing of magmas associated with the paroxysmal activity between the 2011 and 2013 AD at Mt. Etna.

In order to evaluate these timescales, each lithium profile was modeled using a one-dimensional model of diffusion through a layer (i.e. the crystal edge) placed between two semi-infinite bodies (Fig. 34), following an approach similar to that of Morgan et al. (2004). The adopted approach allows the derivation of analytical solutions for the diffusion equation because the Li diffusion coefficients in plagioclase are independent

from An. The initial lithium distribution between the plagioclase and the melt was described as a step-function at the crystal edge, and it was assumed a uniform initial concentration in the crystal and constant concentration at the crystal-melt interface. Once the initial and boundary conditions have been defined, the evolution through time of the Li concentration within the crystal was modelled following the equation:

$$C_{x,t} = C_0/2 \, [\, 1 + \mathrm{erf}\,(x / 2\,(D\,t)^{0.5}) \,]$$

where $C_{x,t}$ represents the composition at the maximum extent of diffusion at the distance *x* from the crystal margin, D is the diffusion coefficient for Li in plagioclase, and t is the time elapsed since diffusion begins. The diffusion of Li within the Etnean plagioclases was modelled with a composition-independent diffusion coefficient D of 3.72×10^{-10} m^2/s. Coefficients were calculated at 1100 °C by using the Arrhenius parameters (i.e., the pre-exponential factor D_0, and the activation energy Q) provided by Gilletti and Shanahan (1997) for Li diffusivity in plagioclase of anorthitic composition.

Diffusion modelling calculations yield timescales of syneruptive magma degassing and ascent between ~~5~~ 20 and ~~14~~ 30 seconds, with the shorter timescales calculated for the episodes of February 23 and April 18, 2013. Because the calculated D is composition-independent, uncertainties on time determinations are mainly dependent on temperature, in a way that T changes of ±10° C result in time variations of ±4 seconds. Moreover, the uncertainty related to the calculation of D_0 and Q for Li diffusivity at 1100° (see Giletti and Shanahan, 1997) may also result in 10-15 second overestimates on the final timescales. These time estimates offer also the opportunity to determine the final rates of magma degassing and ascent associated with the paroxysmal eruptions at Mt. Etna. Determinations of the ascent rate upon eruption require, however, some constraints on the

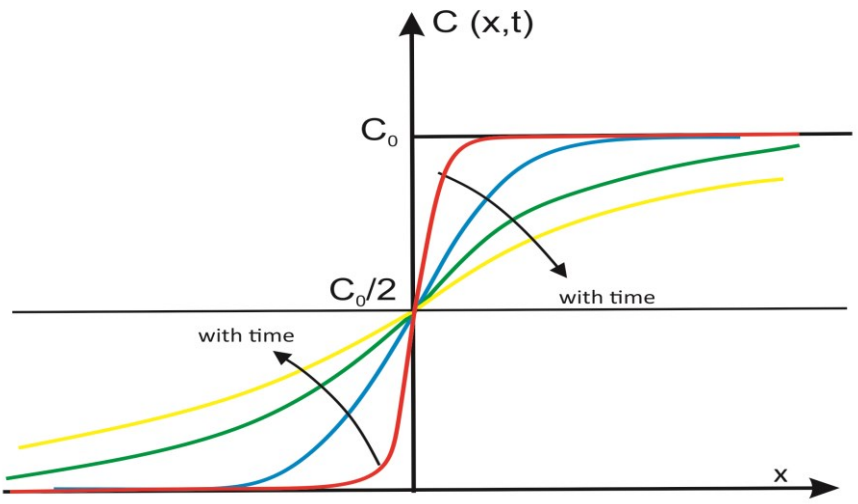

Figura 34. *Example of elemental diffusion in the case of semi-infinite uniform release. Physically, the element diffuses in the melt through the crystal edge; therefore, its concentration in the crystal decrease with time, while in the melt it gradually increases. Graphically, the initial concentration profile takes the aspect of a step that is gradually eroded.*

pressure at which Li disequilibrium begins and, therefore, the pressure at which the magma was stored before emission. In this regard, the compositional and textural characteristics of plagioclase crystals from the 2011-2013 activity at Mt. Etna highlighted common late-stage histories of crystallization in a shallow storage zone. This magma reservoir was inferred to be located below the summit area at 1-2 km a.s.l., corresponding to a pressure of ~40 MPa (cf. Patanè et al., 2013, and references therein). This indicates that just prior to the eruption, magmas were likely stored at an average depth of 1.8 km beneath the volcano summit, and later underwent instantaneous decompression through the conduit. Assuming that the Li diffusion begins at this depth, our timescales imply rates of magma ascent upon eruption between 50 and 75 m/s. These rates inferred from Li profiles are higher compared to those estimated for other extremely explosive eruptions

either at basaltic or silicic volcanoes; for these, calculated ascent rates are up to 65 m/s (i.e., the 1980 eruption of Mt. Saint Helens; Humphreys et al., 2008). These time differences may be attributed to the large uncertainty on the calculation of Li diffusion coefficients for plagioclase of Mt. Etna. Indeed, the absence of experimentally-calibrated Li diffusion coefficients in plagioclase crystals at magmatic temperatures >850 °C has precluded a proper application of the Li diffusion modelling in plagioclases from Mt. Etna, where magmatic temperatures are ~1100 °C at intratelluric conditions (cf. Pompilio et al., 1998). Temperature variations of ~200°C for calculation of D, as reported from Gilletti and Shanahan (1997), results in a higher diffusion rate of Li and leads to timescales of magma ascent about 10-15 seconds faster than those expected for paroxysmal eruptions.

3.6.8 General picture of Mt. Etna dynamics beneath the NSEC

The picture drawn from integration of whole rock data with the compositional, textural and temporal information preserved in crystal is that of an extremely dynamic plumbing system, where processes of mafic recharge and migration of CO_2-rich gases, continuously affect the evolutionary dynamics of magmas during the 2011-2013 paroxysmal activity.

The compositional dataset presented in this study suggests that magmas feeding the recent activity at Mt. Etna preserve a signature very close to those of magmas emitted during the explosive episodes of 2007, although they display differences mainly dependent on the evolutionary degree. A more detailed investigation of the geochemical characteristics of Etnean magmas based on *in-situ* trace element analyses on plagioclase

revealed the presence of two contrasting parental magmas, with rather different Sr/Ba concentrations, involved during the recent activity of the volcano. Only crystals from a few eruptive episodes, especially of the first half of 2011 (from February to July), have low-Sr/Ba contents, suggesting that during these episodes the plumbing system may have intercepted low-Sr magma batches underlying the volcano, probably inherited from past pre-1971 eruptions. This inference is consistent with the observation, already documented by Viccaro et al. (2016), that a new geochemically distinct magma (at higher Sr concentration) has progressively replaced the resident one during the last decades. Time constraints from Sr diffusion in plagioclase also reveal maximum times of magma residence shorter than 31 years, as an indication that the plumbing system has been able to supply poorly differentiated magmas over relatively short timescales.

Textural and compositional heterogeneities of plagioclase and olivine crystals highlighted the presence of magmas at distinct differentiation degrees, ascending from several unconnected pathways, which finally merge at shallow depth prior to the eruption. The transfer of primitive magmas across the Mt Etna plumbing system occurred preferentially stepwise through multiple episodes of intrusion and residence in distinct levels of the plumbing system. The most basic magma environment is located at a depth of ~18-20 km below the summit. From this deep reservoir, magma generally moved along a dominant pathways, intercepting the M2 (12-14 km) and/or M3 (8-10 km), M4 (5-6 km) and M5 (1-2 km) reservoirs, and experienced both crystal and fluid fractionation during its ascent. Timescales of transfer and storage across these distinct sections of the plumbing system vary from ~1 to ~18 months and are generally shorter for paroxysmal episodes showing a rapid intensification of the eruptive phenomena. In the case of some

specific eruptions (e.g. during the eruption of February 18, 2011 and March 4, 2012), the ascent of more primitive magma did not follow the dominant migration route, but it rose up along a preferential route that facilitated the transfer of primitive magma directly into the shallower and evolved M5 reservoir, bypassing the intermediate storage zones. Timescales associated with this process of migration from M1 to M5 for the episode of March 04 2012 are, however, rather long (~7-10 months) and may indicate that the transfer of primitive magma at shallow depth began in minor pulses several months before the eruption, and continued until the system is overpressurized. Intrusion and mixing by more basic magmas into the shallowest reservoir occurred within 5 months before eruption for all the episodes of the 2011-2013 sequence.

Magmatic processes that occurred within the system residing at shallow depth beneath NSEC have proved to be closely related to the temporal evolution of paroxysmal phenomena. For instance, episodic recharge of more basic magma into the shallowest part of the magmatic system drives the development of long-lasting paroxysms, leading to a gradual increase of the eruption intensity up to the paroxysmal phase. On the contrary, transient gas bursts exert a primary control on the development of short-lasting paroxysms characterized by fast transition to lava fountaining. Cycles of gas-flushing rising up from deeper sections of the plumbing system and accumulating at shallow depths have been traced through the evidence of Li enrichment in plagioclase crystals. This gas flushing may have caused overpressurization of the system, leading to sudden awakening of activity and its evolution to lava fountains. The lithium concentration gradients also provided a marker for the final stage of magma ascent and degassing during the paroxysmal phase, indicating extremely fast ascent rate of 50-75 m/s.

4.0. UNDERSTANDING THE INFLUENCE OF CARBON DIOXIDE ON MINERAL STABILITY AND MELT CHEMISTRY DURING MAGMA STORAGE AT INTERMEDIATE AND SHALLOW CRUSTAL LEVELS

4.1. Introduction

As mentioned in the previous chapters, processes of CO_2 flushing from magmas exsolving gas at depth have been found to play a major role in producing high-energy eruptions at many basaltic systems, such as Etna and Stromboli (Aiuppa et al., 2010a; 2010b; Allard 2010; Pichavant at al., 2013; Ferlito et al., 2014). In this context, Mt. Etna represents one of the most intriguing cases. The complex plumbing system of Mt. Etna is persistently fed by primitive, volatile-rich magmas that mix with basic, degassed magmas stored at shallow levels (Armienti et al.; 2013; Corsaro et al., 2013; Mollo et al., 2015; Viccaro et al., 2010, 2015; Nicotra and Viccaro, 2012a). This means that a major part of the crystallization occurs in regions of the plumbing system where CO_2 is already exsolved, but in which H_2O activity activities can change very abruptly as a result of local fluxes of CO_2–rich fluids in magma reservoirs (cf. Aiuppa et al. 2010b; Patanè et al., 2013).

The concentrations of CO_2 in Mt. Etna K-trachybasalts are prominent (>1.5 wt.%; Allard, 1991). Moreover, on average, from both its summit area and the volcano flanks, Mt. Etna discharges more CO_2 than any other volcano elsewhere (about 25 Mt/year Gerlach, 1991), which represents about 10-15 % of the total estimated volcanic CO_2 emissions in the world (cf. Gerlach, 1991; D'Alessandro et al., 1997; Mörner and Etiope,

2002). In such a magmatic system that is particularly rich in CO_2, the proportion of CO_2 in the melt, in addition to H_2O, may play a key role in chemical changes of the melt and on the mineral stability, which in turn affects crystal textures. To provide a proper interpretation of natural samples from the combination of petrological, textural and microanalytical data, it is therefore crucial to address compositional and/or textural changes of magmatic crystals as a response to variations in the proportion of CO_2 in the magma.

In this section, we present crystallization experiments on H_2O+CO_2-bearing K-trachybasaltic melts from the recent activity of Mt. Etna, with the aim to test if flushing of CO_2 in variable proportions may produce variations of mineral stability and glass chemistry. The experimental strategy applied in this study involves at first the crystallization of a natural melt equilibrated with pure H_2O-fluid at elevated pressure (300 MPa) below the H_2O saturation depth; this melt is initially exposed to thermal cycling to induce crystal nucleation and growth. The partially-crystallized magma obtained from this first experiment was, then, used to simulate the CO_2-flushing of Etnean magmas during their storage in the intermediate and shallow plumbing system through two sets of flushing experiments conducted at 300 and 100 MPa with a fluid composed of H_2O and CO_2.

4.2 Experimental methods

4.2.1 Anhydrous glass synthesis

A natural lava sample from the March 4, 2012 paroxysmal eruption at Mt. Etna was used as starting material. This sample is a porphyritic basalt (SiO_2 47.01 wt.%) that is among the most basic materials collected at Mt. Etna during the post-2011 eruptive period

(see Table 6 for the major oxides composition of the chosen sample). This basalt contains 25 vol.% of phenocrysts in the following proportions: 40% clinopyroxene, 30% plagioclase, 15% olivine and 10% titaniferous magnetite. Phenocrysts are generally dispersed in a hyalopylitic groundmass.

The experimental starting material was prepared by crushing the natural lava to a grain size <5 mm. To further improve the homogeneity, an agate mortar was used to produce more fine-grained powder. The powders were melted for 3h in a Pt-crucible placed in a furnace at 1600 °C and 1 atm. Then, the melt was quickly quenched to glass by quenching it directly on a brass plate. To improve the homogeneity of the mixture, the glass was grinded again in an agate mortar and melted for 2h at the same conditions. The major element composition and homogeneity of the final quenched basaltic anhydrous glass were examined by Cameca SX 100 electron microprobe at the Institute for Mineralogy of the University of Hannover, Germany. The composition of this anhydrous glass is reported in Table 6. The glass was crushed and divided in two fractions with a diameter of 200 μm and 500 μm. Before loading into experimental capsules, the two grain-size powders were mixed in a volume ratio of 1:1 to minimize the free volume between grains and hence, to reduce the incorporation of atmospheric water or nitrogen into the charge (Vetere et al., 2015 and reference therein). This procedure ensures a more uniform distribution of fluids and avoids the incorporation of absorbed water in the sample container.

.

Table 6. *Bulk rock composition (wt.% anhydrous)s of the natural starting material (sample 04Mar12) determined by Viccaro et al. (2015) and average major oxide compositions of the experimental dry glasses (wt.%). Errors represent one standard deviation for six electron microprobe analyses.*

	SiO_2	TiO_2	Al_2O_3	FeO_{tot}	MnO	MgO	CaO	Na_2O	K_2O
04Mar12	47.01	2.02	16.28	12.09	0.22	5.61	11.00	3.33	2.00
Dry glass	47.37 ±0.42	1.83 ±0.03	16.55 ±0.34	9.86 ±0.34	0.13 ±0.03	5.42 ±0.10	10.60 ±0.23	3.34 ±0.69	1.90 ±0.04

4.2.2 Sample hydration and preparation of capsules for experiments

The glass powder prepared at 1 atm was first used to synthesize a hydrous glass containing 1 wt.% H_2O. A 40 mm long $Au_{80}Pd_{20}$-capsule, with a diameter of 5.0-5.4 mm, was used to perform the experiments. After annealing at 950°C, the capsule was prepared by loading ≈ 1.0 g of glass powder and 1 wt.% of deionized water for the synthesis of the hydrous glass. The amount of added water was calculated to ensure that melts were volatile undersaturated at the initial experimental conditions (300 MPa, 1080°C). The choice to hydrate the sample with only 1 wt.% of water is based on the necessity to make sure the crystallization of plagioclase at high-pressure conditions. This choice is in agreement with the application of the hygrometer of Putirka (2008) on oscillatory zoning plagioclase cores from sample 04Mar12, which suggests early crystallization of plagioclase at a depth of ~290 MPa, temperature of 1100 °C, and with a water content between 0.5 and 1.1 wt.%.

The capsule was filled in several steps to achieve homogenous initial distribution of water and glass. Water was added step by step to dry glass powders and the charge was compressed after each addition of water by using a steel piston. Finally, capsules were

welded and checked for leakage of water by annealing at 110°C for about 2 hours. No water loss was detected by re-weighing the capsule.

Syntheses of water-bearing glasses were, finally, performed at 1250°C and 300 MPa for about 24h in a vertically operating Internally Heated Pressure Vessel (IHPV). These glasses were then used to synthesize a partially crystallized water-bearing sample to be used as starting material for CO_2-flushing experiments.

4.2.3 Crystallization and flushing experiments in Internally Heated Pressure Vessel

To describe accurately textures obtained from the reaction of an assemblage (melt + mineral) in disequilibrium with fluids (simulating the flushing with a fluid composed by H_2O and CO_2), an experimental approach was applied to obtain particularly large crystals in the synthesis of the melt + mineral assemblage. The hydrous glass was melted to superliquidus conditions at 1250°C and 300 MPa in IHPV. Subsequently, nucleation and crystallization processes were induced by lowering the temperature from liquidus conditions to 1080°C, with a cooling rate of 20°C/min. Finally, 25 thermal cycles of two hours each, with a temperature oscillating between 1060 and 1100 °C, were applied. The pressure was kept constant at 300 MPa by automatic compensation. A LabView program was used to control temperature cycling and to record the measured temperature every minute. Before quenching, the temperature was set to the mean temperature (1080°C) for 20 minutes.

Crystallization under oscillating temperatures was expected to enhance the growth of crystals (cf. Hintzmann and Muller-Vogt, 1969; Mills et al., 2011; Mills and Glazner, 2013; Erdmann and Koepke, 2016) and indeed the product obtained after the synthesis

shows crystals of clinopyroxene and plagioclase larger than 1 mm (Fig. 35). This product, labeled S_0, was used as starting material for the subsequent experiments in which a H_2O+CO_2 fluid mixture was added (Fig. 35).

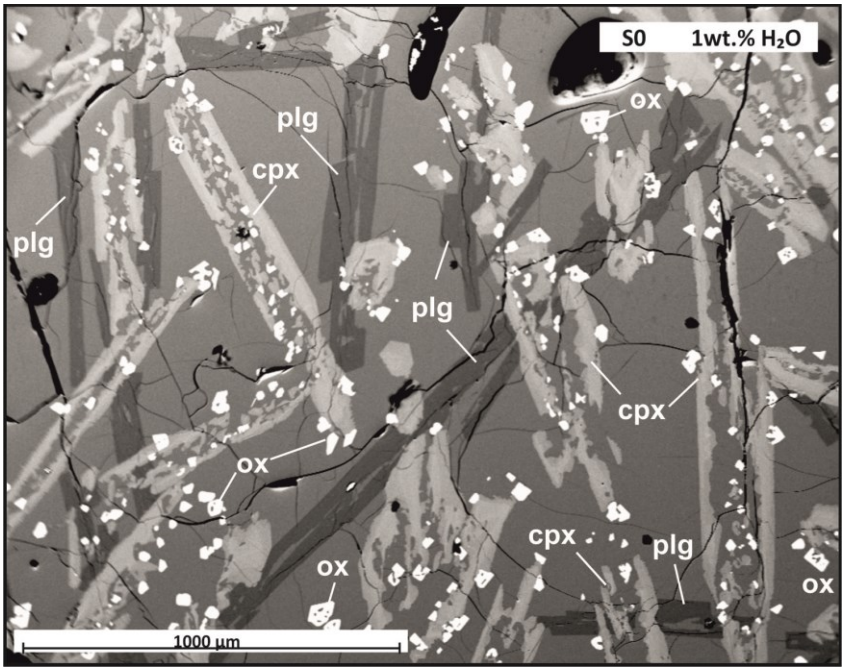

Figura 35. *BSE image of sample S_0 that has been used as starting material for experiments of flushing with water and carbon dioxide. S_0 has been crystallized from a melt hydrated with 1 wt.% of water. Experiment performed with thermal cycling at 1080°±20°C and pressure of 300 MPa. Cpx=clinopyroxene; plg=plagioclase; ox=opaque oxides.*

Two set of experiments were performed in IHPV at constant temperature of 1080 °C and pressures of 300 MPa and 100 MPa to simulate CO_2-flushing at different levels of the plumbing system. The P-T conditions selected for the H_2O+CO_2-bearing experiments are those of the lower-intermediate plumbing system of Mt. Etna, where the presence of

major magma storage zones at depths of 12-9 km and 6-3 km, together with a small reservoir at 1-2 km beneath the summit craters, have been inferred by geophysical studies (Aloisi et al. 2002; Patanè et al. 2006, 2013; Bonaccorso et al., 2011). However, it must be noted that the crystallization process was performed at temperatures of 1080 °C that are slightly lower than those generally acknowledged for Etnean K-trachybasaltic magmas at intratelluric condition. This choice was done in order to ensure crystallization of all mineral phases observed in the natural samples and to further increase the crystal mean size.

In order to perform the flushing experiments, slices (14-23 mg) of the starting materials S_0 were encapsulated in Au80Pd20-tubes together with deionized water and silver oxalate ($Ag_2C_2O_4$), which was used as source of CO_2. Water and silver oxalate were loaded into capsules in different proportions to establish different mole fractions of CO_2 in the fluid phase before the beginning of each experiment (XCO_2^{fl} from 0.2 to 0.9; Table 7). Capsules were weighted after loading of each component and after welding; they were finally checked for leakage by annealing in an oven for at least 1h at 110°C. For each set of experiments, three capsules were run simultaneously. The duration of each run was about 24h.

The IHPV apparatus and the rapid quench technique used in this study are described in detail by Berndt et al. (2002). The temperature is measured by four unsheathed S-type (Pt-Pt90Rh10) thermocouples, with an accuracy of ±10°C, and an Eurotherm software was used to record the measured temperature along the whole experimental run time. Argon is the pressurizing medium and the pressure is monitored by digital pressure transducers with an uncertainty of about 1 MPa. Variation of pressure during experiments

Table 7. *Experimental conditions, composition of the fluid phase dissolved and exsolved after runs and post run products. All runs at 1080°C.*

Run	Type	P (MPa)	log fO_2	Initial fluid fraction	Initial fluid compositions (*wt.%*)		Fluids in the melt (*wt.%*)*		Exsolved fluids (*wt.%*)*		Final fluid mole fraction	Post-run products
				$XCO_2^{fl}{}_{In}$	H_2O	CO_2	H_2O	CO_2	H_2O	CO_2	$XCO_2^{fl}{}_{fi}$	
300_S2	H_2O+CO_2	300	-6.62	0.4	3.9	7.3	2.63	0.22	1.27	7.08	0.69	Gl+Cpx+Ox
300_S3	H_2O+CO_2	300	-6.79	0.7	3.5	24.9	1.72	0.26	1.78	24.64	0.85	Gl+Cpx+Ox
300_S4	H_2O+CO_2	300	-7.26	0.9	0.7	29.5	0.5	0.28	0.2	29.22	0.98	Gl+Cpx+Plg+Ox
100_S1	H_2O+CO_2	100	-7.01	0.2	4.9	3.8	2.39	0.03	2.51	3.77	0.38	Gl+Cpx
100_S2	H_2O+CO_2	100	-6.82	0.5	3.3	8.3	1.58	0.05	1.72	8.25	0.66	Gl+Cpx+Plg+Ox
100_S4	H_2O+CO_2	100	-6.04	0.9	0.7	28.8	0.39	0.09	0.31	28.7	0.97	Gl+Cpx+Plg+Ox

* *Composition calculated through MagmaSat software (Ghiorso and Gualda, 2015).*

was <5 MPa. Experiments were performed at the intrinsic hydrogen fugacity of the vessel. Under intrinsic conditions in the IHPV, the oxygen fugacity in capsules containing pure H_2O (i.e. sample S_0) fluid was found to be close to the MnO–Mn_3O_4 or NNO + 3.7 buffer (Berndt et al. 2002). In charges containing a H_2O+CO_2 fluid mixture, the oxygen fugacity decreases as the amount of loaded CO_2 increases, chiefly due to the lowering of water activity, e.g., an increase in XCO_2 from 0 to 0.9 decreases the fO_2 by roughly two logarithmic units (e.g., Botcharnikov et al. 2008, 2005; Vetere et al., 2014). Hence, the redox conditions within capsules were determined on post-run products using the oxygen barometer of Ishibashi (2013), which is based on the spinel-melt equilibria (Table 7). The calculated logfO_2 varies between 10^{-6} to $10^{-7.3}$ bars, corresponding to ΔQFM + 3.5-2 (Table 7). At the end of each run, samples were quickly quenched isobarically by dropping the capsule down into the cold part of the vessel, in order to avoid any non-equilibrium quench effects (Berndt et al. 2002). Using this rapid quench device, estimated cooling rate was about 150°C/s.

4.3 Analytical methods

4.3.1 Karl-Fischer Titration measurements of H_2O content in initial hydrous glasses

Karl-Fischer titration (KFT) was adopted for the determination of the water concentrations in quenched initial glasses. Water is extracted by heating the sample up to temperatures of about 1300°C and the released water is measured by coulometric titration. The coulometer used in this study is a Mitsubishi CA100. The benefit of the KFT method is that only small amounts of glass are required to get reliable analyses. In this study,

about 50-100 mg of glass were required for a water content of 1 wt.%. However, the extraction of water in silicic melts with this technique is incomplete (Behrens, 1995). Typically, about 0.10 wt.% of non-extracted H_2O was found in samples containing initially more than 1.5 wt.% H_2O (Behrens 1995; Leschik et al., 2004), implying that the water contents obtained with KFT methods must be corrected for values of residual water content. As the water diffusivity is much faster in silica-poor melts than in silica-rich melts (Behrens et al., 2004), the extraction of water should be greatly enhanced in the less evolved basaltic melts under investigation. Hence, the 1.1 wt.% of H_2O measured with KFT for the 04Mar12 glasses can be assumed as representative of the real water content of the sample, and corrections for non-extracted water were not required.

4.3.2 Determination of sample fluid compositions after experiments

The mole fractions of H_2O and CO_2 in the fluid phase after experiments were calculated by mass balance using the initial amounts of loaded volatiles, rock powders and the estimated concentrations of volatiles retained in the melt after each experimental run (Table 7). The H_2O and CO_2 concentrations in the melt and the related composition of the exsolved gas phase were determined through the MagmaSat software based on the thermodynamic model of Ghiorso and Gualda (2015), which allows calculation of the saturation conditions for mixed H_2O-CO_2 fluids in natural silicate melts. In all the samples, the H_2O-CO_2 degassing behavior was modeled starting from the average composition of the run product glasses. Adopted P, T and fO_2 values are in accordance with the chosen experimental conditions as reported in Table 7. Results of the modeling indicate that the H_2O and CO_2 contents in the melts after each run are 2.6-0.5 wt.% H_2O and 0.2-0.3 wt.% CO_2 for experiments performed at 300 MPa, and 2.4-0.4 wt.% H_2O and

0.03-0.09 wt.% CO_2 at 100 MPa. Such concentrations are in the same range of those determined from melt inclusion analyses from other recent post-2001 eruptions of Mt. Etna (Métrich et al., 2004; Spilliaert at al., 2006a; Collins et al., 2009).

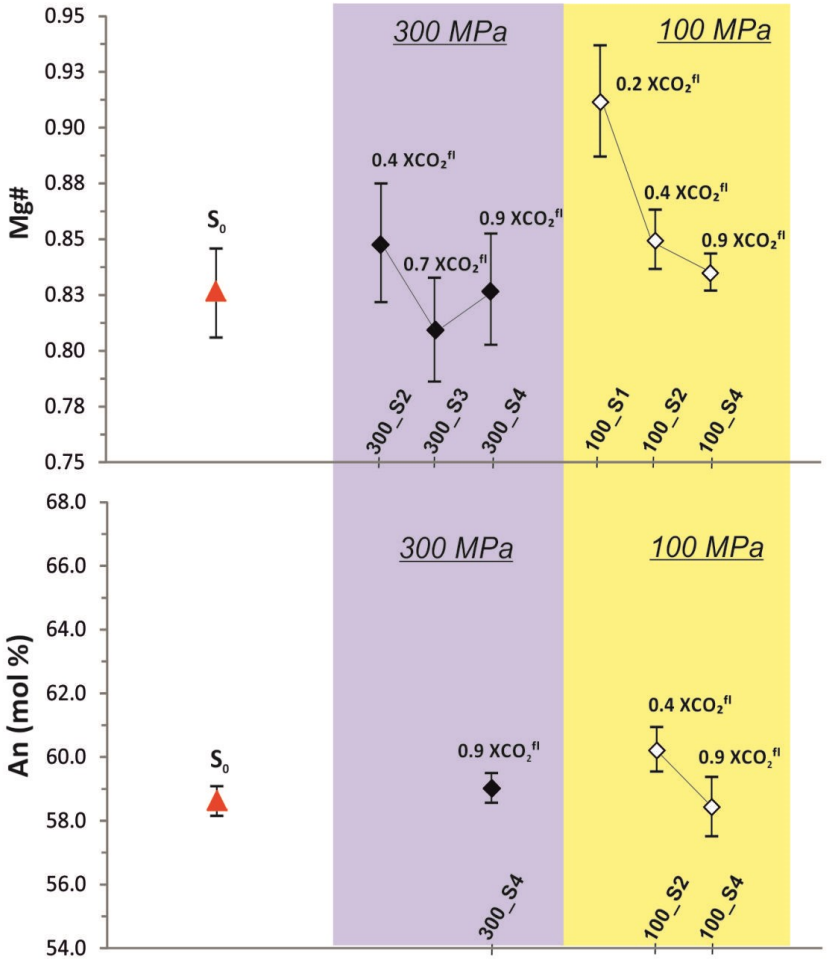

Figure 36. *Variation of the average Mg# of clinopyroxene and An (mol.%) of plagioclase crystals in the initial sample S_0 and for the products flushed at 100 and 300MPa using a fluid with distinct proportion of H_2O+CO_2. XCO_2^{fl} is the mole fraction of CO_2 in the fluid phase. Bars on data indicate the 2 sigma error.*

4.3.3 Electron Microprobe Analysis (EMPA)

Major element compositions of the starting glass and the experimental products, composed of minerals and glass, were analyzed by a Cameca SX-100 electron microprobe, using 15 kV as the acceleration voltage. Conditions of measurement during glass analyses were 4 nA beam current and 20 μm diameter of electron beam. Peak counting times vary from 4s for Na and K, to 8s for the other elements. Cameca standards were used for calibration. The analyses on minerals were conducted with a 15 nA beam current and a focused electron beam. Peak counting time was 5s for Na and K, and 10s for the other elements. The composition of the starting glass is an average of 6 analyses. Multiple point measurements were made for mineral phases and glasses of the experimental products to check the sample homogeneity and to reduce possible analytical errors. For some of the larger crystals (~1 mm size), core-to-rim profiles were measured through single grains to determine changes in chemical composition.

4.4 Experimental Results

4.4.1 Mineral assemblage and composition of the post-run hydrated products

The hydrated product resulting from crystallization at 300 MPa, which is indicated in this paper as sample S_0 (Fig. 35), consist of glass and a mineral assemblage primarily constituted by phenocrysts of plagioclase (~40 vol.% of the total assemblage) and clinopyroxene (~50 vol.%). Abundant and small (20-150 μm size) oxides, mainly titaniferous magnetite are also present in proportion of ~10 vol.% (Fig. 35). The glass compositions fall in the field of the basaltic trachyandesite (SiO_2 = 52-53 wt.%;

Na_2O+K_2O = 8.2-8.6 wt.%). As a whole, the observed mineral assemblage resembles that of the natural lava samples from Mt. Etna 2012 eruptions. The exception is the lack of olivine crystals at the chosen experimental conditions, which probably did not crystallized due to the too high oxidizing conditions. Clinopyroxene, the most abundant mineral phase with size from 200 μm to about ~1 mm, has diopsidic composition ($Wo_{47-50}En_{30-38}Fs_{14-21}$). Variations in Mg# are between 77% and 88% (Fig. 36). Clinopyroxene displays complex crystallization patterns that indicate an extensive dissolution/resorption and a subsequent regrowth of the crystal during the run. Plagioclase occurs in euhedral crystals up to 1 mm in size. Plagioclase crystals are labradoritic in composition ($An_{55-64;}$ Fig. 36) and oscillatory zoned, with very small oscillations in anorthite content between core and rim (~ΔAn 2%). This chemical zonation of plagioclase is, however, not evident under optical and BSE observations. It is worth noting that the average anorthite concentration of plagioclase in the experimental sample is significantly lower than the plagioclase compositions in natural products from Mt. Etna, which typically cover a wider compositional range from bytownite to labradorite, with subordinate rare anorthite crystals (Viccaro et al., 2010; 2016). Textural relations between minerals indicate that clinopyroxene and Fe-Ti oxides are the first crystallizing phases, whereas plagioclase crystallizes at a later stage.

4.4.2 Mineral assemblage and composition of the products after CO_2 flushing

In this section, we describe the textural and compositional characteristics of the sample S_0 after CO_2 flushing at distinct pressure conditions. Experimental results are

described below for increasing mole fraction of CO_2 in the fluid phase for the experiments at 300 and 100 MPa (Figs. 37 and 38).

At 300 MPa, experiments with water and carbon dioxide produced a mineral assemblage only composed of clinopyroxene and titaniferous magnetite in samples 300_S2 (0.4 XCO_2^{fl}; Fig. 37a-b) and 300_S3 (0.7 XCO_2^{fl}; Fig. 37c-d). Sample 300_S2 shows relicts of clinopyroxene ($Wo_{47-50}En_{33-38}Fs_{15-20;}$ average Mg# 85), in the size range from 300 to 400 μm, affected by pervasive dissolution (Fig. 37a-b). Clinopyroxene in sample 300_S3 does not show significant changes in composition ($Wo_{45-50}En_{32-37}Fs_{15-20}$; average Mg# 81; Fig. 36) with respect to 300_S2. However, S3 crystals have a maximum size of about 100 μm and subeuhedral to anhedral habitus, which testify a lower degree of destabilization (Fig. 37c-d). The composition of oxides, their sizes (5-60 μm) and modal abundances (~5 vol.%) are comparable in both 300_S2 and 300_S3 samples. Sample 300_S4 was flushed with a gas phase at higher CO_2 concentration (0.9 XCO_2^{fl}); here, clinopyroxene and titaniferous magnetite coexist with plagioclase (Fig. 37e-f). Plagioclase forms sub-euhedral crystals up to ~500 μm in size, commonly characterized by dissolution textures along their edges (Fig. 37e-f). Plagioclase is labradoritic with limited oscillations in the anorthite content within the range An 57-65 mol% (Fig. 36). Clinopyroxene is euhedral to sub-euhedral with $Wo_{46-49}En_{30-39}Fs_{14-22}$ composition and size of ~300 μm. These crystals display growth textures that contrast with the higher degree of destabilization observed at lower XCO_2^{fl}; rims are usually marked by Ca and Mg-rich growth zones (Mg# 87-89) enclosing cores with more evolved composition (Mg# 76-82; Fig. 36). On the whole, the porphyritic index (PI) of the samples at 300 MPa increases progressively from ~10 vol.% in sample 300_S2 to ~30 vol.% in 300_S4 (Fig. 37).

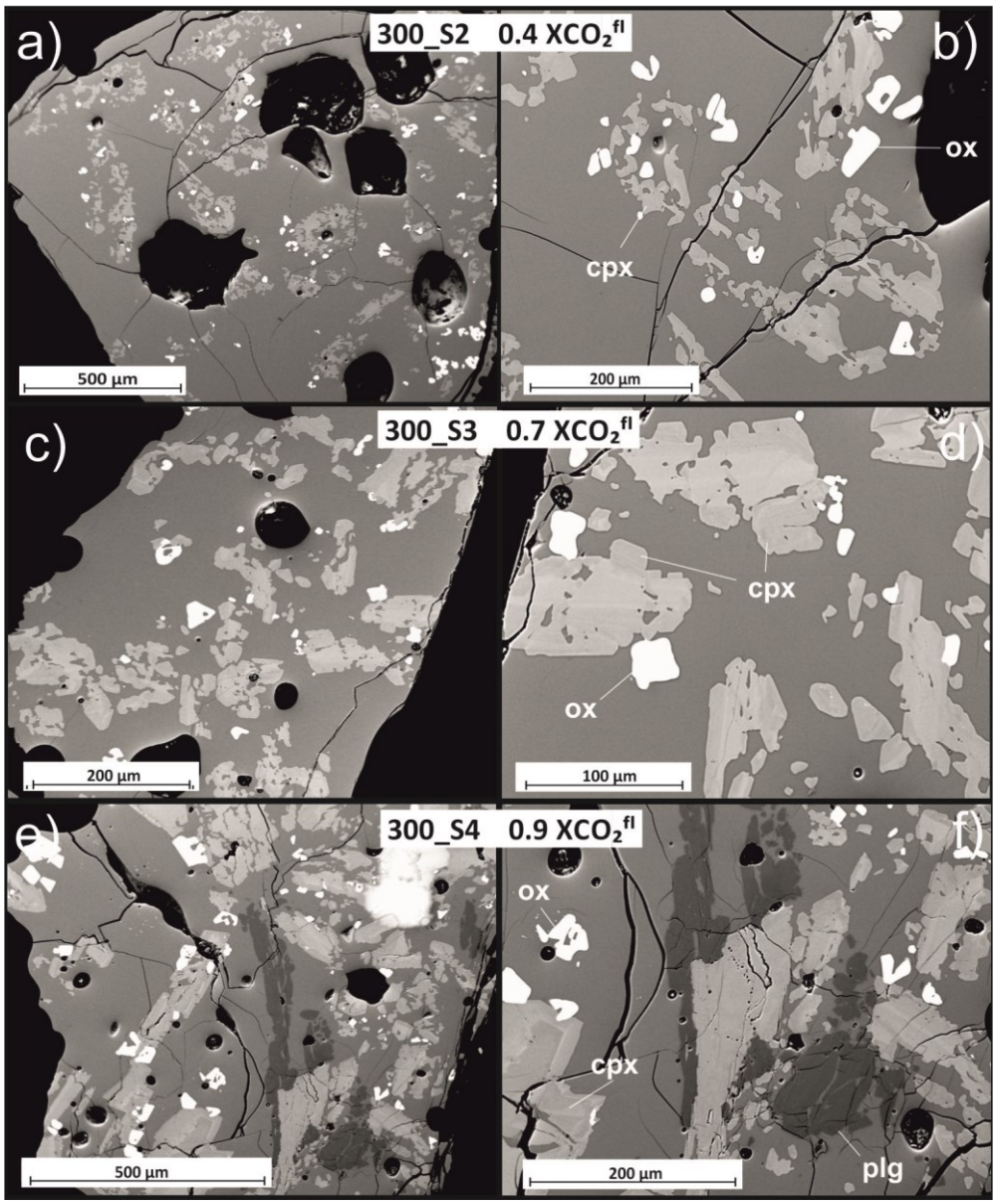

Figure 37. *Textural characteristic of sample S_0 after flushing with a fluid composed of H_2O+CO_2 at 300 MPa and 1080 °C. Experimental results are shown for increasing proportion of CO_2 in the system (XCO_2^{fl}). Note that in condition of high water activity (lower XCO_2^{fl}) the mineral assemblage is only constituted by clinopyroxene (cpx) and opaque oxide (ox) in samples 300_S2 and 300_S3. Plagioclase (plg) is found in sample 300_S4, which was flushed with a gas phase at higher CO_2 concentration.*

At 100 MPa and 0.2 $X\mathrm{CO_2^{fl}}$ (i.e. sample 100_S1), the system is only composed of glass ($\mathrm{SiO_2}$ = 48 wt.%) and zoned clinopyroxene ($\mathrm{Wo_{47\text{-}50}En_{34\text{-}39}Fs_{13\text{-}17;}}$ average Mg# 0.91; Fig. 36; Fig. 38a-b). The mineral assemblage changes to clinopyroxene, plagioclase and titaniferous magnetite at higher proportion of $\mathrm{CO_2}$ (i.e. 0.5 $X\mathrm{CO_2^{fl}}$ in 100 S2 and 0.9 $X\mathrm{CO_2^{fl}}$ in 100_S3; Fig. 38c-f). In sample 100_S1 (0.2 $X\mathrm{CO_2^{fl}}$), clinopyroxene is euhedral to subhedral with slight evidence of dissolution at the core. The degree of destabilization of the cores becomes more severe in sample 100_S2, finally reaching the highest degree in 100_S4, where clinopyroxene has totally resorbed cores (Fig. 38e-f). As the $X\mathrm{CO_2^{fl}}$ of the system increases, the number of clinopyroxene crystals becomes higher, whereas the average Mg# decreases from 0.91 (100_S1) toward a minimum value of 0.84 (100_S4; Fig. 36). A detailed observation of these samples highlights that crystal sizes do not correlate with $\mathrm{CO_2}$. The average crystal size first decreases from ~400 μm (100_S1) to ~200 μm (100_S2) and then increases again up to ~300 μm for highest $X\mathrm{CO_2^{fl}}$ (100_S4), following similar trends of size variations observed during the high pressure experiments (Fig. 38). When present, plagioclase occurs as 200 to 300 μm-large oscillatory-zoned crystals with composition ranging from $\mathrm{An_{53}}$ to $\mathrm{An_{65}}$. However, the average anorthite content declines from An 60 mol% at 0.5 $X\mathrm{CO_2^{fl}}$ (100_S2) to An 58 mol% at 0.9 $X\mathrm{CO_2^{fl}}$ (100_S4; Fig. 36). Observations under optical microscope and BSE images reveal negligible textural differences between plagioclase crystals of samples 100_S2 and 100_S4. Most of plagioclase crystals have elongated euhedral habitus, but crystals with subhedral to anhedral habitus, characterized by minor dissolution surfaces, are also present (Fig. 38).

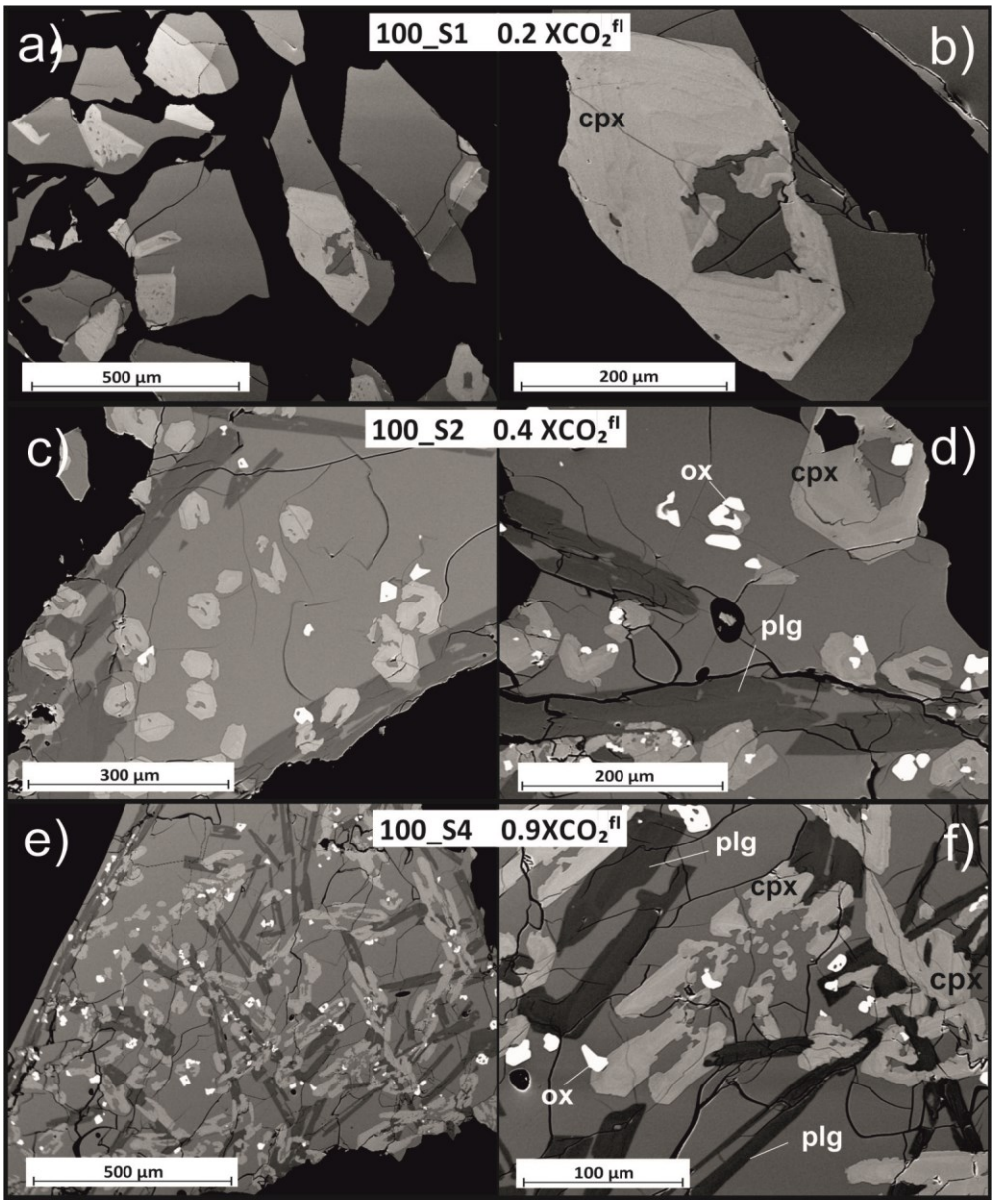

Figure 38. *Textural characteristic of sample S_0 after flushing with a fluid composed of H_2O+CO_2 at 100 MPa and 1080 °C. Experimental results are shown for increasing mole fraction of CO_2 in the fluid phase, as in Figure 3. Note that as the XCO_2^{fl} increases, clinopyroxene crystals show major textural changes and higher degree of resorption, whereas plagioclase crystals do not record significant textural variations.*

4.4.3 Composition of the experimental glasses

Major element compositions of glasses record progressive melt evolution in response to increasing CO_2 content in both sets of experiments. K_2O and Na_2O become progressively more concentrated in the melt, while the concentrations of MgO, CaO and TiO_2 decrease, a feature in good agreement with the change in crystallinity of the melt. The melt chemical changes toward more evolved compositions are well expressed by Harker diagrams with silica and alkalis that correlate negatively with MgO (Fig. 39).

All the oxides correlate with XCO_2, except FeO that shows inflected trends: FeO decreases from low to intermediate XCO_2^{fl}, but increases again towards the highest CO_2 fraction in the fluid phase. At comparable XCO_2, but different crystallization pressures, the system displays changes in FeO concentration on the order of 0.5 wt.%. Remarkable chemical differences between the charges at 100 and 300 MPa with similar CO_2 are also given by the concentrations in K_2O and Na_2O, which show variations up to 0.6 wt.%. CaO contents record changes up to 2.2 wt.% between the 100 and 300 MPa runs, whereas Al_2O_3 values display great variations at the highest proportion of CO_2 in the melt.

The comparison between the glass composition of sample S_0 and that of the samples flushed with CO_2 also put into evidence that K_2O concentration in the residual glasses of the 100 and 300 MPa charges records a significant decrease with respect to sample S_0, accounting for decreasing bulk crystal content during the flushing experiments. In this context, the sample 100_S4 represents an exception because it shows a K_2O glass concentration very close to that of S_0, a feature that well reflects the similar crystal/liquid proportion of these products. Samples S_0 and 100_S4 also show comparable Al_2O_3 glass compositions, whereas for the samples flushed at 100 MPa with a lower fraction of CO_2,

the Al_2O_3 contents is lower than in S_0. A different behavior has been noted in the products flushed at 300 MPa where, for intermediate (300_S3) to higher (300_S4) XCO_2^{fl}, residual glasses record an increase in Al_2O_3 up to 1.2 wt.% compared to S_0.

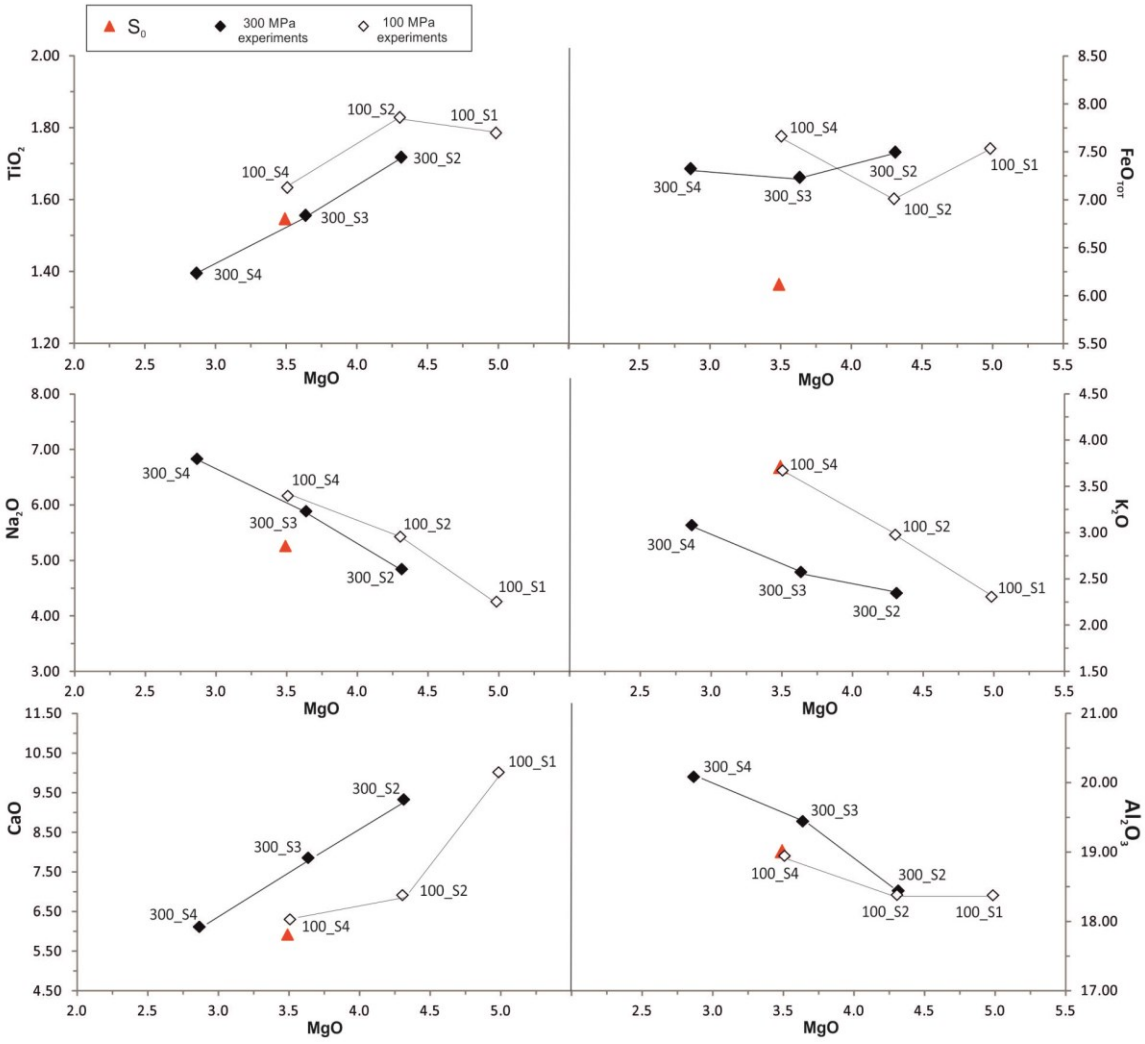

Figure 39. *Major element composition of residual glasses for increasing CO_2 composition after flushing experiments at 300MPa and 100 MPa. In diagrams the composition of the glass in sample S_0 is also shown for comparison.*

4.5 Discussion

Several studies have investigated the solubility of H_2O+CO_2 volatile mixtures over a wide range of pressures, highlighting how the exsolution of CO_2 in basic system starts at depths even greater than 15 km (e.g., Papale, 1997; 1999; Newman and Lowenstern, 2002; Papale et al., 2006; Whitam et al., 2011; Baker and Alletti, 2012). In the case of Mt. Etna alkali basalts, the melt already coexists with an exsolved gas phase mainly composed of CO_2 at pressures around 400 MPa (Spilliaert et al., 2006b). This implies that crystallization from the melt should take place under volatile-saturated conditions at pressures investigated in our experimental runs. Data reported in Table 7 reproduce the total amounts of volatiles dissolved and exsolved after the runs. They reveal that the proportion of exsolved water is always low compared to CO_2, especially at higher pressure conditions, where most of the water remains dissolved in the melt.

The high H_2O concentration in the system during the 300 MPa crystallization experiments of Etnean basalts prevented plagioclase crystallization in samples 300_S2 (2.6 wt.% H_2O in the melt) and 300_S3 (1.7 wt.% H_2O in the melt). At the same time clinopyroxene was stabilized, in accordance with results of Feig et al. (2006) and Hamada and Fujii (2008) for basaltic melts. At 100 MPa, plagioclase is stabilized for water contents between 1.6 and 2.4 wt.%, and is largely present in samples 100_S2 and 100_S3. Therefore, our evaluations of textural and compositional changes of plagioclase as a function of H_2O and CO_2 proportions in the volatile phase are limited to few experimental charges. Conversely, clinopyroxene crystals are always present in all the samples, so their features can be examined throughout the entire range of H_2O and CO_2 proportions inspected at 300 and 100 MPa.

A primary result of our experiments is that the number of crystals, especially plagioclase and clinopyroxene, increases with growing CO_2 proportions relative to water. A similar increase in the crystal abundance was recently documented by Riker et al. (2015) that provided quantitative textural data on plagioclase through decompression experiments on H_2O- and H_2O+CO_2-saturated rhyodacitic magmas of Mount St. Helens. They found that the addition of CO_2 with respect to pure water in the system, especially for pressures <100 MPa, increases the number of plagioclase crystals and produces only minor variations in plagioclase morphologies. Differences observed in the H_2O and H_2O+CO_2 charges have been attributed by Riker et al. (2015) more to the prominent role played by H_2O; indeed, according to these authors, the water content in the H_2O+CO_2 system is ~1 wt.% lower than in the pure H_2O-bearing melt. The evolution of plagioclase abundance and morphology was examined in these studies across a large range of physical conditions, a circumstance that makes difficult discrimination of the effective role of changing CO_2 concentrations relative to water.

The isobaric experiments presented in this study reproduce melt crystallization as a function of variable H_2O and CO_2 proportions in the volatile mixture, maintaining a constant temperature at both 300 and 100 MPa. Results of this study indicate major changes in crystal abundance, size and textures that cannot be ascribed neither to the effect of changing water contents of the system, nor to other parameters that indeed are kept constant. At 300 MPa, plagioclase crystals occur only in sample 300_S4, where the dissolved water in the melt is significantly lower than in 300_S2 and 300_S3. According to several experimental studies, plagioclase responds quickly to changing water contents of the system (e.g., Housh and Luhr, 1991; Lange et al., 2009; Almeev et al., 2012).

Morphology, size and abundance of plagioclase are also strongly influenced by water (Logfren, 1974; 1980; Kirkpatrick, 1981; Sisson and Grove, 1993; Geschwind and Rutherford, 1995; Hammer and Rutherford, 2002). In pure H_2O-bearing systems, a reduction of the water concentration in the melt promotes plagioclase stability, thereby enhancing crystallization (e.g., Moore and Carmichael, 1978; Blundy and Cashman, 2001). Our textural observations on the sample 300_S4 (XH_2O^{fl} 0.1 and XCO_2^{fl} 0.9) reveal however incipient destabilization of plagioclase crystals, which exhibit variable degrees of dissolution along their rims (Fig. 37e-f), even for very low H_2O proportions. Therefore, this behavior cannot be accounted for by decreasing water contents of the system, but rather to CO_2 flushing.

In runs at 100 MPa, plagioclase changes manifest primarily as variations in crystal abundance, whereas sizes remain rather similar. Under these conditions, most of the plagioclase crystals have subhedral habitus with minor evidence of dissolution surfaces in both 100_S2 and 100_S4 samples (Fig. 38). In contrast to higher pressure experiments, the increase of CO_2 proportions affects the plagioclase stability at 100 MPa to a minor extent. We suggest that, in this instance, the destabilizing role of CO_2 was counterbalanced by water, given that the low water concentration and the low pressure should promote plagioclase stability.

Different proportions of H_2O and CO_2 in experimental charges also produce major variations of clinopyroxene textures and sizes. Textures of the clinopyroxene crystals vary at increasing XCO_2^{fl}, with different behavior depending on pressure. In the experimental charges at 300 MPa, the clinopyroxene stability expands with increasing CO_2 proportions in the fluid phase; under these conditions crystals grow, and develop Ca

and Mg-rich growth zones towards the rim (Fig. 37). Consistent with this result, Houchi and Nakamura (2007) investigated the effect of water in the Fo-Di system and demonstrated that increasing water concentrations of the system promote the growth of diopside, and indeed, as the water content of the system initially reduces by about 1 wt.% (at intermediate XCO_2^{fl}) the crystal sizes decrease to ~100 μm. However, from intermediate to higher CO_2 proportions in the melt, our H_2O+CO_2 runs at 300 MPa show that clinopyroxene sizes increase again to ~300 μm (Fig. 37 and 38), suggesting that under elevated CO_2 proportions, but low water, clinopyroxene growth is enhanced with development of crystals with large size. The clinopyroxene behavior is, however, rather different at 100 MPa, where crystals that for low XCO_2^{fl} display large grains of clinopyroxene (~400 μm) became progressively smaller and underwent intense resorption with flushing at increasing proportion of CO_2 (Fig. 38).

Changes of major element concentrations observed in glasses can be interpreted taking into account the processes of crystallization and dissolution that mineral phases underwent during the experiments at 300 and 100 MPa (Fig. 39). The major element variations are generally consistent with the increase of crystallinity, which is in turn correlated positively with the CO_2 amount in the melt. Only FeO_{tot} has a more complex behavior (Fig. 39). At 100 MPa, the extensive dissolution of clinopyroxene observed at the highest CO_2 proportions (Fig. 38e-f) could be responsible for the iron increase in the residual melt. We attribute this behavior to clinopyroxene, because the amount of titaniferous magnetite does not change significantly in the charges. Conversely, in the experimental runs at 300 MPa, the iron increase cannot be exclusively ascribed to clinopyroxene, because we have evidence of increasing growth of clinopyroxene crystals

that coexist with titaniferous magnetite. Reasons for this behavior could be due to change of redox conditions in the charge, as fO_2 decreases ~1 log unit from sample 300_S2 to sample 300_S4 (Table 7). This assumption is consistent with some experimental studies that demonstrated how the partitioning of multivalent cations, such as Fe, varies as a function of the redox conditions of the system (Laubier et al., 2014 and references therein). Specifically, minerals that preferentially incorporate the 2+ iron ions (i.e. olivine, orthopyroxene, clinopyroxene) display increase of the $^{mineral/melt}D_{Fe}$ as fO_2 decreases. As the volume of titaniferous magnetite in sample 300_S4 does not significantly increase, Fe preferentially partitions into the liquid at lower fO_2. The growth of clinopyroxene crystals at 300 MPa also accounts for decreasing Ca and Mg contents in the glass, which records a more significant decline of these elements in the 300_S4. This behavior (particularly of Ca) has been ascribed to the beginning of plagioclase crystallization in the system; indeed it is specially evident at 100 MPa, where it is observed a reduction of CaO of 3 wt.% in those glasses where destabilized clinopyroxene coexists with plagioclase.

4.6 Implications on natural samples

Empirical investigations aimed at reproducing the interaction between silicate melts and volatile species, where the fluid is realistically multicomponent, i.e. H_2O+CO_2, are crucial for interpreting the pre-eruptive histories of magmas that are largely enriched in CO_2, such as those of Mt. Etna. Our experiments on Etnean K-trachybasalts directly simulate processes of CO_2-flushing in distinct sections of the plumbing system, providing new insights for interpreting the range of crystal textures we observed in natural samples.

Although the compositions of the experimental mineral phases do not significantly change with changing CO_2, we have direct evidence that plagioclase and clinopyroxene undergo variable extent of disequilibrium as a consequence of the addition of significant amounts of CO_2. Results show that under elevated CO_2 proportion with respect to water, plagioclase crystals experience variable degrees of dissolution along the rim at 300 MPa, whereas they exhibit minor evidence of destabilization at 100 MPa. Clinopyroxene textures change with opposed behavior during the high and low pressure experiments of flushing. Namely, clinopyroxene stability expands and crystals display growth textures at 300 MPa; in contrast, they destabilize during the 100 MPa runs, recording severe dissolution as the CO_2 proportion increases.

Because we have demonstrated that CO_2 has significant influence on crystals, the effects of CO_2-flushing on products from the recent activity of Mt. Etna cannot be neglected for a proper interpretation of pre-eruptive dynamics. This means that processes ascribed as responsible for disequilibrium textures of crystals from the 2011-2013 eruptive sequence need to be revaluated in the light of the new experimental evidences provided by this study.

I recall that plagioclase crystals characterized by dissolution/resorption and consequent rounding of the core are common in the recent product of Mt. Etna. Moreover, the rims of plagioclase are often affected by single or multiple disequilibrium textures. Most of the augitic clinopyroxenes that were found in lava rocks from short-lasting paroxysms between 2011 and 2013 (in particular the eruptions of March 04, 2012, and April 18, 2013; cf. Viccaro et al., 2014, 2015) also display destabilization along the rim, sometimes evolving to more pervasive disequilibrium features similar to sieve textures.

Combining textural and microanalytical information on mineral phases, we attributed the development of disequilibrium features at the crystal rims to processes of recharge of the residing system by more basic magmas, whereas decompression of water-undersaturated magmas has been thought as the main process controlling the destabilization of plagioclase crystal cores (see Chapter 3.6 for details).

Experimental results presented in this study demonstrate that addition of high CO_2 concentration to the magmatic system may also be responsible for such a kind of disequilibrium.

Exploring the degassing path of Etnean magmas variably enriched in H_2O and CO_2, various authors concur on a CO_2 exsolution depth >400 MPa, i.e. below the plagioclase crystallization threshold (the last located above ~12 km, corresponding to ~340 MPa; Viccaro et al., 2010). Conversely, water is kept almost entirely dissolved in the melt up to ~5.5-7 km (~155-200 MPa). This means that, at the highest pressure investigated by our experiments, i.e. 300 MPa, the system is already volatile-saturated. Although the water concentration in the melt is probably enough to produce plagioclase dissolution/resorption during magma decompression below depths of 5.5-7 km, the migration of CO_2-rich bubbles that are released from deeper regions of the plumbing system (>400 MPa) should further promote plagioclase destabilization during their early grow history. Under these circumstances, the spectrum of disequilibrium textures at variable resorption degree that affect the cores of Etnean plagioclases may form in response of different concentrations of CO_2 in the exsolved gas mixture flushing the magmatic system in which crystals grow.

On the same line of evidence, the transfer and injection of prevalent CO_2-rich gases

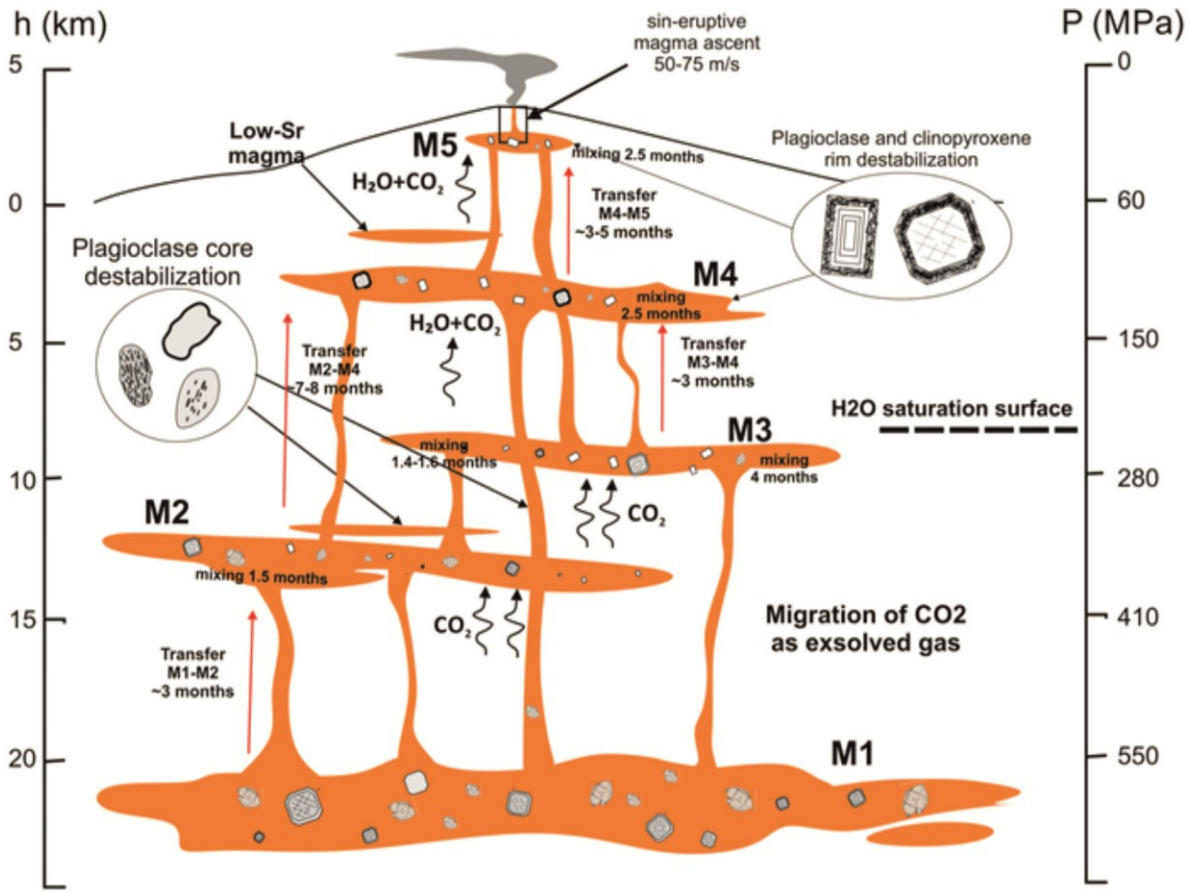

Figure 40. *Schematic representation of the recent history of ascent, storage and degassing of magmas at distinct sections of the plumbing system at Mt. Etna volcano. After an early crystallization of olivine, clinopyroxene and opaque oxides at depth (> 550 km), magmas moved toward surface passing through distinct magmatic environments that are variously connected with each other. During ascent, magma experienced multiple episodes of mixing in these reservoirs, where it resides for relatively short times (~1-18 months). At high pressure (>300 MPa) the system is volatile-saturated and exsolves a gas phase dominantly constitute by CO_2, which strongly destabilize plagioclase crystal in their early stage of growth. The exsolution of H_2O become important only at shallow depth (~250 MPa), where processes of gas flushing affect the stability of plagioclase and clinopyroxene, producing resorption textures at their rim. The injection at very shallow depth (~40Mpa) of dominant gases or gas-rich magmas is the main process able to trigger the paroxysmal eruption. Gases determine overpressurization of the chamber, leading to the fragmentation of the magma that rapidly rises up with rates between 50-75 m/s.*

into the shallow <100MPa reservoirs may have reduced the clinopyroxene stability, causing severe destabilization of their rims. Even in this case, the development of more pervasive disequilibrium features in clinopyroxenes, such as the sieve textures, is consistent with a possible increase of the CO_2 concentration in the gas phase that flushes the magma stored at shallow crustal levels. Such a process may also explain the occurrence of the type of sieve textures at the rim of plagioclase that cannot be attributed to processes of mafic recharge due to the lack of correlation between anorthite, iron and/or magnesium contents (cf. Viccaro et al., 2014).

5. CONCLUDING REMARKS

As one of the most fascinating chapters of the recent history of Mt. Etna, the 2011-2013 paroxysmal sequence drew the interest of the scientific community because of the basaltic CO_2-rich magmatism and the high degree of explosivity of each event.

The present multidisciplinary study (based on different *in-situ* analytical approaches along with experimental determinations) allowed the reconstruction of the internal dynamics of the plumbing system leading to the eruption onset, and opens new perspectives for investigating explosive basaltic volcanism. We have shown that modeling of the compositional heterogeneities of crystals can be successfully used to determine the timescales of a variety of magmatic processes, from the early stages of magma migration and intrusion at crustal reservoirs to syn-eruptive ascent and degassing. A combination of the compositional and temporal information (residence time in different environments and timing of magma transfer between them) provides an indication of a very dynamic plumbing system beneath Mt. Etna, where processes of recharge and emplacement of mafic CO_2-rich melt at shallow depth, along with the migration CO_2-rich gases, are the triggering factors for the onset of paroxysmal eruptions.

Paroxysms have a high hazard potential, which is primarily related to the conspicuous ash-lapilli fall-out that can be ejected hundreds of kilometers from the volcano vents. The effects of these short-lived, but sometimes extremely violent eruptive episodes, can be even more dangerous for those volcanoes that lie in areas of major business and touristic interest, with implications for air traffic, such as in the case of Mt. Etna. Awareness of the magmatic processes driving such kind of eruptions and their

timescales is therefore crucial for the hazard assessment at Mt. Etna, but also at other basaltic volcanoes worldwide where processes of CO_2-flushing and fragmentation of CO_2-oversaturated melts are common mechanisms.

REFERENCES

Aiuppa, A., Federico, C., Paonita, A., Pecoraino, G., Valenza, M. (2002). S, Cl and F degassing as an indicator of volcanic dynamics: The 2001 eruption of Mount Etna. Geophysical Research Letters, 29, 1559;

Aiuppa, A., Moretti, R., Federico, C., Giudice, G., Gurrieri, S., Liuzzo, M., Papale, P., Shinohara, H., Valenza, M. (2007). Forecasting Etna eruption by real time evaluation of volcanic gas composition. Geology 35, 1115-1118;

Aiuppa, A., Bertagnini, A., Métrich, N., Moretti, R. Di Muro, A., Liuzzo, M., Tamburello, G. (2010a). A model of degassing for Stromboli volcano. Earth and Planetary Science Letters 295, 195-204;

Aiuppa, A., Burton, M., Caltabiano, T., Giudice, G., Guerrieri, S., Liuzzo, M., Mur, F., Salerno, G. (2010b). Unusually large magmatic CO_2 gas emissions prior to a basaltic paroxysm. Geophysical Research Letters 37, L17303;

Allard, P., Carbonnelle, J., Dajlevic, D., Le Bronec, J., Morel, P., Robe, M. C., Maurenas, J. M., Faivre-Pierret, R., Martin, D., Saboux, J. C., Zettwoog, P. (1991). Eruptive and diffusive emission of CO_2 from Mt. Etna. Nature 351, 387-391;

Allard, P. (1997). Endogeneous magma degassing and storage at Mt. Etna. Geophysical Research Letters 24, 2219-2222;

Allard, P., Burton, M., Mure, F. (2005), Spectroscopic evidence for a_lava fountain driven by

previously accumulated magmatic gas. Nature, 433, 407–410;

Allard, P. (2010). A CO_2-rich gas trigger of explosive paroxysms at Stromboli volcano, Italy. Journal of Volcanology and Geothermal Research 189, 363-374;

Allegre, C. J., Provost, A., Jaupart, C. (1981). Oscillatory zoning: a pathological case of crystal growth. Nature 294, 223-228;

Almeev, R. R., Holtz, F., Koepke, J., Parat, F. (2012). Experimental calibration of the effect of H_2O on plagioclase crystallization in basaltic melts at 200 MPa. American Mineralogy 97, 1234–1240;

Aloisi, M., Cocina, O., Neri, G., Orecchio, B., Privitera, E., (2002), Seismic tomography of the crust underneath the Etna Volcano, Sicily. Physics of the Earth and Planetary Interiors 134, 139-155;

Anderson, A. T. (1984). Probable relations between plagioclase zoning and magma dynamics, Fuego Volcano, Guatemala. American Mineralogist 69, 660-676;

Andronico, D., Branca, S., Calvari, S., Burton, M., Caltabiano, T., Corsaro, R., Del Carlo, P., Garfì, G., Lodato, L., Miraglia, L., Murè, F., Neri, M., Pecora, E., Pompilio, M., Salerno, G., Spampinato, L., (2005). A multi-disciplinary study of the 2002–03 Etna eruption: insights into a complex plumbing system. Bulletin of Volcanology 67, 314–330;

Andronico, D., Cristaldi, A., Scollo, S. (2008). The 4-5 September 2007 lava fountain at South-East Crater of Mt Etna, Italy. Journal of Volcanology and Geothermal Research 173, 325-328;

Andronico, D., Corsaro, R. A. (2011). Lava fountains during the episodic eruption of South-East Crater (Mt. Etna), 2000: insights into magma-gas dynamics within the shallow volcano plumbing system. Bulletin of Volcanology 73, 1165-1178;

Armienti, P., Pareschi, M. T., Innocenti, F., Pompilio, M. (1994). Effects of magma storage and ascent on the kinetics of crystal growth. The case of 1991-93 Mt. Etna eruption.

Contribution to Mineralogy and Petrology 115, 402-414;

Armienti, P., Pareschi, M.T., Pompilio, M. (1997). Lava textures and time scales of magma storage at Mt. Etna (Italy). Acta Vulcanologica 9, 1-5;

Armienti, P., Perinelli, C., and Putirka, K. D. (2013) A New Model to Estimate Deep-level Magma Ascent Rates, with Applications to Mt. Etna (Sicily, Italy). Journal of Petrology, 54, 795-813;

Austin-Erikson, A., Buttner, R., Dellino, P., Ort, M. H.. Zimanowski, B., (2008). Phreato-magmatic explosions of rhyolitic magma: experimental and field evidence. Journal of Geophysical Research 113, B11201;

Baker, D. R., Alletti, M. (2012). Fluid saturation and volatile partitioning between melts and hydrous fluids in crustal magmatic systems: the contribution of experimental measurements and solubility models. Earth Science Review 114, 298–324;

Behncke B, Branca S, Corsaro RA, De Beni E, Miraglia L, Proietti C (2014) The 2011-2012 summit activity of Mount Etna: Birth, growth and products of the new SE crater. Journal of Volcanology and Geothermal Research 270, 10-21;

Behrens, H., (1995). Determination of water solubilities in high viscosity silicate glasses. An experimental study on NaAlSi3O8 and KAlSi3O8 melts. European Journal of Mineralogy 7, 905–920;

Behrens, H., Ohlhorst, S., Holtz, F., Champenois M (2004) CO_2 solubility in dacitic melts equilibrated with H2O–CO2 fluids. Implications for modeling the solubility of CO_2 in silicic melts. Geochimica et Cosmochimica Acta 68, 4687–4703;

Berlo, K., Blundy, J., Turner, S., Cashman, K., Hawkesworth, C., Black, S., (2004). Geochemical precursors to volcanic activity at Mount St. Helens, USA. Science 306:1167-1169;

Berndt, J., Liebske, C., Holtz, F., Freise, M., Nowak, M., Ziegenbein, D., Hurkuck,W., Koepke, J., 2002. A combined rapid-quench and H_2-membrane setup for internally heated pressure

vessels: Description and application for water solubility in basaltic melts. American Mineralogist 87, 1717–1726;

Berndt, J., Koepke, J., Holz, F., (2005). An experimental investigation of the influence of water and oxygen fugacity of differentiation of MORB at 200 Mpa. Journal of Petrology 46, 135-167;

Bindeman, I.N., Davis, A. M., Drake, M. J. (1998). Ion microprobe study of plagioclase-basalt partition experiments at natural concentration level of trace elements. Geochimica et Cosmochimica Acta 62,1175-1193;

Bindeman, I. N., Davis, A. M. (2000). Trace element partitioning between plagioclase and melt: investigation of dopant influence on partition behavior. Geochim Cosmochim Acta 64:2863–2878;

Blundy, J. D., Wood, B. J. (1991). Crystal-chemical controls on the partitioning of Sr and Ba between plagioclase feldspar, silicate melts, and hydrothermal solutions. Geochimica et Cosmochimica Acta 55, 193-209;

Blundy, J. D., Cashman, K.V. (2001). Ascent-driven crystallization of dacite magmas at Mount St. Helens, 1980-1986. Contribution to Mineralogy and Petrology 140, 631-650;

Blundy, J.D., Cashman, K.V. (2005). Rapid decompression-driven crystallization recorded by melt inclusions from Mount St. Helens Volcano. Geology 33, 793-796;

Blundy, J., Cashman, H., (2008). Petrologic reconstruction of magmatic system variables and processes. Rev Mineral Geochem 69:179-239;

Botcharnikov, R. E., Koepke, J., Holtz, F., McCammon, C., Wilke, M. (2005). The effect of water activity on the oxidation and structural state of Fe in a ferro-basaltic melt. Geochimica et Cosmochimica Acta 69, 5071-5085;

Botcharnikov, R.E., Almeev, R.R., Koepke, J., Holtz, F. (2008). Phase relations and liquid lines of descent in hydrous ferrobasalts: implications for the Skaergaard intrusion and

Columbia river flood basalts. Journal of Petrology 49, 1687–1727;

Bonaccorso, A., Calvari, S. (2013). Major effusive eruptions and recent lava fountains: Balance between expected and erupted magma volumes at Etna volcano. Geophysical Research Letters 40, 6069-6073;

Bonaccorso, A., Bonforte, A., Calvari S., Del Negro, C., Di Grazia,G. , Ganci, G., Neri, M.,Vicari, A., Boschi, E., (2011). The initial phases of the 2008-2009 Mount Etna eruption: a multidisciplinary approach for hazard assessment. Geophysical Research, Solid Earth, 116 (3), B03203;

Branca, S., Del Carlo, P. (2005). Types of eruptions of Etna volcano AD 1670-2003: implications for short-term eruptive behaviour. Bulletin of Volcanology 67, 732-742;

Branca, S., Coltelli, M., De Beni, E., Wijbrans, J. (2008). Geological evolution of Mount Etna volcano (Italy) from earliest products until the first central volcanism (between 500 and 100 ka ago) inferred from geochronological and stratigraphic data. International Journal of Earth Sciences 97, 135-152;

Burnham, C. W. (1979). The importance of volatile constituents. In: Yoder, H.S., Jr. (eds) The evolution of igneous rocks. Princeton University Press, 439-482;

Cabato, J., Altherr, R., Ludwig, T., and Meyer, H.P. (2013) Li, Be, B concentrations and δ7Li values in plagioclase phenocrysts of dacites from Nea Kameni (Santorini, Greece). . Contribution to Mineralogy and Petrology 165, 1135-1154;

Calvari, S., Salerno, G.G., Spampinato, L., Gouhier, M., La Spina, A., Pecora, E., Harris, A.J.L., Labazuy, P., Biale, E., Boschi, E. (2011). An unloading foam model to constrain Etna's 11-13 January 2011 lava fountaining episode. Journal of Geophysical Research 116, B11207;

Cannata, A., Catania, A,, Alparone, S., Gresta, S. (2008). Volcanic tremor at Mt. Etna: inferences on magma dynamics during effusive and explosive activity. Journal of Volcanology and

Geothermal Research 178, 19-31;

Carmichael, I. S. E., Ghiorso, M. S. (1990). The effect of oxygen fugacity on the redox state of natural liquids and their crystallizing phases. In: Nicholls, J., Russel, J.K. (eds), Reviews in Mineralogy and Geochemistry, vol. 24. Mineralogical Society of America, Washington, D.C;

Cashman, K. (2004). Volatile controls on magma ascent and eruption. In: Sparks, R. & Hawkesworth, C. (eds) The State of the Planet: Frontiers and Challenges in Geophysics. American Geophysical Union, 109-124;

Castaing, R. (1951). Application des sondes electroniques aune methode d'analyse ponctuelle chimique et crystallographyque. PhD thesis, University of Paris;

Charlier, B.L.A., Morgan, D.J., Wilson, C.J.N., Wooden, J.L., Allan, A.S.R., and Baker, J.A. (2012). Lithium concentration gradients in feldspar and quartz record the final minutes of magma ascent in an explosive supereruption. Earth Planetary Science Letters 319, 218–227;

Cichy, S., Botcharnikov, R., Holtz, F., Behrens, H. (2011). Vesiculation and microlites crystallization induced by decompression: A case study of the 1991-1995 Mt. Unzen eruption (Japan). Journal of Petrology 52, 1469-1492;

Ciliberto, E., Crisafulli, C., Manuella, F.C., Samperi, F., Scirè, S., Scribano, V., Viccaro, M., Viscuso, E. (2009). Aliphatic hydrocarbons in metasomatized gabbroic xenoliths from Hyblean diatremes (Sicily): genesis in a serpentinite hydrothermal system. Chemical Geology 258, 258-268;

Clocchiatti, R., Condomines, M., Guènot, N., Tanguy, J.C. (2004). Magma changes at Mount Etna: the 2001 and 2002-2003 eruptions. Earth and Planetary Science Letters 226, 397-414;

Collins, S.J., Pyle, D.M., Maclennan, J. (2009). Melt inclusions track pre-eruption storage and

dehydration of magmas at Etna. Geology 37, 571-574;

Coltelli, M., Del Carlo, P., Vezzoli, L., (1998). Discovery of a Plinian basaltic eruption of Roman age at Etna volcano, Italy. Geology, 26, 1095 – 1098;

Correale, A., Paonita, A., Martelli, M., Rizzo, A., Rotolo, S. G., Corsaro, R. A., Di Renzo, V. (2014). A two-component mantle source feeding Mt. Etna magmatism: Insights from the geochemistry of primitive magmas. Lithos 184-187:243-258;

Corsaro, R.A., Civetta, L., Di Renzo, V., Miraglia, L. (2009). Petrology of lavas from the 2004-05 flank eruption of Mt. Etna, Italy: inferences on the dynamics of magma in the shallow plumbing system. Bulletin of Volcanology 71, 781-793;

Corsaro RA, Di Renzo V, Distefano S, Miraglia L, Civetta L (2013). Relationship between petrologic processes in the plumbing system of Mt. Etna and the dynamics of the eastern flank from 1995 to 2005. Journal of Volcanology and Geothermal Research 251,75–89;

Costa, F., Chakraborty, S., Dohmen, R. (2003). Diffusion coupling between trace and major elements and a model for calculation of magma residence times using plagioclase. Geochimica et Cosmochimica Acta 67, 2189-2200;

Costa F., and Chakraborty, S. (2004). Decadal time gaps between mafic intrusion and silicic eruption obtained from chemical zoning patterns in olivine. Earth and Planetary Science Letters 227, 517-530;

Costa, F., Dohmen, R., and Chakraborty, S. (2008). Time scales of magmatic processes from modeling the zoning patterns of crystals. In: Putirka, K.D., and Tepley F.J.III. (eds), Minerals, Inclusions and Volcanic Processes. Reviews in Mineralogy and Geochemistry, 69, 545-594;

Costa, F., and Morgan, D. (2010). Time constraints from chemical equilibration in magmatic crystals. In: Dosseto, A., Turner, S.P., and Van Orman, J.A. (eds), Timescales of Magmatic Processes: From Core to Atmosphere. Wiley-Blackwell, Oxford, 125-159;

Cristofolini, R., Romano, R. (1982). Petrologic features of Etnean volcanic rocks. Memorie della Società Geolica Italiana 23, 99-115;

Cristofolini, R., Ghisetti, F., Scarpa, R., Vezzani, L. (1985). Character of the stress field in the Calabrian arc and southern Apennines (Italy) as deduced by geological, seismological and volcanological information. Tectonophysics 117, 39-58;

D'Alessandro, W., Giammanco, S., Parello, F., Valenza, M. (1997). CO_2 output and $\delta^{13}C$ (CO_2) from Mount Etna as indicators of degassing of shallow asthenosphere. Bulletin of Volcanology 58, 455-458;

Davidson, J. P., Tepley, F. J., III, Palacz, Z., and Meffan-Main, S. (2001). Magma recharge, contamination and residence times revealed by in situ laser ablation isotopic analysis of feldspar in volcanic rocks. Earth Planetary Science Letters 184, 427-442;

Davidson, J. P., Morgan, D. J., Charlier, B. L. A., Harlou, R., and Hora, J. M. (2007). Microsampling and isotopic analysis of igneous rocks: Implications for the study of magmatic systems. Annual Review of Earth and Planetary Sciences 35, 273-311;

Dohmen, R., and Chakraborty, S. (2007b) Fe-Mg diffusion in olivine II: point defect chemistry, change of diffusion mechanisms and a model for calculation of diffusion coefficients in natural olivine. Physics and Chemistry of Minerals, 34, 597-598;

Donaldson, C.H., (1990). Forsterite dissolution in superheated basaltic andesitic and rhyolitic melts. Mineralogical Magazine 54, 67-74;

D'Orazio, M., 1994. Natura ed evoluzione delle vulcaniti dell'Etna e loro relazioni con il magmatismo ibleo. Unpublished doctoral dissertation, University of Pisa.

Druitt, T. H., Costa, F., Deloule, E., Dungan, M., and Scaillet, B. (2012). Decadal to monthly timescales of magma transfer and reservoir growth at a caldera volcano. Nature 482, 77–80;

Erdmann, M., Koepke, J. (2016). Silica-rich lavas in the oceanic crust: experimental evidence for

fractional crystallization under low water activity. Contribution to Mineralogy and Petrology 171, 83. DOI: 10.1007/s00410-016-1294-0

Feig, S. T., Koepke, J., Snow, J.(2006). Effect of water on tholeiitic basalt phase equilibria—an experimental study under oxidizing conditions. Contributions to Mineralogy and Petrology 152, 611-638;

Feig, S. T., Koepke, J., Snow, J. E., (2010). Effect of oxygen fugacity and water on phase equilibria of a hydrous tholeiitic basalt. Contribution to Mineralolgy and Petrology. 160, 551-568;

Ferlito C, Viccaro M, Nicotra E, Cristofolini R (2012) Regimes of magma recharge and their control on the eruptive behaviour during the 2001-2005 period at Mt. Etna (Italy). Bull Volcanol 74533-54;

Ferlito, C., Coltorti, M., Lanzafame, G., and Giacomoni, P.P. (2014). The volatile flushing triggers eruptions at open conduit volcanoes: Evidence from Mount Etna volcano (Italy). Lithos 184-187, 447-455;

Fiege, A. Vetere, F., Iezzi, G., Simon, A., Holtz, F. (2015). The roles of decompression rate and volatiles (H2O + Cl ± CO2 ± S) on crystallization in (trachy-) basaltic magma. Chemical Geology 411, 310–322;

Gao S., Liu X., Yuan H., Hattendorf B., Günther D., Chen L., Hu S.: Determination of Forty Two Major and Trace Elements in USGS and NIST SRM Glasses by Laser Ablation-Inductively Coupled Plasma-Mass Spectrometry, Geostand. Newslet.: The Journal of Geostandards and Geoanalysis, 26, (2002), 181-196;

Gardner, J.E., Burgisser, A., Hort, M., Rutherford, M., (2006). Experimental and model constraints on degassingof magma during ascentand eruption, in: Siebe, C., Macias, J.L., Aguirre-Diaz, G.J., (eds.), Neogene-quaternary Continental Margin Volcanism: A Perspective from Mexico. Geological Society of Amererica, Special Paper 402, Penrose

Conference Series, 99-113;

Genareau, K., and Clarke, A.B. (2010). In situ measurements of plagioclase growth using SIMS depth profiles of $^{7}Li/^{30}Si$: A means to acquire crystallization rates during short-duration decompression events. American Mineralogy 95, 592-601;

Genareau, K., Hervig, R., Clarke, A.B. (2007). Geochemical variations in late-stage growth of volcanic phenocrysts revealed by SIMS depth-profiling. American Mineralogist 92, 1374-1382;

Gerlach, T. M. (1991). Present-day CO_2 emissions from volcanoes. Eos Transactions AGU 72, 240–253;

Geschwind, C. H., Rutherford, M. J. (1995). Crystallization of microlites during magma ascent: the fluid mechanics of 1980^1986 at Mount St Helens. Bulletin of Volcanology 57, 356^370;

Ghiorso, M. S., Gualda, G. A. R., (2015). An H_2O-CO_2 mixed fluid solubility model compatible with rhyolite-MELTS. Contributions to Mineralogy and Petrology, 169: 53;

Giletti, B. J., Casserli, J. E. D. (1994). Strontium diffusion kinetics in plagioclase feldspars. Geochimica et Cosmochimica acta, 58, 3785-3793;

Giletti, B. J., Shanahan, T. M. (1997). Alkali diffusion in plagioclase feldspar. Chemical Geology 139, 3-20;

Ginibre, C., Kronz, A., Wörner, G. (2002a). High-resolution quantitative imaging of plagioclase composition using accumulated backscattered electron images: new constraints on oscillatory zoning. Contributions to Mineralogy and Petrology 142, 436-448;

Ginibre, C., Worner, G., Kronz, A., (2002b). Minor and trace element zoning in plagioclase: implications for magma chamber processes at Parinacota Volcano, N. Chile. Contributions to Mineralogy and Petrology 143, 300-315;

Ginibre, C., and Wörner, G. (2007). Variable parental magmas and recharge regimes of the

Parinacota magma system (N. Chile) revealed by Fe, Mg and Sr zoning in plagioclase. Lithos 98, 118-140;

Grove, T. L., Baker, M. B., Kinzler, R. J. (1984). Coupled CaAl-NaSi diffusion in plagioclase feldspar: experiments and applications to cooling rate speedometry. Geochimica et Cosmochimica Acta 48, 2113-2121;

Gualda., G. A. R., Ghiorso, M.. S., Lemons, R. V., Carley, T. L. (2012). Rhyolite-MELTS: a Modified Calibration of MELTS Optimized for Silica-rich, Fluid-bearing Magmatic Systems. Journal of Petrology 53, 875-890;

Holloway, J. R. (1976). Fluids in the evolution of granitic magmas: consequences of finite CO_2 solubility. Geological Society America Bulletin 87, 1513-1518;

Holloway, J. R., Burnham, C.W. (1972). Melting relations of basalts with equilibrium water pressure less than total pressure. Journal of Petrology 13, 1-29;

Hamada, M., Fujii, T., (2008). Experimental constraints on the effects of pressure and H_2O on the fractional crystallization of high-Mg island arc basalt. Contribution to Mineralogy and Petrology 155, 767;

Herzberg, C., and O'Hara, M. J. (1998) Phase equilibrium constraints on the origin of basalts, picrites, and komatiites. Earth Science Reviews, 44, 39-79.

Hintzmann, W., Müller-Vogt, G. (1969). Crystal growth and lattice parameters of rare-earth doped yttrium phosphate, arsenate and vanadate prepared by the oscillating temperature flux technique. Journal of Crystal Growth 5, 274-278;

Housh, T. B., Lurh, J. F. (1991). Plagioclase-melt equilibria in hydrous system. American Mineralogist 76, 477-491;

Hughes, J. W., Guest, J. E., Duncan, A. M. (1990). Changing styles of effusive eruption on Mount Etna since AD 1600. In: Ryan, M.P. (Ed), Magma transport and storage. Wiley, New York, 385-406;

Hummer, J., Rutherford, M. (2002). An experimental study of the kinetics of decompression-induced crystallization in silicic melts. Journal of Geophysical Research 107, 1-23;

Humphreys, M. C. S., Blundy, J. D., and Sparks, J. D. (2006). Magma evolution and open-system processes at Shiveluch Volcano: Insights from phenocryst zoning. Journal of Petrology 47, 2303-2334;

Humphreys, M. C. S., Menand, T., Blundy, J. D., Klimm, K. (2008). Magma ascent rates in explosive eruptions: Constraints from H_2O diffusion in melt inclusions. Earth and Planetary Science Letters, 270, 25-40;

Ishibashi, H. (2013) Spinel-melt oxygen barometry: a method and application to Cenozoic alkali basaltic magmas from the Higashi-Matsuura district, NW Kyushu, Japan. Geoscience Rep. Shizuoka University 4, 21–32 (in Japanese with English abstract);

Kahl, M., Chakraborty, S., Costa, F., and Pompilio, M. (2011). Dynamic plumbing system beneath volcanoes revealed by kinetic modeling, and the connection to monitoring data: an example from Mt. Etna. Earth Planetary Science Letters 308, 11-22;

Kahl, M., Chakraborty, S., Costa, F., Pompilio, M., Liuzzo, M.,Viccaro, M.(2013). Compositio-nally-zoned crystals and real-time degassing data reveal changes in magma transfer dynamics during the 2006 summit eruptive episodes of Mt. Etna. Bulletin of Volcanology 75, 1-14;

Kahl, M., Chakraborty, S., Pompilio, M., and Costa, F. (2015). Constraints on the Nature and Evolution of the Magma Plumbing System of Mt. Etna Volcano (1991–2008) from a Combined Thermodynamic and Kinetic Modelling of the Compositional Record of Minerals. Journal of Petrology 56, 2025-2068;

Kawamoto, T. (1992). Dusty and honeycomb plagioclase: indicators of processes in the Uchiho stratified magma chamber, Izu Peninsula, Japan. Journal of Volcanology and Geothermal Research 49, 191-208;

Kent, A. J. R., Blundy, J., Casman, K. V., Cooper, K.M., Donnelly, C., Pallister, J. S., Reagan, M., Rowe, M. C., Thorber, C. R., (2007). Vapor transfer priorto the October 2004 eruption of Mount St. Helens, Washington. Geology 35, 231-234;

Kirkpatrick, R. (1981). Kinetics of crystallization of igneous rocks. In: Lasaga, A. & Kirkpatrick, R. (eds), Kinetics of Geochemical Processes. Mineralogical Society of America, Reviews in Mineralogy 8, 321-397;

Klug, C., Cashman, K.V., Bacon, C.R., (2002). Structure and physical characteristics of pumice from the climatic eruption of Mount Mazama (Crater Lake), Oregon, Bulletin of Volcanology 64, 486-501;

Kremers, S., Scheu, B., Cordonnier, B., Speiler, O., Dingwell, D.B., (2010). Influence of decompression rate on fragmentation processes: an experimental study. Journal of Volcanology and Geothermal Research 193, 182-188;

Kuritani, T., (1998). Boundary layer crystallization in a basaltic magma chamber: eveidence from Rishiri Volcano, Northern Japan. Journal of Petrology 39, 1619-1640;

Lange, R. A., Frey, H. M., Hector, J. (2009). A thermodynamic model for the plagioclase-liquid hygrometer/thermometer. American Mineralogist 94, 494–506;

La Delfa, S., Patanè, G., Clocchiatti, R., Joron, J. L., Tanguy, J. C. (2001). Activity of Mount Etna preceding the February 1999 fissure eruption: inferred mechanism from seismological and geochemical data. Journal of Volcanology and Geothermal Research 105, 121-139;

Landi P., Francalanci, L., Pompilio, M., Rosi, M., Corsaro R. A., Petrone, C. M., Nardini, I., Miraglia, L., (2007), The December 2002-July 2003 effusive event at Stromboli volcano, Italy: insights into the shallow plumbing system by petrochemical studies. Journal of Volcanology and Geothermal Research 155, 263-284;

Larsen, E. S., Irving, J., Gonyer, F. A. (1938). Petrological results of a study of the minerals from the Tertiary volcanic rocks of the San Juan region, Colorado. American Mineralogist 23,

227-257;

Laubier, M., Grove, T. L., Langmuir, C. H. (2014), Trace element mineral/melt partitioning for basaltic and basaltic andesitic melts: An experimental and laser ICP-MS study with application to the oxidation state of mantle source regions. Earth and Planetary Science Letters 392: 265–278;

Leeman, W. P., Sisson ,V. B. (1996). Geochemistry of boron and its implications for crustal and mantle processes. Review in Mineralogy 33, 645-707;

Leeman, W. P, Tonarini, S., Chan, L. H, Borg, L. E. (2004). Boron and lithium isotopic variations in a hot subduction zone: The southern Washington Cascades. Chemical Geology 212, 101–124;

Leschik, M., Heide, G., Frischat, G.H., Behrens, H., Wiedenbeck, M., Wagner, N., Heide, K., Geissler, H., Reinholz, U., (2004). Determination of H2O and D2O contents in rhyolitic glasses. Physics and Chemistry of Glasses 45, 238–251;

L'Heureux, I., Fowler, A. D. (1994). A nonlinear dynamical model of oscillatory zoning in plagioclase. American Mineralogy 79, 885-891;

L'Heureux, I., Fowler, A. D., (1996), Isothermal costitutive undercooling as a model for oscillatory zoning in plagioclase. Canadian Mineralalogist 34, 1137-1147;

Liu, M., and Yund, R. A. (1992). NaSi-CaAl interdiffusion in plagioclase. American Mineralogy 77, 275-283;

Lofgren, G. E. (1974). An experimental study of plagioclase crystal morphology: isothermal crystallization. American journal of Science 274, 243-273;

Lofgren, G. E. (1980). Experimental studies on the dynamic of crystallization of silicate melts. Chapter 11. In: Hargraves RB (Ed), Physics of Magmatic Processes. Princeton University Press, Princeton, New Jersey;

Lowenstern, J. B., (2001). Carbon dioxide in magmas and implications for hydrothermal systems:

Mineralium Deposita: 36, 490-502;

Metrich, N., Rutherford, M. J., (1998), Low pressure crystallization paths of H_2O-saturated basaltic-hawaiitic melts from Mt Etna: Implications for open-system degassing of basaltic volcanoes. Geochimica et Cosmochimica Acta 62, 1195-1205;

Metrich, N., Allard, P., Spillaert, N., Andronico, D., Burton, M. R. (2004). 2001 flank eruption of the alkali- and volatile-rich primitive basalt responsible for Mount Etna's evolution in the last three decades. Earth and Planetary Science Letters 228, 1-17;

Mills, R. D., Ratner, J .J. Glazner, A. F., (2011). Experimental evidence for crystal coarsening and fabric development during temperature cycling. Geology 39, 1139-1142;

Mills , R. D., and Glazner, A. F. (2013). Experimental study on the effects of temperature cycling on coarsening of plagioclase and olivine in an alkali basalt, Contribution to Mineralogy and Petrology 166, 97-111;

Mollo, S., Giacomoni, P. P., Coltorti, M., Ferlito, C., Iezzi, G., Scarlato, P. (2015). Reconstruction of magmatic variables governing recent Etnean eruptions: constraints from mineral chemistry and P-T-fO2-H2O modelling. Lithos 212–215, 311–320;

Monaco, C., Tapponier, P., Tortorici, L., Gillot, P. Y. (1997). Late Quaternary slip rates on the Acireale-Piedimonte normal faults and tectonic origin of Mt. Etna (Sicily). Earth and Planetary Science Letters 147, 125-139;

Moore, G. M., Carmichael, I. S. E. (1998). The hydrous phase equilibria (to 3 kbar) of an andesite and basaltic andesite from Western Mexico: constraints on water content and conditions of phenocryst growth. Contribution to Mineralogy and Petrology 130, 304–319;

Morgan, D.J., Blake, S., Rogers, N.W.B., DeVivo, B., Rolandi, G.,Macdonald, R.,Hawkesworth, C. J. (2004). Time scales of crystal residence and magma chamber volume from modelling of diffusion profiles in phenocrysts: Vesuvius 1944. Earth Planetary Science Letters 222, 933-946;

Morgan, D. J, and Blake, S. (2006). Magmatic residence times of zoned phenocrysts: introduction and application of the binary element diffusion modeling (BEDM) technique. Contribution to Mineralogy and Petrology 151, 58-70;

Moriguti, T., Nakamura, E. (1998) Across-arc variation of Li isotopes in lavas and implications for crust/mantle recycling at subduction zones. Earth and Planetary Science Letters 163, 167–174

Mörner, N. A., Etiope, G., (2002). Carbon degassing from the lithosphere. Global Planetary Change 33, 185-203;

Morse, S. A., (1984). Carion diffusion in plagioclase feldspar. Science 225, 504-505;

Mourtada-Bonnefoi, C., Laporte, D. (2002). Homogeneous bubble nucleation in rhyolitic magma: An experimental study of the effect of H2O and CO2. Journal of Geophysical Research 107 (BA), 2066;

Nakamura, M., Shimakita, S. (1998). Dissolution origin and syn-entrapment compositional changes of melt inclusions in plagioclase. Earth and Planetary Science Letters 161, 119-133;

Nelson, S.T., Montana, A. (1992). Sieve textured plagioclases in volcanic rocks produced by rapid decompression. American Mineralogist 77, 1242-1249;

Newman, S., Lowenstern, J. B.,(2002). VolatileCalc: a silicate melt-H2O–CO2 solution model written in Visual Basic for Excel. Computers & Geosciences 28, 597-604;

Nicotra, E., Viccaro, M. (2012a). Transient uprise of gas and gas-rich magma batches fed the pulsating behaviour of the 2006 eruptive episodes at Mt. Etna volcano. Journal of Volcanology and Geothermal Research 227-228, 102-118;

Nicotra, E., Viccaro, M. (2012b). Unusual magma storage conditions at Mt. Etna (Southern Italy) as evidenced by plagioclase megacryst-bearing lavas: implications for the plumbing system geometry and summit caldera collapse. Bulletin of Volcanology 74, 795-815;

Ottolini, L., Bottazzi, P., Vannucci, R. (1993). Quantification of Lithium, Beryllium and Boron in silicates by Secondary Ion Mass Spectrometry using conventional energy filtering, Analytical Chemistry 65, 1960-1968;

Ottolini, L., Camara, F., Hawthorne, F. C., Stirling J. (2002). SIMS matrix effects in the analysis of light elements in silicate minerals: Comparison with SREF and EMPA data, Amererican Mineralogist 87, 147-148;

Papale, P. (1997). Thermodynamic modelling of the solubility of H2O and CO2 in silicate liquids. Contribution to Mineralogy and Petrology 126, 237-251;

Papale, P., Dobran, F.(1994). Magma flow along the volcanic conduit during the Plinian and pyroclastic flow phases of the May 18, 1980, Mount St. Helens eruption. Journal of Geophysical Research 99: doi 10.1029/93JB02972.

Papale, P., Neri, A., Macedonio, G. (1998). The role of magma composition and water content in explosive eruptions. 1. Conduit ascent dynamics. Journal of Volcanology and Geothermal Research 87, 95-115

Papale, P. (1999). Modeling of the solubility of a two-component H2O+CO2 fluid in silicate liquids. American Mineralogist 84, 477-492;

Papale, P., Moretti, R., Barbato, R. (2006). The compositional dependence of the saturation surface of H2O + CO2 fluids in silicate melts. Chemical Geology 229, 78-95;

Patanè D., Barberi, G., Cocina, O., De Gori, P., Chiarabba, C., (2006). Time-Resolved Seismic Tomography Detects Magma Intrusions at Mount Etna. Science 313, 821-823;

Patanè, D., Aiuppa, A., Aloisi, M., Behncke, B., Cannata, A., Coltelli, M., Di Grazia, G., Gambino, S., Gurrieri, S., Mattia, M., and Salerno, G. (2013). Insights into magma and fluid transfer at Mount Etna by a multiparametric approach: A model of the events leading to the 2011 eruptive cycle. Journal of Geophysical Research 118, 3519-3539;

Pearce, T. H., Kolisnik, A.M. (1990). Observation of plagioclase zoning using interference

imagining. Earth Science Review. 29, 9-26;

Pearce, T. H., (1994), Recent work on oscillatory zoning in plagioclase. In: Feldspars and their Reactions. Parsons I (ed) Kluwer Academic Publisher, p. 313-349;

Pearce, N. J. G., Perkins, W. T., Westgate, J. A., Gorton, M. P., Jackson, S. E., Neal, C. R. and Chenery S. P. (1997). A compilation of new and published major and trace element data for NIST SRM 610 and NIST SRM 612 glass reference materials. Geostandard Newsletters: The Journal of Geostandards and Geoanalysis 21, 115-141;

Pearce, N. J. G., Perkins, W. T., Westgate, J. A., Wade, S. C. (2011). Trace-element microanalysis by LA-ICP-MS: the quest for the comprehensive chemical characterisation of single, sun-10 micron volcanic glass shards. Quaternary International 264, 57-81;

Pichavant, M., Di Carlo, I., Rotolo, S. G., Scaillet, B., Burgisser, A., Le Gall, N., Martel, C. (2013). Generation of CO2-rich melts during basalt magma ascent and degassing. Contribution to Mineralogy and Petrology 166, 545-561;

Pompilio, M., Trigila, R., Zanon, V. (1998). Melting experiments on Mt. Etna lavas: I – The calibration of an empirical geothermometer to estimate the eruptive temperature. Acta Vulcanologica 10, 67-75;

Putirka, K. D. (2005). Igneous thermometers and barometers based on plagioclase plus liquid equilibria: Tests of some existing models and new calibrations. American Mineralogist, 99, 336-346;

Putirka, K. D. (2008).Thermometers and Barometers for Volcanic Systems. Review in Mineralogy and Geochemistry In*:* Putirka*,* K., Tepley, F. (Eds.), Minerals, Inclusions a Volcanic Processes 69 Mineralogical Society of America, Chantilly, VA, USA;

Richter, F. M., Davis, A. M., De Paolo, D. J., Watson E. B. (2003). Isotope fractionation by chemical diffusion between molton basalt and rhyolite. Geochimica et Cosmochimica Acta 67, 3905-3923;

Riker, J. M., Cashman, K.V., Rust, A. C., Blundy, J.D. (2015). Experimental constraints on plagioclase crystallization during H_2O- and H_2O–CO_2-saturated magma decompression. Journal of Petrology 0, 1-32;

Rizzo, A., Caracausi, A., Favara, R., Martelli, M., Paonita, A., Paternoster, M., Nuccio, P.M., Rosciglione, A. (2006). New insights into magma dynamics during last two eruptions of Mount Etna as inferred by geochemical monitoring from 2002 to 2005. Geochemistry Geophysics Geosystems 7, Q06008;

Roeder, P. L., and Emslie, R. F. (1970). Olivine-liquid equilibrium. Contribution to Mineralogy and Petrology, 29, 275-289;

Rutherford, M. J. (2008). Magma Ascent Rates. In: Putirka, K.D., Tepley III, F., J., (eds) Minerals, Inclusions and Volcanic Processes. Reviews in Mineralogy and Geochemistry 69, Mineralogical Society of America, Chantilly, VA, USA, 241-271;

Sato, H., (1989). Mg-Fe partitioning between plagioclase and liquids in basalts of Hole 504B, ODP leg 111: a study of melting at one atm. College Station, TX, Proc Ocean Drilling Program Science Research 111, 17-26;

Shea, T., Gurioli, L., Larsen, J. F., Houghton, B. F., Hammer, J. E., Cashman, K. V., (2010). Linking experimental and natural vesicle textures in Vesuvius 79AD white pumice. Journal of Volcanology and Geothermal Reearch 192, 69-84;

Shea, T., Costa, F., Krimer, D., Hammer, J. E. (2015). Accuracy of timescales retrieved from diffusion modeling in olivine: a 3D perspective. American Mineralogist, doi:10.2138/am-2015-5163;

Shinohara, H., Aiuppa, A., Giudice, G., Gurrieri, S., Liuzzo, M. (2008). Variations of H2O/CO2 and CO2/SO2 ratios of volcanic gas discharged by continuous degassing of Mount Etna volcano, Italy. Journal of Geophysical Research 113, B09203;

Shishkina, T. A., Botcharnikov, R. E., Holtz, F., Almeev , R. R., Portnyagin, M. V. (2014).

Solubility of H2O- and CO2-bearing fluids in tholeiitic basalts at pressures up to 500 MPa. Chemical Geology 277, 115-125;

Shishkina, T. A., Botcharnikov, R. E., Holtz, F., Almeev, R. R., Jazwa, A. M., Jakubiak, A. A., (2014). Compositional and pressure effects on the solubility of H2O and CO2 in mafic melts. Chemical Geology 388, 112-129;

Singer, B. S., Dungan, M. A., and Layne, G. D. (1995). Textures and Sr, Ba, Mg, Fe, K and Ti compositional profiles in volcanic plagioclase: clues to the dynamics of calc-alkaline magma chamber. American Mineralogist 80, 776-798;

Sisson, T.W., Grove, T. L., (1993). Temperatures and H2O contents of low-MgO high-alumina basalts. Contribution to Mineralogy and Petrology 113, 167–184;

Slodzian, G. (1964). Etude d'une method d'analise locale chimique et isotopique utilisant l'emission ionique secondaire. Annales des Physique 9,591-648;

Smith, R. K., Lofgren, G. E. (1983). An analytical and experimental study of zoning in plagioclase. Lithos 16, 153-168;

Snyder, D. A, Carmichael, I.S.E., (1992). Olivine-liquid equilibria and the chemical activities of FeO, NiO, Fe2O3, and MgO in natural basic melts. Geochimica et Cosmochimica. Acta 56, 303-318;

Spilliaert, N., Allard, P., Metrich, N., Sobolev, A.V. (2006a). Melt inclusions record of the conditions of ascent, degassing, and extrusion of volatile-rich alkali basalt during the powerful 2002 flank eruption of Mount Etna (Italy). Journal of Geophysical Research,Solid Earth 111, B04203;

Spilliaert, N., Metrich, N., Allard P. (2006b). S–Cl–F degassing pattern of water-rich alkali basalt: modelling and relationship with eruption styles on Mount Etna volcano. Earth and Planetary Science Letters 248, 772–786;

Sparks, R. S. J., and Pinkerton, H. (1978). Effects of degassing on rheology of basaltic lava.

Nature 276, 385–386;

Sparks, R. S. J., (2003). Dynamics of Magma Degassing. In C. Oppenheimer, D. M. Pyle, & J. Barclay, Eds., Volcanic Degassing, London: The Geological Society;

Streck, M. J. (2008). Mineral textures and zoning as evidence for open system processes. In: Minerals, inclusions and volcanic processes, Putirka, K.D., Tepley III, F.J. (eds). Review in Mineralogy and Geochemistry 69, Mineralogical Society of America, 595-622;

Sugawara, T. (2001). Ferric iron partitioning between plagioclase and silicate liquid: thermodynamics and petrological applications. Contribution to Mineralogy and Petrology 141, 659-686;

Tanguy, J. C., Clocchiatti, R. (1984). The Etnean lavas, 1977-1983: petrology and mineralogy. Bulletin of Volcanology 47, 879-894;

Tanguy, J. C., Condomines, M., Kieffer, G. (1997). Evolution of Mount Etna Magma: constraint on the present feeding system and eruptive mechanism. Journal of Volcanology and Geothermal Research 75, 221-250;

Toplis, M. J. (2005). The thermodynamic of iron and magnesium partitioning between olivine and liquid: criteria for assessing and predicting equilibrium in natural and experimental systems. Contribution to Mineralogy and Petrology, 149, 22-39;

Tsuchiyama, A. (1985). Dissolution kinetics of plagioclase in the melt of the system diopside-albite-anorthite, and the origin of dusty plagioclase in andesites. Contribution to Mineralogy and Petrology 89, 1-16;

Tsuchiyama, A., Takahashi, E. (1983). Melting kinetics of a plagioclase feldspar. Contribution to Mineralogy and Petrology 84, 345-354;

Tsune, A., Toramaru, A., (2007). A simple model of oscillatory zoning in magmatic plagioclase: development of an isothermal undercooling model. American Mineralogist 92, 1071-1079;

Van Achterberg, E., Ryan, C. G., Jackson, S. E., Griffin, W. L. (2001). Data reduction software for LA-ICPMS: appendix. In: Sylvester, P.J. (Ed), Laser Ablation-ICP-Mass Spectrometry in the Earth Sciences: Principles and Applications. Mineralogical Association of Canada, Short Course Series 29, 239-243;

Vetere, F., Behrens, H., Schuessler, J. A., Holtz, F., Misiti, V., Borchers, L. (2008). Viscosity of andesite melts and its implication for magma mixing prior to Unzen 1991–1995 eruption. Journal of Volcanology and Geothermal Research 175, 208–217;

Vetere, F., Holtz, F., Behrens, H., Botcharnikov, R. E.; Fanara, S. (2014). The effect of alkalis and polymerization on the solubility of H_2O and CO_2 in alkali-rich silicate melts. Contribution to Mineralogy and Petrology 167, 1014. DOI 10.1007/s00410-014-1014-6;

Vetere, F., Mollo, S., Giacomoni, P.P., Iezzi, G., Coltorti, M., Ferlito, C., Holtz, F., Perugini, D., Scarlato, P. (2015). Experimental constraints on the origin of pahoehoe "cicirara" lavas at Mt. Etna volcano (Sicily, Italy). Bulletin of Volcanology 77, 44. DOI 10.1007/s00445-015-0931-1;

Viccaro M, Ferlito C, Cortesogno L, Cristofolini R, Gaggero L (2006) Magma mixing during the 2001 event at Mt. Etna (Italy): effects on the eruptive dynamics. Journal of Volcanology and Geothermal Research 149, 139-159;

Viccaro, M., Cristofolini, R. (2008). Nature of mantle heterogeneity and its role in the short-term geochemical and volcanological evolution of Mt. Etna (Italy). Lithos 105, 272-288;

Viccaro, M., Giacomoni, P.P., Ferlito, C., and Cristofolini R. (2010). Dynamics of magma supply at Mt. Etna volcano (Southern Italy) as revealed by textural and compositional features of plagioclase phenocrysts. Lithos 116, 77-91;

Viccaro, M., Nicotra, E., Millar, I.L., Cristofolini, R. (2011). The magma source at Mount Etna volcano: perspectives from the Hf isotope composition of historic and recent lavas. Chemical Geology 281, 343-351.

Viccaro, M., Giuffrida, M., Nicotra, E., and Ozerov, A.Yu. (2012). Magma storage, ascent and recharge history prior to 1991 eruption at Avachinsky volcano, Kamchatka, Russia: inferences on the plumbing system geometry. Lithos 140-141, 11-24;

Viccaro, M., Garozzo, I., Cannata, A., Di Grazia, G., Gresta, S. (2014). Gas burst vs. gas-rich magma recharge: a multidisciplinary study to reveal factors controlling triggering of the recent paroxysmal eruptions at Mt. Etna. Journal of Volcanology and Geothermal Research 278-279, 1-13;

Viccaro, M., Calcagno, R., Garozzo, I., Giuffrida, M., Nicotra, E. (2015). Continuous magma recharge at Mt. Etna during the 2011-2013 period controls the style of volcanic activity and compositions of erupted lavas. Mineralogy and Petrology 109, 67-83;

Viccaro, M., Giuffrida, M., Nicotra, E., and Cristofolini, R. (2016a). Timescales of magma storage and migration recorded by olivine crystals in basalts of the March-April 2010 eruption at Eyjafjallajökull volcano, Iceland. American Mineralogist 101, 222-230;

Viccaro, M., Barca, D., Bohrson, W.A., D'Oriano, C., Giuffrida, M., Nicotra, E., Pitcher, B.W. (2016b). Crystal residence time from trace element zoning in plagioclase reveal changes in magma transfer dynamics at Mt. Etna during the last 400 years. Lithos 248, 309-323;

Wallace, G.S., and Bergantz, G.W., (2002). Wavelet-based correlation (WBC) of zoned crystal populations and magma mixing. Earth Planetary Science Letters 202, 133–145;

Wallace, G. S., and Bergantz, G.W., (2004). Constraints on mingling of crystal populations from off-center zoning profiles: a statistical approach. American Mineralogist 89, 64–73;

Webster, J. D., Kinzler, R. J., Mathez, E. A., (1999). Chloride and water solubility in basalt and andesite melts and implications for magmatic degassing. Geochimica et Cosmochimica Acta 63, 729–738;

Webster, J. D., Holloway, J. R., and Hervig, R. L. (1989). Partitioning of lithophile trace-elements between H_2O and H_2O+CO_2 fluids and topaz rhyolite melt. Economic Geology 84, 116-

134;

Wilke, M., Behrens, H. (1999). The dependence of the partitioning of iron and europium between plagioclase and hydrous tonalitic melt on oxygen fugacity. Contribution to Mineralogy and Petrology 137, 102-114;

Witham, F., Blundy, J., Kohn, S. C., Lesne, P., Dixon, J., Churakov, S. V., Botcharnikov, R. (2012). SolEx: a model for mixed COHSCl-volatile solubilities and exsolved gas compositions in basalt. Computers and Geosciences 45, 87-97;

Whittington, A., Richet, P., Linard, Y., and Holtz, F. (2001). The viscosity of hydrous phonolites and trachytes. Chemical Geology 174, 209-223;

Zellmer, G. F., Blake, S., Vance, D., Hawkesworth, C., and Turner, S. (1999). Plagioclase residence times at two island arc volcanoes (Kameni island, Santorini, and Soufriere, St. Vincent) determined by Sr diffusion systematics. Contribution to Mineralogy and Petrology 136, 345-357;

Zellmer, G. F., Sparks, R. S. J., Hawkesworth, C. J., and Wiedenbeck, M. (2003). Magma emplacement and remobilization timescales beneath Montserrat: insights from Sr and Ba zonation in plagioclase phenocrysts. Journal of Petrology 44, 1413-1431;

Zhang, Y., and Behrens, H. (2000). H_2O diffusion in rhyolitic melts and glasses. Chemical Geology 169, 243-262.